Fault Plane Structure of the 1995 Antofagasta Earthquake (Chile) Derived From Local Seismological Parameters

Dissertation

Zur Erlangung des akademischen Grades
Doctor rerum naturalium
(Dr. rer. nat.)
in der Wissenschaftsdisziplin Geophysik

eingereicht an der
Mathematisch - Naturwissenschaftlichen Fakultät
der Universität Potsdam

von

Monika Sobiesiak

Potsdam, im November 2004

Contents

Zusammenfassung

Die Bruchfläche grosser Erdbeben umfaßt inhomogene Strukturen, die bisher hauptsächlich in teleseismischen Untersuchungen nachgewiesen werden konnten. Häufig werden begrenzte Bereiche auf einer Bruchfläche beobachtet, die durch eine starke Konzentration des freigesetzten seismischen Moments und durch grosse Dislokationen gekennzeichnet sind. Diese Bereiche werden als "asperities" bezeichnet, die offensichtlich starken Einfluß auf den Bruchverlauf des Hauptbebens ausüben. Beschaffenheit und Eigenschaften der Strukturen in einem Herdgebiet, die verantwortlich sind für die Bildung solcher "asperities" und deren eventueller Bedeutung für Schadensverteilungen in zukünftigen Erdbeben, sind Gegenstand aktueller geowissenschaftlischer Untersuchungen.

In der vorliegenden Arbeit werden "asperity"-Strukturen auf der Bruchfläche des M_w=8.0 Antofagasta Erdbebens vom 30. Juli 1995 im Norden Chiles identifiziert. Es handelt sich hierbei um ein typisches Subduktionsbeben mit Aufschiebungscharakter, das in der seismogenen Zone zwischen der abtauchenden pazifischen Nazca-Platte und der überschiebenden südamerikanischen Platte stattfand. Durch die Zusammenarbeit der Deutschen Task Force für Erdbeben und dem sich während des Bebens bereits vor Ort befindlichen CINCA '95 Projektgruppe, konnte ein bis zu 44 Stationen umfassendes seismologisches Netzwerk zur Registrierung der Nachbeben errichtet werden. Vor allem die seeseitige Erweiterung des Netzes durch 9 OBH Stationen trug zur hohen Präzision der Hypozentrenbestimmung der Nachbeben bei, die sich hauptsächlich auf der Bruchfläche und damit im Küstenbereich um die Stadt Antofagasta und der nördlich gelegenen Halbinsel Mejillones verteilten. Die Tiefenverteilung des starken Nachbebenclusters, das aufgrund seines Charakters eine Unterscheidung von der in der Wadati-Benioff-Zone tiefer gelegenen Hintergrundseismizität ermöglichte, erstreckte sich etwa zwischen 10 und 50 km Tiefe.

Aus dem aus manuell bestimmten Hypozentren bestehenden Datensatz wurden für die vorliegende Studie insgesamt 1302 Nachbebenereignisse ausgewählt, die sich auf der Bruchfläche des Hauptbebens sowie dem nördlich angrenzenden Gebiet unter der Halbinsel Mejillones befinden. Die zentralen Methoden zur Untersuchung der Nachbeben, die hier angewendet werden, sind die Kartierung des b-Wertes aus der $Gutenberg - Richter$ Beziehung und die empirisch berechnete Verteilung der von den Nachbeben abgestrahlten seismischen Energie. Beide Parameter zeigen deutliche Variationen auf der Bruchfläche, ergänzen sich in ihren Aussagen und liefern Hinweise auf Lokation, Ausdehnung und Grenzen von Strukturen, die für die Entstehung von "asperities" verantwortlich sein können. Auf der Bruchfläche des Antofagasta Bebens wurden mit Hilfe dieser Methoden zwei getrennte "asperities" erkannt, deren Grösse, seismisches Moment, mittlere Dislokation und Spannungsabfall berechnet wurde.

Diese Zusammenhänge konnten vor allem durch den Vergleich der publizierten Kartierungen zur teleseismisch gewonnenen Herd-Zeit-Funktion des Bebens, der Verteilung der isostatischen Restanomalien des Gravitationsfeldes, der Geologie und der räumlich verteilten v_p/v_s Verhältnisse, gewonnen aus einer Lokalbebentomographie unter Verwendung des selben Datensatzes, geklärt werden. Von zentraler Bedeutung ist dabei das Ergebnis, dass hohe b-Werte positiv korrelieren mit hohen Raten der seismischen Momentenverteilung, hohen Werten der isostatischen Restanomalien, niedrigen seismische Energien der Nachbeben und hohen Werten der v_p/v_s Verhältnisse. Aus der räumliche Kongruenz zwischen isostatischen Restanomalien und den im Bereich des Untersuchungsgebietes in der oberen Platte befindlichen jurassischen Batholithe und dem Nachweis des Kontaktes dieser Batholithe mit der seismogenen Zone, konnte die Schlußfolgerung gezogen werden, daß die geologische Struktur die Bildung der "asperities" verursacht.

Das damit erstellte Modell ermöglicht eine Aussage über die Vorgänge in der seismogene Zone vor, während und nach dem Hauptbeben. Unter der Annahme der Gültigkeit des "asperity"-Modells wird gefolgert, daß vor dem Beben Spannungen dort akkumuliert werden, wo sich die jurassichen Batholithe mit der durch Auftriebskräfte nach oben gedrückten Nazca-Platte "verhaken". Bei Durchgang einer Bruchfront entsteht im "vorgespannten" Bereich der Batholithe die grösste Momentenfreisetzung und Dislokation. Konsequenterweise zeigen diese Bereiche der Bruchfläche einen höheren Zerstörungsgrad des beteiligten Materials, was sich in einer relativ grösseren Anzahl von kleineren Bruchvorgängen in der Nachbebenserie äußert. Dadurch lassen sich diese Bereiche mittels hoher b-Werte der Nachbebenserie identifizieren. Die addierten seismischen Energien, die durch die Nachbeben abgestrahlt werden, sind dort hoch, wo sich die Übergänge zwischen hohen und niedrigeren b-Werten befinden. Diese Übergänge scheinen identisch zu sein mit den äusseren Umrissen der Batholithe; loten also folglich Materialgrenzen aus.

Die beschriebenen Resultate weisen eindeutig auf die inhomogene Struktur der Bruchfläche des Hauptbebens hin. Daß die Bruchfläche aufgrund dieser Inhomogenitäten von einer planaren Fläche abweicht, konnte durch die Untersuchung von 295 Herdflächenlösungen aus der Nachbebenserie bestätigt werden. Die summierten Momententensoren dieser Herdflächenlösungen weisen wesentlich höhere CLVD-Anteile für den südlichen Abschnitt der Bruchfläche auf als dies für die Momententensoren der nördlichen Bruchfläche der Fall ist. Die südliche Bruchfläche beherbergt die zuvor identifizierten "asperity"-Strukturen. Der CLVD-Anteil eines Momententensors ist zwar immer noch deviatorisch, beweist aber einen signifikanten 3D-Deformationszustand. Dies steht in Einklang mit den hohen v_p/v_s Verhältnissen im Breich der "asperities", die durch intrudierende Fluide nach dem Hauptbeben interpretiert werden. Die verschiedenen Mechanismen der Herdflächenlösungen weisen zudem auf die Segmentierung der Herdfläche und auf ein leichtes "slip-partitioning" hin.

Summary

Fault planes of large earthquakes incorporate inhomogeneous structures. This can be observed often in teleseismic studies through the spatial distribution of slip and seismic moment release caused by the mainshock. Both parameters are often concentrated on patches on the fault plane with much higher values for slip and moment release than their adjacent areas. These patches are called asperities which obviously have a strong influence on the mainshock rupture propagation. Condition and properties of structures in the fault plane area, which are responsible for the evolution of such asperities or their significance on damage distributions of future earthquakes, are still not well known and subject to recent geo-scientific studies.

In the presented thesis asperity structures are identified on the fault plane of the M_w=8.0 Antofagasta earthquake in northern Chile which occurred on 30th of July, 1995. It was a thrust-type event in the seismogenic zone between the subducting pacific Nazca plate and the overriding South American plate. In cooperation of the German Task Force for Earthquakes and the CINCA'95 project a network of up to 44 seismic stations was set up to record the aftershock sequence. The seaward extension of the network with 9 OBH stations increased significantly the precision of hypocenter determinations. They were distributed mainly on the fault plane itself around the city of Antofagasta and Mejillones Peninsula. The pronounced aftershock cluster, which could be well distinguished from deeper background seismicity, had a depth range of approximately 10 to 50 km depth thus the deeper limit of the seismogenic zone could be well determined.

From the database of manually determined hypocenters, 1302 events were selected for further studies in this thesis. They all were located either on the fault plane itself or in the adjacent area to the North beneath Mejillones Peninsula. The principle methods to be applied to the dataset were the mapping of the b-value from the $Gutenberg - Richter$ relation and the spatial distribution of the empirically determined aftershock radiated seismic energy. Both parameters show significant spatial variations on the fault plane, are complementary in their results and help to constrain location, size and boundary of the structure responsible for asperities. Two distinct asperities could be identified on the Antofagasta fault plane. The size, seismic moment, avarage slip and stress drop were calculated for each asperity.

The mapped parameters were compared to the teleseismically determined source time function of the mainshock, the isostatic residual anomalies of the gravity field, the geology, and the spatial distribution of v_p/v_s ratios obtained from a local earthquake tomography derived from the same dataset, reveals new insight on the relations between proposed structures and observed variations in mapped parameters. The positive correlation of high b-values with high mainshock seismic moment release, high isostatic residual anomalies, low

aftershock radiated energy, and high v_p/v_s ratios is an important result to give information on the physics behind these parameters. The spatial congruence between the isostatic residual anomalies, the location of the jurassic batholiths in the upper crust, and the evidence, that these batholiths are in contact with the subduction interface it is concluded, that the geological structure is the major cause for the asperities.

Based on these findings, a model could be developed describing the processes in the seismogenic zone before, during and after the mainshock. Assuming the asperity-model is valid, stresses are accumulated where the batholiths interact with the subducted Nazca plate, which is driven upward by buoyant forces. When the rupture front of an earthquake is going through, the pre-stressed areas of the batholiths show the largest slip and moment release. As a consequence, the material in these areas suffers a high degree of damage, documenting itself in a relatively larger number of small ruptures and cracks. Therefore these areas can be detected by high b-values in the aftershock sequence. The aftershock radiated seismic energies are high at the transition of high to low b-values. Theses transition zones seem to be identical with the outer limits of the batholiths and thus line out changes in material.

The described results clearly indicate the inhomogeneous structure of the mainshock fault plane. Caused by this inhomogeneous structure, the surface of the fault plane deviates from being planar, which could be evidenced by investigating 295 aftershock fault plane solutions. The summed moment tensor solutions of focal mechanisms in the southern part of the fault plane possess a much higher CLVD than the equivalent moment tensor solutions in the northern part. This is attributed to the asperity-structures located in the southern part of the fault plane. Although the CLVD component of a moment tensor is still deviatoric, it refers to a deformational state with a significant 3D component. This is in accord with the high v_p/v_s ratios found in the area of the asperities which are interpreted in terms of fluid intrusion after the mainshock. An additional result is the segmentation and slight slip partitioning of the mainshock fault plane obtained from the interpretation of the different types of aftershock focal mechanisms.

1. Introduction

1.1 Inhomogeneous fault planes and their implication to seismic hazard

Fault planes of large earthquakes incorporate inhomogeneous structures which have a persistent influence on the rupture propagation itself. Regarding these interactions between fault structures and main shock rupture, one key question which should be considered in modern seismic hazard assessment is whether this can affect the damage distributions in urban areas caused by large earthquakes. A second consequential question is then whether the influencing fault structures are of any importance for future earthquakes.

The two large earthquakes which will be addressed in this thesis are the M_w=8.0, 1995, Antofagasta earthquake in the Northern Chile subduction zone, and the M_w=6.9, 1997, Cariaco strike slip earthquake in Northeastern Venezuela. Regarding the key questions, the two earthquakes have in common, that the damage distributions they caused might be related to the locations of influencing fault structures near or in the vicinity of the major cities and towns of the areas concerned. The studies and related results presented in this thesis concentrate on the Antofagasta earthquake whereas the Cariaco earthquake will be discussed only briefly to confirm important findings of the Antofagasta case study.

The complexity of rupture planes had been observed in far field body wave traces of large earthquakes as for example the 1940 Imperial Valley, the 1964 Alaska, and 1976 Guatemala earthquakes (*Trifunac & Brune*, 1970; *Wyss & Brune*, 1967; *Kanamori & Stewart*, 1978). These large earthquakes all showed a complex energy or moment release resulting in the division of the main shock rupture into more than one sub-event. *Kanamori & Stewart* (1978) discussed the heterogeneous mechanical properties of the source area as differences in strength, pore pressure, slip characteristics or a combination of these factors as a cause for multiple events and emphasized the important effect of complexity on the strong ground motion.

Seeking physical interpretations for the observed heterogeneity of the fault planes seismologists introduced the asperity and the barrier model (*Lay & Kanamori*, 1981; *Lay et al.*, 1982; *Madariaga*, 1979; *Papageorgiou & Aki*, 1983; *Das & Kostrov*, 1988; *Johnson & Nadeau*, 2002; *Das & Aki*, 1977; *Aki*, 1979, 2002; *Ruff*, 1992). Both models try to explain heterogeneity in a theoretical way, making the assumption that asperities are patches of higher stress concentrations before the main shock rupture; barriers are defined as patches of higher strength on the fault plane. Here in this thesis, the asperity model was adopted as a first step to discuss the observations. However, the obtained results led to the conclusion that only a mixture of both models is able to account for all observed phenomena (*Aki*, 1984; *Scherbaum*, 1994) and often it seems to be more a question of verbal preference, which conception is used.

The previous examples show that the identification of rupture plane complexity was mainly done through investigation of teleseismic seismograms. This implies that structural inhomogeneities at the source are studied through low frequency information which reduces the resolution for small scale structures and their locations with respect to the fault plane. The same problem seems to arise for the investigation of large earthquakes with the help of geodetic data. Often the resulting displacement fields are smooth exhibiting only one center of major displacement. Simultaneous invertion of geodetic and seismological data (*Ihmlé & Ruegg*, 1997) evidenced the importance of the integration of independently derived results to obtain a more detailed picture of relevant structures.

Thus, recently emphasis is put on the acquisition of local seismological data to investigate source related phenomena. The advancement of seismological instrumentation, e.g. dense station spacings and the use of different sensor types covering a wide frequency range of seismic signals, envisaged high resolution data sets, amiable also to the application of statistical methods. The attempts to be made then were to find appropriate parameters, sensitive to map the proposed inhomogeneities in a source area with a suitable resolution. This is also one target in this thesis. Further it will be varified whether source parameters like moment release, stress drop and slip values related to the inhomogeneities can be reasonably estimated. As a future target the investigation of probable interactions between fault related inhomogeneities producing high moment release and soil dynamics should be proposed.

Due to the high quality of data sets, the seismic b-value of the Gutenberg-Richter (GR) relation (*Gutenberg & Richter*, 1944) has been proven to be a promising parameter to map out spatial variations in seismogenic areas (*Wiemer & Katsumata*, 1999; *Wiemer & McNutt*, 1997; *Wyss et al.*, 1997). First attempts to look for physical explanations of the b-value were made in laboratory experiments and mining induced seismicity (*Mogi*, 1962; *Scholz*, 1968; *Urbancic et al.*, 1992) showing that the b-value is sensitve to changes in applied stress, to differences in crack density and to the degree of heterogeneity of the materials involved. However, on a macroscopic scale there is still a lack of clear connections between identified inhomogeneities, geological structures, and the physics behind the spatial b-value variations.

This resulted in the major target of this thesis which is testing the usefulness of the b-value as a significantly varying parameter to indicate structural settings which influence the rupture process of a large destructive earthquake. Once this ability is evaluated, it will be varified to what extent the b-value mapping can give the sizes of involved structures to estimate further source parameters. Another major issue is the correlation of the achieved b-value map to other spatially distributed parameters in the fault plane area to constrain ideas about the nature of the identified inhomogeneities. The additional investigated parameters are mainshock moment release (*Delouis*, 1996), isostatic residual anomalies of the gravity field (*Götze et al.*, 1994), aftershock radiated seismic energy (E_s), and v_p/v_s ratios from a local earthquake tomography study (*Husen*, 1999). The significant correlations found here also help to examine the individual aptitude of the parameters mapping out seismogenic structures. Summed moment tensor solutions of aftershocks will give an idea about a possible "topography" on the fault plane indicating the deviation of the main shock rupture from a pure shear mechanism.

As mentioned before, the aspired high resolution requires dense data sets and an appropriate magnitude of completeness. Aftershock sequences have proofed to be an excellent tool possessing these requirements as many events can be registered in a relatively short time. In addition, temporal networks often have a large number of stations with respect to the size of the investigated area. The results obtained here will also contribute some ideas to what extent the post-seismic aftershocks can mirror co-seismic characteristics of the mainshock.

1.2 Aftershocks and the German Task Force for Earthquakes

Aftershock sequences

Aftershock sequences follow large earthquakes and are characterized by high activity rates which decay in time. The sequences can be generally described by the Gutenberg-Richter relation (see Chapter 3) for earthquake occurrence and by the modified Omori law (*Utsu*, 1961), which accounts for the decay:

$$n(t) = \frac{c}{(K+t)^p}. \tag{1.1}$$

In this equation n(t) is the number of events per unit time at time t. c, K, and p are constants which depend on the rate of activity in the earliest part of the sequence, on the total number of events, and give the rate at which the activity decays (*Kisslinger & Jones*, 1991; *Lay & Wallace*, 1995). *Kisslinger & Hasegawa* (1991) found that not all sequences can be described by a single value of these parameters, but that more often several decay rates are needed to describe one aftershock sequence. *Kisslinger & Jones* (1991) investigated 39 aftershock sequences in California to find that the p-value can vary geographically and might be controlled by temperature. *Guo & Ogata* (1995) were able to establish a positive correlation between p- and b-values from the GR relation for aftershocks in Japan. The authors propose a further correlation of each parameter with the fractal dimesion of aftershock hypocenter distributions. Therefore aftershock sequences, also due to their large number of events, provide a tool for mapping spatial and temporal variations of parameters which are expected to contribute to resolve structural inhomogeneities in the fault plane area.

Aftershocks are the reaction on the impact of the mainshock in the fault plane area and therefore can help to deduce information on the mainshock itself. For many large earthquakes, aftershocks have been used to constrain the mainshock fault plane because for a long time it had been quite difficult to obtain this important source parameter from the inversion of teleseismic data only (*Henry & Das*, 2001). Although the fault plane of a large earthquake seems to expand with time, and aftershock activity outside the plane is frequently apparent, the activity in the first stage of the aftershock sequence seems to give a good estimation of the fault plane size.

In a number of case studies it could be observed that low aftershock activity seems to correlate with areas of high mainshock slip (*Mendoza & Hartzell*, 1988; *Beroza*, 1990; *Scherbaum*, 1994). Considering the model of highly stressed asperities as a mechanism for the mainshock and assuming that asperities are areas of high slip, then the aftershocks should occur in response to the stress transfer from the asperities to the surrounding regions (*Beroza & Zoback*, 1993). However, the Antofagasta case study in this thesis points out that this statement might be too general for all aftershock sequences.

These properties of aftershock sequences stated above underline again their importance in gaining knowledge about the earthquake process in general. The acquisition of high quality data sets is necessary to take advantage of this capabilities. Usually such kind of data is availabel in countries running permanent networks with dense station spacings. In recent years portable stations for temporal networks have come into use providing a means to collect data also in remote areas. This is especially important for developing countries where seismological data often is very rare or simply not available. As aftershocks can also help to constrain information on local site conditions (*Scherbaum*, 1994) in many countries the investigation of aftershocks will be the major source for first steps in the reduction of vulnerability.

The German Task Force for Earthquakes

The German Task Force for Earthquakes was founded in March, 1993, with the main aim to achieve a data base of high quality standards in all participating disciplines. The Task Force committee is a multidisciplinary group comprising geosciences, construction engineering, social sciences and economy. The primary goal of the committee is earthquake disaster reduction and mitigation by applying an interdisciplinary concept. The major task of the active groups (seismology, geodesy, hydrology, engeneering) is to arrive in the epicentral area after an earthquake as soon as possible to start data acquisition immediately after the large earthquake had happened. Especially in seismology valuable information can be lost in the early days after the main shock as the aftershock activity decays rapidly with time. Already during the mission the data is sighted and pre-analyzed. After the mission a detailed analysis in each field has to be carried out. Regional aspects on geography, climate and society etc. should be taken into account and should be gathered in an informational pool together with scientific results. This pool should then constitute the basis for advice on preventive measures. So far 13 missions had been attended by the groups of seismology, geodesy, hydrology and engineering in earthquake disasters worldwide (Table 1.1).

Up to now, two outstanding seismological catalogues of aftershock sequences could be produced in terms of number of registered events, precision of hypocenter calculation and resolution of the data set: the catalogue of the Mw=8.0 Antofagasta earthquake which was derived by collaboration with the SFB CINCA'95 project (see also Chapter 2) and the catalogue of the Mw=6.9 Cariaco earthquake which are examined in this thesis. The final catalogues contain more than 2000 and 1300 events respectively for further application of different seismological methods. With both catalogues, regional seismic tomography was performed leading to very high accuracy in hypocenter locations (*Husen*, 1999; *Grosser et al.*, 2001). This leads in both cases to very high resolutions in determining small scale structures of the involved fault segments in the range of 2 - 5 km. This is comparable

List of Task Force missions

year	earthquake	magnitude	country	Task Force groups			
				seismol.	engin.	hydrol.	geodesy
1992	Erzincan	6.8 Ms	Turkey	X	X		
1993	Killari	6.3 Ms	India	X			
1995	Aiyion	6.5 Ms	Greece		X		
1995	Antofagasta	8.0 Mw	Chile	X	X		
1995	Dinar	6.0 Ms	Turkey			X	
1997	Cariaco	6.9 Mw	Venezuela	X	X		X
1998	Adana	6.2 Ms	Turkey		X	X	
1999	Izmit	7.4 Mw	Turkey	X	X	X	X
1999	Düzce	7.2 Mw	Turkey	X	X	X	X
2000	Vogtland swarm	3.7 Mw	Germany	X	X		
2002	Sultandagi	6.5 Mw	Turkey	X	X	X	
2002	Aachen	4.9 Mw	Germany	X	X		
2003	Bingöl	6.4 Mw	Turkey	X	X	X	

Table 1.1: List of large earthquakes where the German Task Force for Earthquakes participated in the emergency response.

to results from investigations of seismicity in California by using the double difference relocation method leading to a resolution of 2 km (*Waldhauser & Ellsworth*, 2002). It is expected that the two data sets from the Mw=7.4 Izmit and Mw=7.2 Düzce earthquakes will overwhelm the previous data sets in total number of available events for further studies. Data processing is similar for all data sets: individual hypocenter calculation for each aftershock also considering events with small magnitudes. This procedure makes the data sets a most valuable base to get information on fault size, orientation and fault structure. These data sets would be suitable also for studying the behaviour in time of the aftershock series and their subsequences which could lead to additional physical understanding of observed processes (*Dieterich et al.*, 2000).

2. Seismotectonic Framework of Study Area

This chapter gives a brief overview on the tectonic evolution in the study area, where the $M_w = 8.0$ 1995 Antofagasta earthquake occurred. As the general aim is the identification of asperities on the main shock fault plane, emphasis will be put on geologic and tectonic structures that could possibly act as stress concentrators, causing the development of asperities in the seismogenic zone. Information on back ground and historical seismicity will be given including the Antofagasta main shock and aftershock sequence. The data compilation, which led to the data basis used for this work, will be described in the last section of the chapter.

2.1 Geological and tectonic setting

The study area in northern Chile (70°W to 71.5°W and 23°S to 25°S, Fig. 2.1) is part of one of the longest coherent subduction zones known worldwide. This convergent plate margin is produced by the movement between the oceanic Nazca plate (NA) and the continental South American plate (SA). The main characterizing features are the deep sea trench (maximum depth of 8000 m in front of the study area, Fig. 2.1), the Wadati Benioff Zone (WBZ) and the impressive Andean orogen, all being consequences of the convergent movement. The shallow part of the WBZ, which hosts the seismogenic zone, shows a dip angle of approximately 20°. Dip angles change within the intermediate and lower part of the WBZ (Fig. 2.2). The entire WBZ, down to about 300 km depth, can be traced by high seismic activity as monitored during various seismological projects with networks covering the Andean arc from the deep sea trench to the Eastern Cordillera between 20°S and 25°S (*Asch et al.*, 1996; *Schurr et al.*, 2003).

Two important parameters, namely convergence angle and convergence rate, control the stress and strain pattern along the edge of the overriding plate and the seismogenic zone and determine the type of igneous activity observed in the upper crust (*Jarrard*, 1986; *Scheuber et al.*, 1994; *Pichowiak*, 1994). These parameters show strong variations in time caused by several changes in plate configuration since the mid Jurassic (160 Ma ago). Plate tectonic reconstructions based on pole rotation and magnetic anomaly data, showed that the Aluk plate subducted beneath continental SA about 100 Ma ago followed by the Farallon plate in late Cretaceous (70 Ma ago)(see small sketch in Fig. 2.1). In late Eocene/early Oligocene (35 Ma ago), the Farallon plate broke up into the Nazca and Cocos plates, producing the recent plate tectonic configuration (*Zonenshayn et al.*, 1984; *Pardo-Casas & Molnar*, 1987).

The angle of convergence obliqueness influences the deformational regime of the overrid-

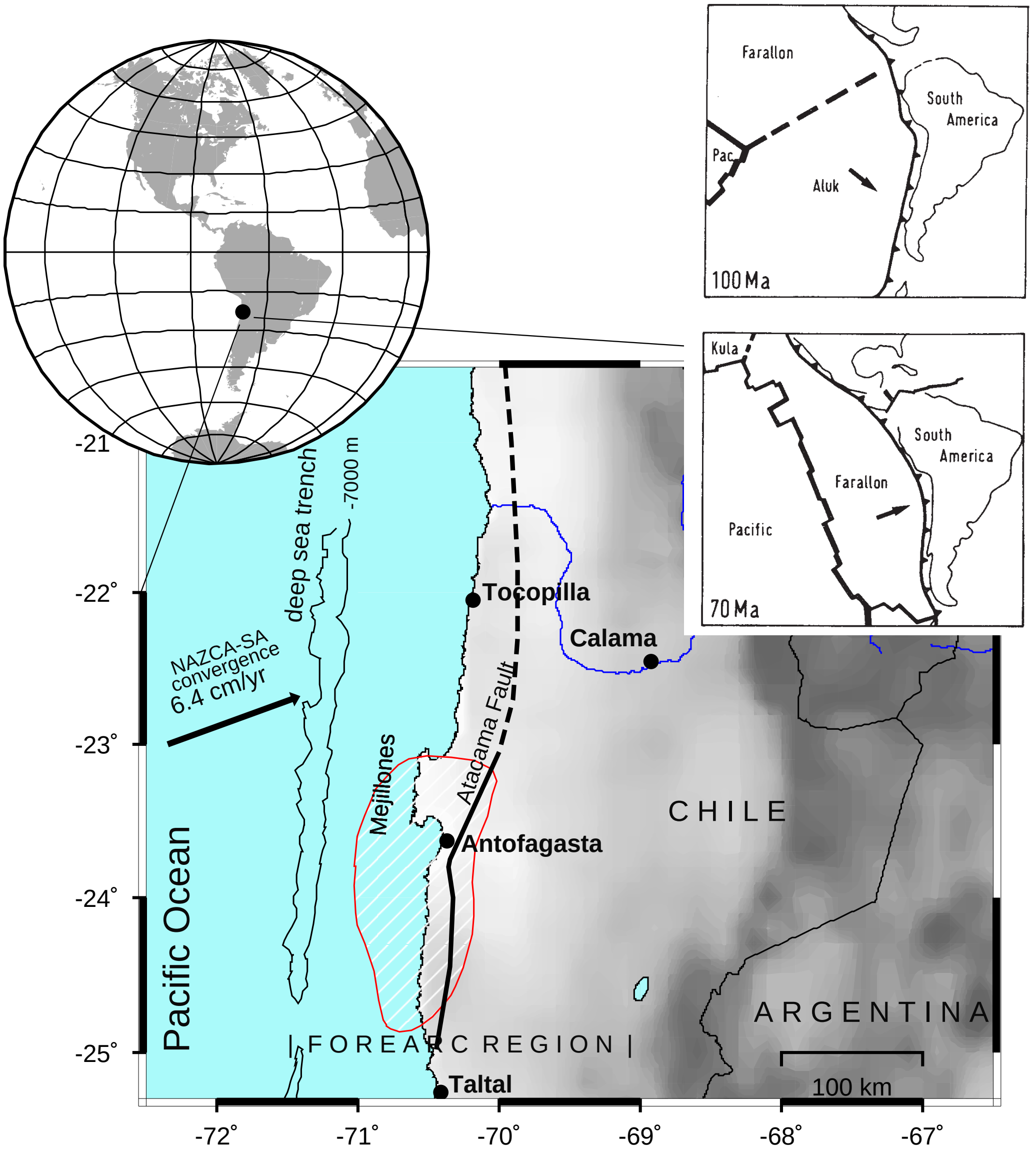

Figure 2.1: The study area in northern Chile. Hatched area marks the proposed fault plane of the 1995 Antofagasta earthquake. The arrow represents the recent convergence direction of the present setting of the Nazca and South American plate. The convergence rate is taken from Norabuena et.al., 1998 and 1999. The small sketches in the upper right corner show the plate tectonic setting 100 Ma and 70 Ma ago (after *Zonenshayn et al.* (1984)).

ing plate at the margin and can cause strike-slip movements parallel to the plate boundary (*Scheuber et al.*, 1994). Convergence obliqueness probably has stimulated the development of the prominent Atacama Fault Zone (AFZ) which is a major tectonic structure of the Coastal Cordillera (Fig. 2.1). It is running parallel to the coast from La Serena to Iquique in northern Chile for ∼ 1000 km, cutting through the Jurassic-early Cretaceaous arc system. Kinematic studies show that the AFZ took up strike slip movements probably from the beginning of early Cretaceous times, developing a ductile to brittle left-lateral fault system (*Scheuber et al.*, 1994, 1995; *Taylor et al.*, 1998). *Taylor et al.* (1998) postulate that the Coastal Cordillera Fault System is forming a strike slip duplex in the area of the outer forearc, incorporating the AFZ and a system of north-northwesterly trending smaller left lateral strike slip faults cutting the continental crust into blocks. The ages dated for active periods of the AFZ show that magmatic and tectonic activities are contemporaneous in the Coastal Cordillera (*Scheuber et al.*, 1994) and magma ascent probably was related to major faults and fault systems. This co-existence of magmatism and formation of faults and the proposed scale of crustal blocks supports the assumption, that the major faults located in the Jurassic-early Cretaceous arc system, such as the Atacama fault, are throughgoing faults that pervade the entire continental crust of the overriding plate. Therefore, they might be considered to influence seismicity patterns not only in the upper crust but also in the seismogenic zone or its adjacent areas.

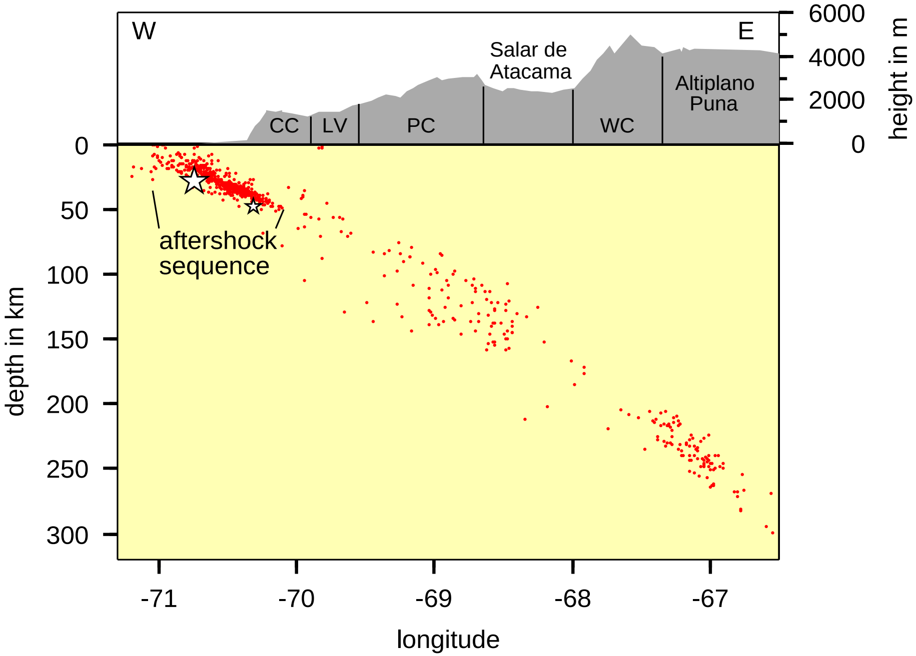

Figure 2.2: The Wadati Benioff Zone (WBZ) in the Antofagasta region as outlined by seismic activity, recorded with the combined CINCA'95 - Task Force network. The aftershock sequence of the 1995 Antofagasta earthquake can be clearly recognized by the dense clustering of hypocenters in the shallow WBZ between 10 and 50 km depth. More diffusive clusters are noticable between 80 and 150 km depth and around 250 km depth, beneath the Altiplano/Puna plateau. A lack of seismicity is seen beneath the active magmatic arc in the *Western Cordillera* (WC). CC=*Coastal Cordillera*, LV=*Longitudinal Valley*, PC=*Precordillera*.

The center of igneous activity of the North Chilean convergent margin has migrated from the coastal area to the east during the Andean Cycle (*Coira et al.*, 1982). It formed four magmatic arc systems whose tectonic settings and strain regimes were influenced by the changes in convergence parameters (*Scheuber et al.*, 1994). These four arc systems are located in the *Coastal Cordillera*, the *Longitudinal Valley*, the *Precordillera* and the

Western Cordillera (Fig. 2.2). Most important for this study is the structure and geology of the arc system in the Coastal Cordillera as it is forming the upper contact of the seismogenic zone of the present subduction interface. This Jurassic-early Cretaceous magmatic activity (200 - 90 Ma ago) in the Coastal Cordillera was characterized by extensive volcanism, plutonism and the intrusion of huge batholiths (*Scheuber et al.*, 1994). Igneous rocks of this time constitute 77% of the Coastal Cordillera. The formations of the El Cobre Batholith and the Coloso Coastal Gabbro Complex (*Pichowiak*, 1994) determine the geological structure in the area of the 1995 Antofagasta earthquake (Fig. 2.3). The batholith is supposed to be a deep reaching structure which might pervade the crust of the overriding SA plate reaching the interface.

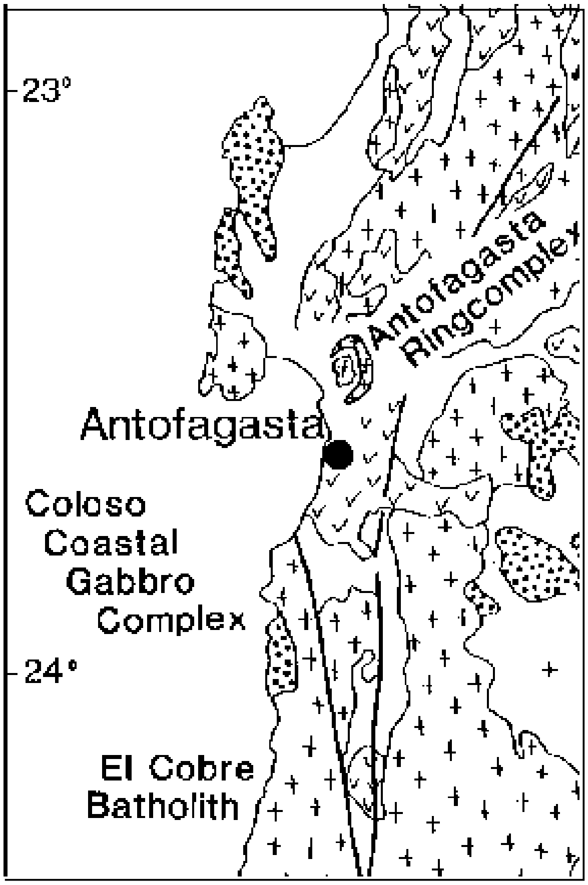

Figure 2.3: Map of Preandean and Andean magmatic rocks in the region of the 1995 Antofagasta earthquake from *Pichowiak* (1994). Crossed areas (+) represent Diorites to Granodiorites which form the deep reaching batholiths in this region like the El Cobre Batholith. The rather small areas of Andesites-Qtz-Tholeiites of the La Negra formation are denoted by vees (∨). Dotted areas are low- to high-grade metamorphic rocks and intrusives of Late Proterozoic to Paleozoic age like the Coloso Coastal Gabbro Complex.

Results from seismic profiling encompassing the area of the Jurassic-early Cretaceous arc (*Wigger et al.*, 1994; *Patzwahl*, 1998; *Patzwahl et al.*, 1999) suggest high average seismic velocities of ∼ 6.6 km/s beneath the Coastal Cordillera which is in accord with a high percentage of igneous rocks in the crust. However, north-south variations in the seismic velocity structure are apparent along the margin. Seismic profiles perpendicular to the coastline at 21° S, 22° S and 23.25° S (*Patzwahl*, 1998; *Hinz et al.*, 1995) reveal several zones of high and low seismic velocities which are attached to or forming part of the interface. One of these profiles north of Mejillones Peninsula is shown in Fig. 2.4 (top). The identified zones are interpreted as either underplated material eroded from the upper continental plate, or as oceanic material deposited on top of the actual interface.

On a profile crossing Mejillones Peninsula at 23.25° S (Fig. 2.4, bottom) these zones are absent. As one possible interpretation *Patzwahl* (1998) proposes an increase of an additional load from north to south caused by continental rocks hosted in the overriding crust that "squeeze" the interface and its adjacent areas. Such additional loads could be represented by the large batholiths and plutones identified in the geological map (see Fig. 2.3). Local tomography studies realised with the aftershock sequence of the 1995 Antofagasta earthquake (*Husen*, 1999; *Patzig*, 2000) also show structures of high seismic velocity. A very pronounced extended structure of 7.0 to 7.5 km/s appears around 24° S which seems to pervade the upper crust and interface (see Fig. 2.5).

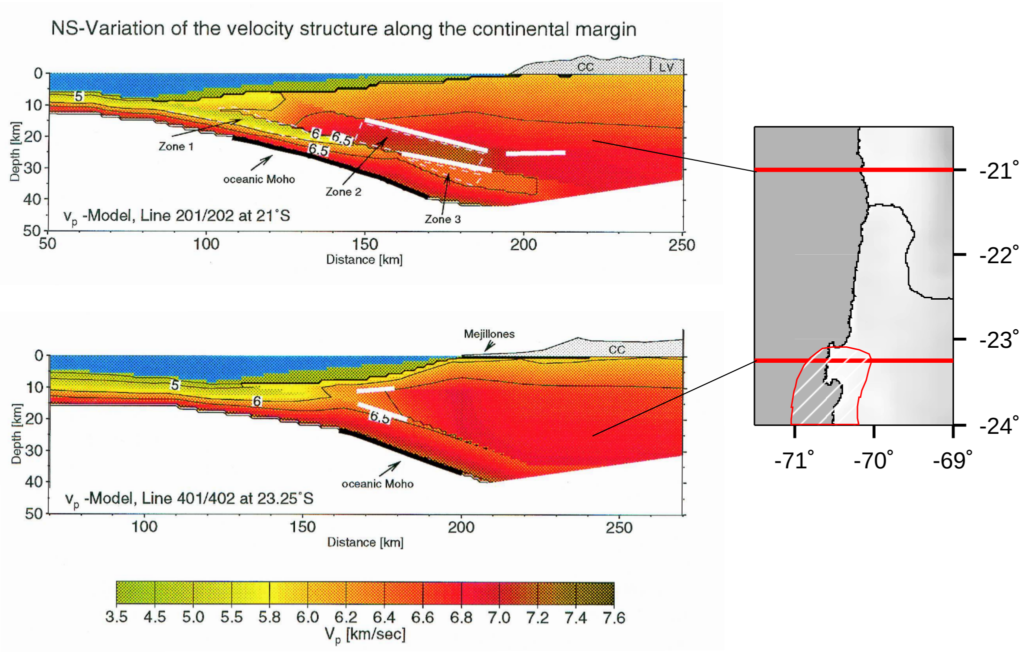

Figure 2.4: Modeling results of east-west seismic profiles at 21° S and 23.25° S (small sketch at the right shows geographical locations of the profiles), focusing on north-south variations in the velocity structure of the upper crust and the interface. Zones 1-3, marked on the northern profile, are missing entirely in the southern profile.

Retreat of the continental front, lack of sediment coverage on the continental slope and the deep sea trench, and the pronounced horst and graben structure of the downgoing oceanic plate led a number of investigators to suggest an erosional character for the north Chilean margin (*Scheuber et al.*, 1994; *von Huene et al.*, 1999; *von Huene & Ranero*, 2003; *Hinz et al.*, 1995). High resolution images from swath bathymetry of the continental slope and the deep sea trench were interpreted by *von Huene et al.* (1999); *von Huene & Ranero* (2003) (see Fig. 2.7). They propose that debris from a steepened midslope is sliding into the trench, filling the graben before they subduct beneath the frontal prism. This elevates the pore fluid pressure and consequently reduces friction at least in the shallow part of the interface (0 to ~ 20 km depth). How this situation continues downslope or whether friction increases rapidly with depth towards the seismogenic zone, is still an unresolved question. Yet no satisfactory conclusion for the friction related seismic coupling (*Scholz*,

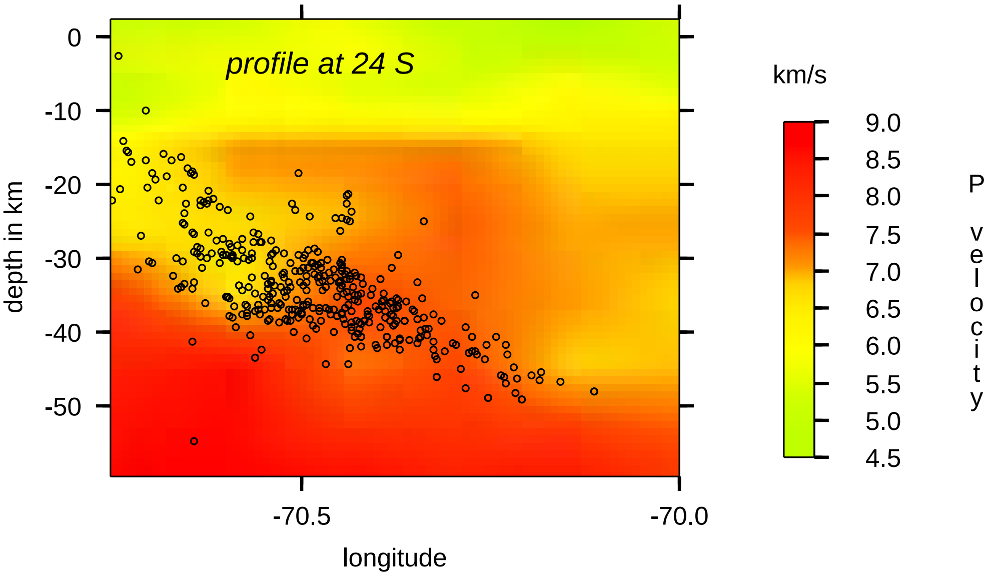

Figure 2.5: 3D tomographic cross section at 24° S showing absolute vp velocities from *Husen* (1999). The profile exhibits a massive high velocity structure (vp 7.0 to 7.5 km/s), which starts at about 15 km depth and seems to pervade the upper crust and interface between overriding and subducting plate. Black circles give aftershock hypocenters in the vicinity of the profile. The upper limit of the hypocenters is interpreted to be the upper limit of the interface.

1990) is given, also not whether or how it varies in time and space along the interface.

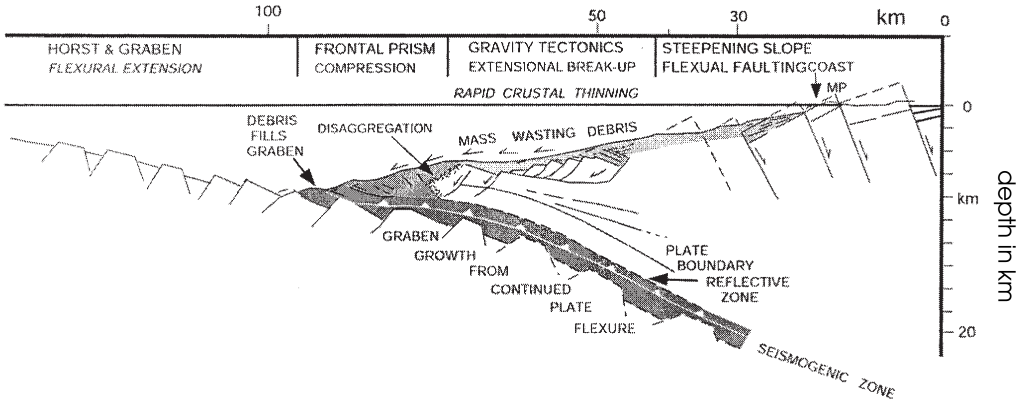

Figure 2.6: Model to explain subduction erosion at the north Chilean margin from *von Huene & Ranero* (2003). The horst and graben structure and a slight kink in the subducting plate at 10 km depth are obvious. MP denotes Mejillones Peninsula.

Reflection seismic data (*Hinz & others*, 1998) reveal a first steepening of the subducted oceanic plate at about 10 km depth. Here the observed angle already adopts a value of $\sim 20°$ which is the same as the dip angle of the adjacent seismogenic zone. At 10 km depth, the horst and graben structure is still visible (Fig. 2.6). A peculiar feature of the continental slope is the Antofagasta ridge (Fig. 2.7). It is a morphological high, situated on the midslope area at 24° S and interpreted to be similar to the Mejillones Peninsula, (*von Huene et al.*, 1999). Both features, Mejillones Peninsula and the Antofagasta ridge, are discussed by *Delouis et al.* (1998) and *von Huene & Ranero* (2003) as the edges of seaward tilted blocks of the continental crust.

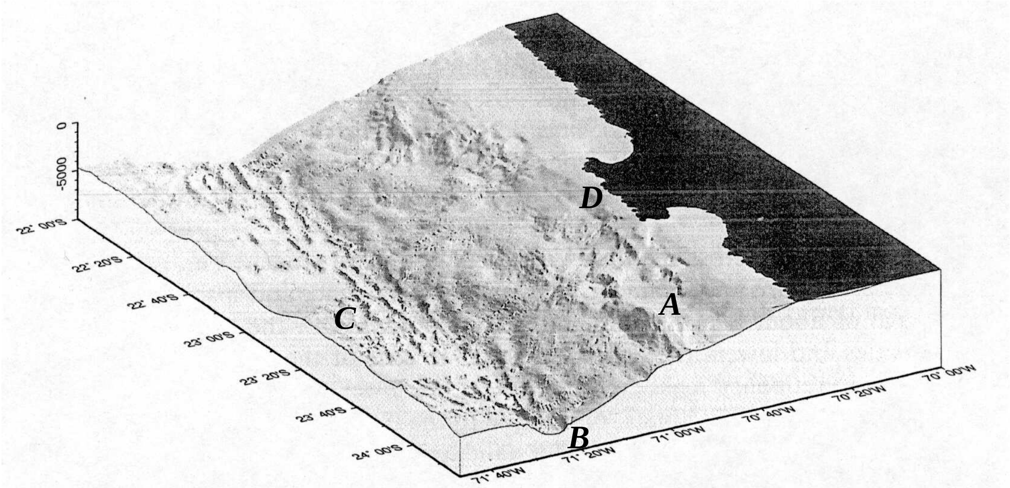

Figure 2.7: High resolution swath bathymetry of the continental slope and deep sea trench (B) off the coast of Antofagasta and Mejillones Peninsula (D) from *von Huene et al.* (1999). The letter A denotes the Antofagasta ridge (see text for further explanation). East of the trench the horst and graben structure (C) is well established in the ocean bottom topography.

The gravity map (*Götze et al.*, 1994) shows a pronounced gravity high of up to 100 mGal along the coastline of the Antofagasta region, forming an elongated chain of anomalies. These anomalies are attributed to igneous bodies of high density within the upper crust of the forearc region and are observed not only locally in northern Chile but characterize the entire Pacific coast of South America. The co-existence of elongated gravity highs above seismogenic zones with high level background seismicity is reported also from other subduction environments, e.g. the Sunda Arc, Alaska Peninsula and Japan (*Wells et al.*, 2002). Investigations of the isostatic residual field in northern Chile exhibit high residual values (up to 150 mGal) in the same coastal area with some extension to the east, thus covering the range of the Coastal Cordillera (*Götze & Krause*, 2002). This belt of positiv isostatic anomalies had been interpreted as a superposition of local and regional mass distributions. In the Antofagasta area they are caused by the uplifted Jurassic batholiths, namely the El Cobre Batholith and the Coloso Coastal Gabbro Complex (*Pichowiak*, 1994) (see Fig. 2.3), which intruded into the Formación La Negra (*Götze & the MIGRA group*, 1996; *Götze & Krause*, 2002). These batholiths will play an important role again for the interpretation of the results gained in this thesis (see Chapter 3, Fig. 3.23). Table 2.1 gives a summary of the previously described and observed structural inhomogeneities in the Antofagasta region which might be of importance for the development of the rupture plane of the 1995 earthquake.

seismics	*geology*	*gravimetry*	*bathymetry*	*tomography*
north-south variations of velocity structures in the upper crust along the margin, high and low velocity zones disappear beneath Mejillones Peninsula, Fig. 2.4	identification of plutonic structures, namely the El Cobre batholith and the Coloso Coastal Gabbro Complex, Fig. 2.3	gravity highs of up to 100 mGal as chain of anomalies along the coastline, isostatic residual anomalies of up to 150 mGal in the same area, Fig. 3.23	confirmation of the erosional character of the convergent margin, identification of Antofagasta ridge at 24° S, Fig. 2.7	pronounced areas of high seismic velocities, extended structure at 24° S, Fig. 2.5

Table 2.1: List of observed structural inhomogeneities in the area of the 1995 Antofagasta earthquake which might have influenced the rupture process.

2.2 Seismicity and the seismogenic zone

Subduction zones usually are characterized by a high level of seismic activity over a wide range of magnitudes. Most of the large subduction earthquakes occur in the upper part of the WBZ between approximately 10 and 60 km depth. This seismogenic zone is the contact zone between the subducting and the overriding plate, where coupling is supposed to be stronger than anywhere else along the WBZ. The parameter of seismic coupling (C_s) seems to play a key role in producing large magnitude earthquakes with high moment releases. *Scholz* (1990) defined the strength of seismic coupling as the seismic moment rate released by seismic events ($\dot{M}_{os}$) divided by the seismic moment rate calculated from geological ($\dot{M}_{og}$) data $C_s = \dot{M}_{os}/\dot{M}_{og}$. In terms of rate and state dependence of an earthquake rupture process, C_s depends on friction in the seismogenic zone. Friction, on the other hand, is related to the force F_i, which is normal to the interface (*Scholz*, 1990; *Uyeda & Kanamori*, 1979). Seismogenic coupling can vary in space and time throughout the seismogenic zone, having increased values on patches called asperities. This is the main assumption for the asperity model developed by *Lay & Kanamori* (1981) for large earthquakes in subductuion zones. This will be addressed in Chapter 4 in detail. Modeling attempts by *Dmowska et al.* (1996) and *Taylor et al.* (1998) showed that heterogeneous coupling, which is interpreted in terms of asperities, can result in complex distributions of co- and post-seismic stress changes. So far, not very much is known about the heterogeneity of coupling in the North Chile subduction zone aside from the general assumption of various authors that it is strongly coupled (e.g. *Jarrard* (1986); *von Huene & Ranero* (2003) among others). Most of the geodetic investigations, where GPS or InSAR data is used to achieve slip and deformation rate, assume a 100% coupled seismogenic zone.

The lower limit of the seismogenic zone in the area between 20° S and 25° S is quite well constrained from investigations of local seismicity (*Comte & Suárez*, 1993; *Comte et al.*, 1994; *Delouis*, 1996; *Delouis et al.*, 1997). The authors derive a lower limit at approximately 45 to 50 km depth for northern Chile. *Tichelaar & Ruff* (1991) used teleseismic data and achieved a depth range between 36 - 41 km for the lower limit of the seismogenic zone in an area north of 28° S, and 48 - 51 km for the area immediately south of this latitude. All these investigations are based on the assumption that events with thrust mechanisms are attributed to the seismically coupled zone and that the downdip limit is determined by a change in the stress field yielding mechanisms different from thrust. The study of *Delouis* (1996) delivered a fairly precise picture of the changing stress field along the WBZ between 22° S and 25° S, subdividing the seismogenic zone in a shallow part from 20 to 35 km and a deeper part from 35 to 50 km depth. The depth distribution of the aftershock sequence investigated in this work shows a change in character at 50 km depth from tightly clustered events to a more diffuse and sparse distribution below 50 km. This can be taken as a confirmation of the lower limit of the seismogenic zone at 50 km depth. The identification of the upper limit of the seismogenic zone is more difficult, but most authors conclude it to be at ∼20 km depth in the Antofagasta region (*Delouis*, 1996; *Husen*, 1999; *von Huene & Ranero*, 2003).

The entire WBZ of the study area (23° S to 25° S) can be traced by seismicity recorded after the 1995 Antofagasta earthquake down to ∼300 km (Fig. 2.2). However, the character of the spatial distribution of hypocenters changes along depth. Besides the pronounced cluster of the aftershock sequence in the shallow part (0 - 50 km), a more diffuse cluster, located beneath the *Precordillera* appears between 80 and 150 km depth. Another cluster around 250 km depth, is situated beneath the *Puna* plateau. A zone of considerably lower seismic activity can be found adjacent to the aftershock sequence in ∼50 and 80 km depth. This gap in Fig. 2.2 does not exist in seismicity recorded between 1990 and 1991 (*Delouis*, 1996). The observation refers to possible stress changes along the WBZ caused by the main shock event (*Taylor et al.*, 1998; *Dmowska et al.*, 1996). The suggestion is supported by SAR and GPS data. *Xia et al.* (2003) observed a change in deformation directions in the 50 to 80 km depth range within three months after the mainshock. Obviously as a consequence, an earthquake of Mw=7.0 occured in 1998 in the area at 55 km depth (see also Fig. 2.9) (*Chlieh et al.*, 2004). A second zone of reduced seismicity is located between 150 and 200 km depth. This zone is attributed to the recent volcanic arc and thus a more or less stable feature of the WBZ.

Dmowska & Lovison (1992), *Dmowska et al.* (1996) and *Taylor et al.* (1998) succeeded to show that strongly heterogeneous slip, attributed to asperities in subduction zones, influences the occurrence of outer rise, downdip and upper plate seismicity in various stages of the seismic cycle. The authors found that the distribution of these stress changes depend on parameters like slip obliquity, dip angle of the slab, width of the seismogenic zone, and friction along the interface. These circumstances can produce increase or decrease in stress or might create stress shadows. Such a stress shadow could serve as a probable explanation for the almost total lack of upper plate seismicity above the seismogenic zone in the Antofagasta area. This lack of seismicity in the upper crust of the forearc region seems to be a local effect which changes north of ∼ 20° S according to *Martinod et al.* (2002), where crustal seismicity is abundant again.

The map of historical seismicity (Fig. 2.8) in northern Chile (17° S to 30° S) exhibits three very large earthquakes: the Arica event in 1868, the Iquique event in 1877 and the Taltal event in 1922. *Kausel* (1986) assigned an Mw=9.0 and Mw=9.1 to the Arica and Iquique events respectively, estimated from macroseismic information. According to *Comte et al.* (1994) the seismic cycle in this area is, approximately, between 100 and 120 years which makes the Iquique fault plane area of 1877 a seismic gap. Several authors (*Delouis et al.*, 1997; *Sobiesiak*, 2000; *Xia et al.*, 2003) propose that the 1995 Antofagasta earthquake caused an additional stress on this 1877 gap, which might bring it nearer to

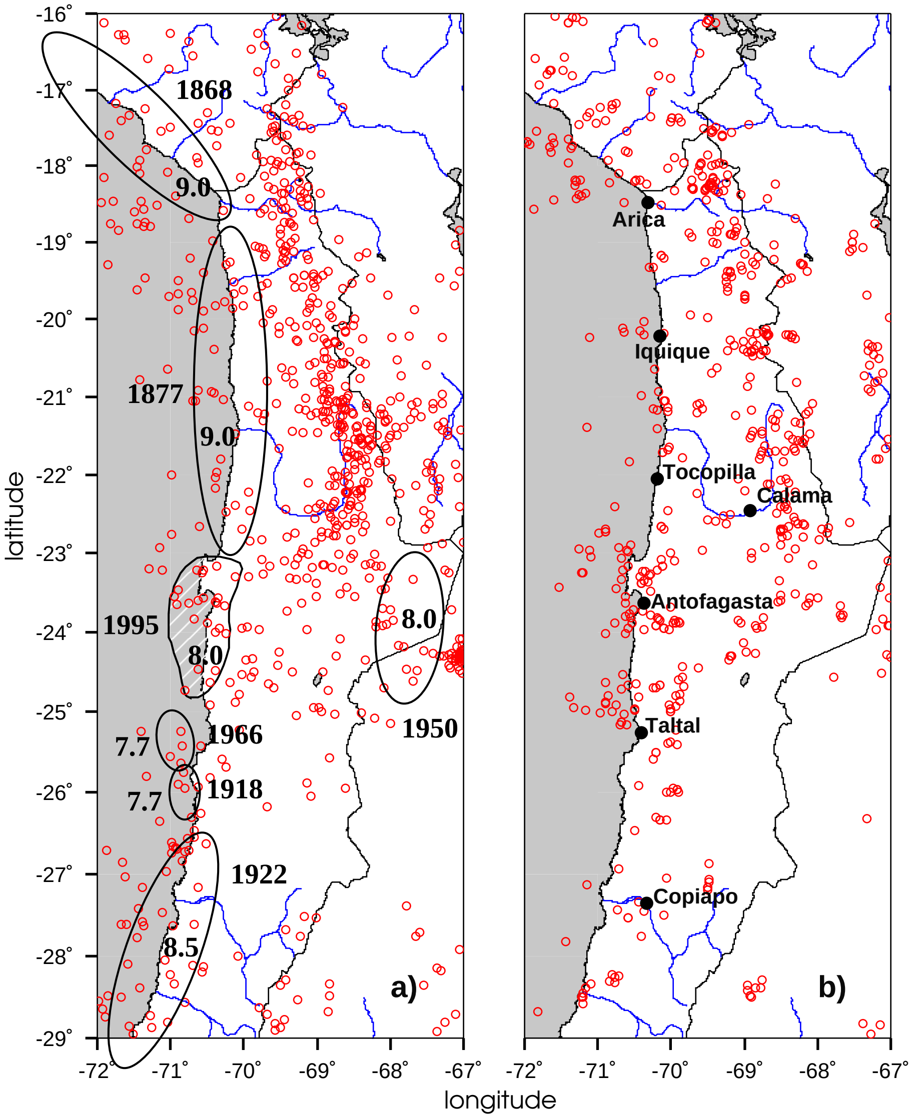

Figure 2.8: Historical seismicity in northern Chile and adjacent areas. The assumed rupture planes are given together with their year of occurrence and proposed magnitude (after *Kelleher* (1972); *Kausel & Campos* (1992); *Delouis et al.* (1998)). Red circles visualize the background seismicity between 1990 and 1995 (a), and between 1996 and 2002 (b) (taken from ISC catalogue).

failure. The southern limit of the estimated fault plane of the 1877 event is located in the northern part of Mejillones Peninsula. The 1995 Antofagasta event started in the southernmost part of Mejillones Peninsula. This led to the suggestion, that Mejillone Peninsula acts like a structural "barrier" on earthquake rupture propagation (*Delouis et al.*, 1997; *von Huene et al.*, 1999). The seismogenic zone between southern Mejillones Peninsula and the northern tip of the 1922 Taltal fault plane seems to rupture in smaller portions, releasing energy in magnitude 7 to 8 earthquakes. A very peculiar event is the 1950 intermediate depth normal fault earthquake of M_w = 8.0 about 100 km east

agency	*longitude*	*latitude*	*depth*	M_w	M_s	*origin time*
NEIC	-70.31	-23.34	45.6 km	8.0	7.3	05:11:23.6
Harvard	-70.74	-24.17	28.7 km	8.0		05:11:56.9
local	-70.48	-23.43	36.0			05:11:23.7
ISC	-70.21	-23.30	42.6		7.4	05:11:23.37

Table 2.2: Hypocenter determinations for the 1995 Antofagasta earthquake calculated by different agencies.

of Antofagasta, having aproximately the same fault plane size as the 1995 Antofagasta event. *Kausel & Campos* (1992) determined the source parameters by modeling long period body waves which resulted in a source time function with two major subevents. The first subevent was localized at 80 km and the second one at 95 to 100 km depth which puts this earthquake at the lower limit of the 50 - 80 km depth zone with changing postseismic deformation after the 1995 Antofagasta earthquake as mentioned above (*Xia et al.*, 2003; *Chlieh et al.*, 2004). *Kausel & Campos* (1992) speculated, by taking into account cyclic coupling and decoupling of the north Chilean seismogenic zone, that this 1950 tensional event should have been followed by a large thrust event in the shallow WBZ which could have been the 1995 Antofagasta event. In consequence the recurrence interval of large thrust events in the seismogenic zone of northern Chile must be influenced not only by N-S directed stress changes parallel to the margin but also by stress changes along depth of the intermediate WBZ.

Spatial and temporal variations apparent in local seismicity of events with magnitudes M>5 can be seen in Fig. 2.9. Between 1990 and 1995 (*Delouis*, 1996; *Delouis et al.*, 1997) the events are grouping around the fault plane of the 1995 Antofagasta earthquake (Fig. 2.9a). The large aftershocks, which occurred between August and December 1995, are concentrating on the upper left corner of the fault plane. This could be proposed as stress concentration after the large main shock (Fig. 2.9b). Fig. 2.9 c) and d) display the fault plane solutions of the Harvard and PDE catalogues between 1996 and 2002. The assigned numbers to some events show that these are pairs of solutions given for one event, where the PDE and Harvard determinations might define the fault planes of these events. It is interesting to note that after 1996 fault planes of adjacent hypocenters rupture again into the fault plane area of the 1995 event. This might refer to the beginning of healing of the 1995 rupture.

2.3 The $M_w = 8.0$ July 30, 1995 Antofagasta earthquake

On July 30, 1995 a strong thrust earthquake occurred in the seismogenic zone beneath the northern Chilean city of Antofagasta at 05:11:23.5 origin time (Harvard catalogue). Table 2.2 compares various hypocenter determinations calculated by different agencies. We used the NEIC location and the centroid moment tensor solution (CMT), calculated by Harvard (*Dziewonski et al.*, 1996), to achieve a first idea about the rupture propagation.

As NEIC determines hypocenters by using first motion phase arrivals, their solutions

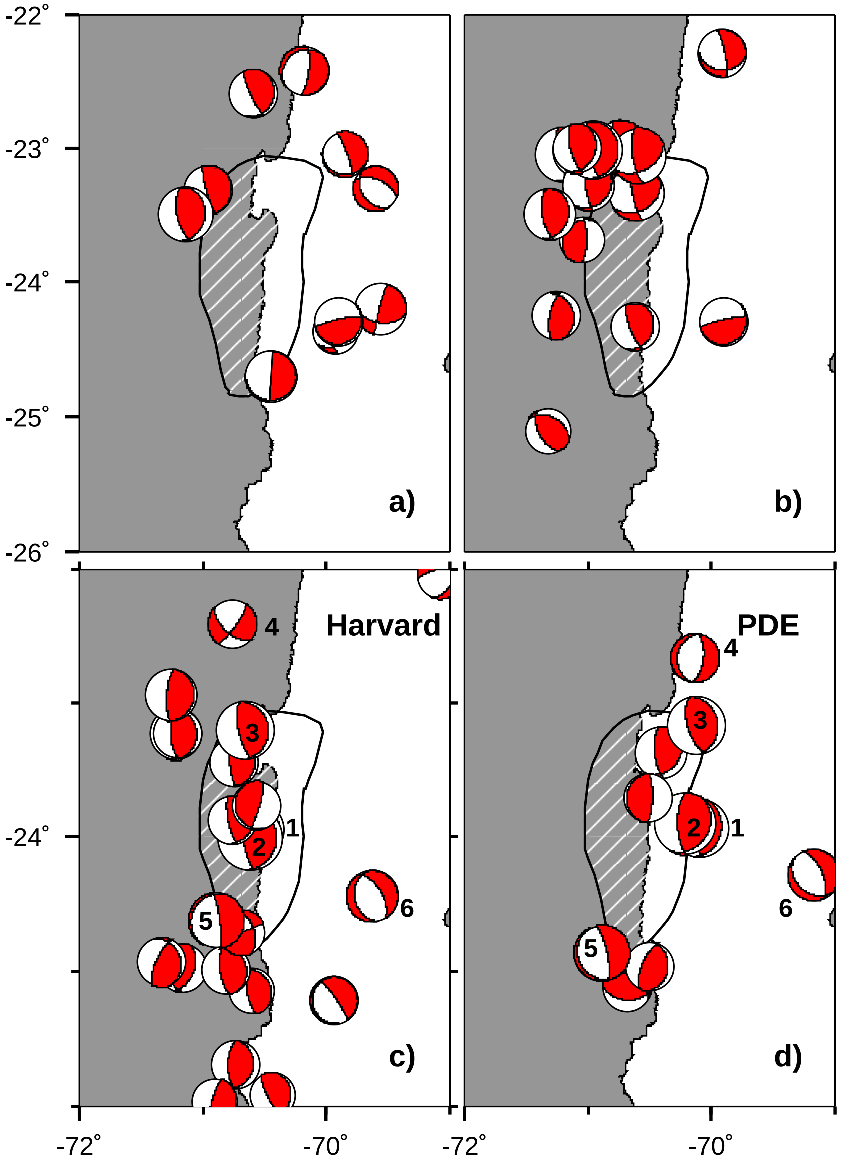

Figure 2.9: Fault plane solutions for M>5 events (a) between 1990 and 1995, (b) between August 1995 and December 1995, (c) and (d) between 1996 and 2002. All events are taken from Harvard and PDE catalogues. See text for further explanation.

are related to the start of the rupture. The CMT solution is the simultaneous inversion of two long period wave trains and thus yields the center of deformation. Plotting both solutions (see Table 2.2 and Fig. 2.10) reveals that the rupture started underneath southern Mejillones Peninsula at $\sim$ 46 km depth and propagated simultaneously southward and upward towards the trench. The southward propagation is corroborated by the directivity obtained from seismogram inversion of teleseismic recordings (*Ruegg et al.*, 1996) and by body-wave modeling (*Delouis et al.*, 1997), which gave a $N200°E$ southward propagation direction at 2.8 km/s. The earthquake was a multiple event composed of at least three major sub-events according to the source time function of *Delouis* (1996) which will be used for the sudies in the present work (see also Fig. 3.22 and Fig. 4.5 in Chapter 3 and 4). Nearly 85% of the total moment was released in the first two sub-events on the northern half of the fault plane (*Delouis*, 1996). The extention of the fault plane was estimated in this work using the aftershock distribution, leading to a value of 15445 km^2 (Table 4.1). The dip of the fault plane is also constrained by the aftershock distribution in depth to $\sim 19°$ towards the east. For comparison and discussion of fault plane parameters of various authors see also Table 4.3 in chapter 4. The CMT source mechanism for the main shock (*Dziewonski et al.*, 1996) is due to thrust faulting with a dip of 22° of nodal plane A for the best double couple (see also Table 5.4, chapter 5).

Some particular observations can be stated for the 1995 Antofagasta earthquake: Despite its large moment magnitude of M_w=8.0 (NEIC, Harvard, ISC), only three fatalities, 58 injured (ISC), and relatively minor damage to buildings was reported. A rather small tsunami wave had been generated with a maximum hight of 130 cm (*Ruegg et al.*, 1996) at Antofagasta and 55 cm at Valparaiso (ISC). *Ruegg et al.* (1996) and *Delouis et al.* (1997) suggest that radiation of seismic energy at very low frequencies could serve as an explanation for the previous observations. The authors identified two peaks in displacement spectra at 65 and 130 s (*Ruegg et al.*, 1996), which could have caused the small $M_s(7.3)/M_w(8.0)$ ratio. From a VBB record of a station at the city of Iquique, they further suggest a slow start of the rupture process. Only a view coseismically induced surface features were identified by *Delouis et al.* (1997) in a field survey after the main shock which were mainly related to the Atacama fault system. Besides these scarps and vertical offsets of some centimeters, *Ortlieb et al.* (1996) found permanent coastal uplifts of 30 to 40 cm at southern Mejillones Peninsula, 2 to 5 cm at Antofagasta and 12 to 22 cm at Caleta Coloso.

2.4 Aftershock sequence and joint CINCA'95 - Task Force network

The CINCA'95 project (Crustal Investiagtions on- and offshore Nazca/Central Andes) was set up to investigate the continental margin of northern Chile within the framework of the SFB 267 (Collaborative Research Center 267) "Deformation Processes in the Central Andes". The experiment was carried out between July and October 1995. Several German and Chilean institutions participated in the onshore field campaign (Free University, Berlin; GFZ Potsdam; Universidad Catolica del Norte, Antofagasta; and Universidad de Chile, Santiago). On bord the German research vessel RV Sonne the Federal Institute for Geosciences and Natural Resources (BGR, Hannover), and GEOMAR (Kiel), were responsible for the marine part of the experiment. During the initial phase of the active field program, the $M_w = 8.0$ 1995 Antofagasta earthquake happened on 30th of July. Immediately after the earthquake the decision was taken to change the planned network layout for 22 PDAS stations of the CINCA project in favour of a temporary network to register the aftershock sequence. The German Task Force for Earthquakes contributed to the newly defined aim with 13 additional REFTEK stations. A very important aspect of the network was its seaward extension with 9 OBH stations (Ocean Bottom Hydrophones) of GEOMAR, Kiel. As a considerable amount of aftershocks was located directly underneath the coast and the offshore continental slope, the OBH's played a major role in improving

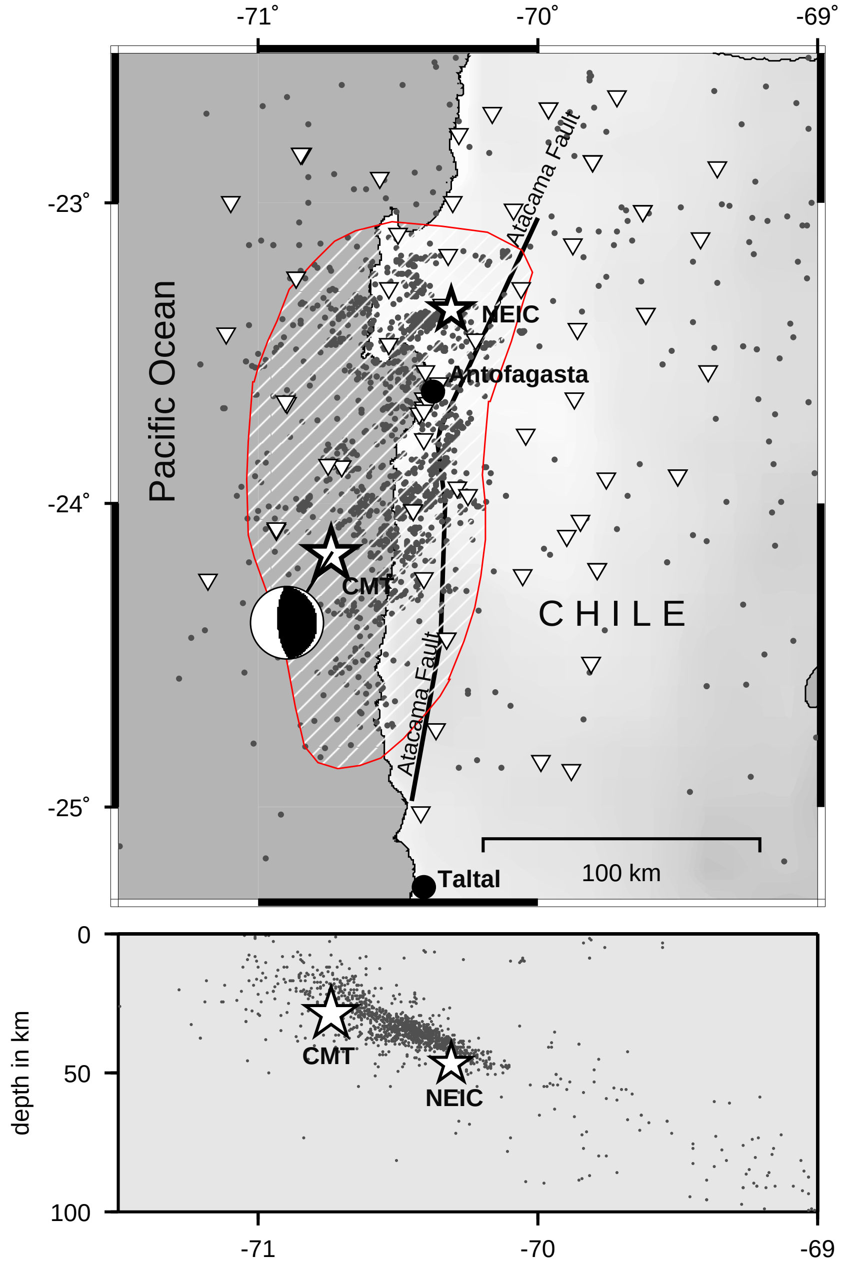

Figure 2.10: Aftershock sequence, infered rupture plane, and fault plane solution of the $M_w = 8.0$ 1995 Antofagasta earthquake. Triangles give station locations of the joint CINCA'95 / Task Force network. The stars mark the hypocenter determinations for the main shock by NEIC and Harvard (CMT). The lower part of the picture shows a vertical depth profile perpendicular to the rupture plane, where the cluster of the aftershock sequence can be clearly distinguished.

the precision in aftershock hypocenter determination.

The final configuration of the combined on- and offshore network covered an area of approximately 250 km in NS direction and 200 km in EW direction (Fig. 2.10). The thirty-five land stations had a spacing of ∼ 15 km around Antofagasta and ∼ 20 km in the southern part and on the outskirts of the network. All onshore stations were equipped with Mark L4-3D seismometers which are three component 1 Hz type of sensors. The OBH positions had a spacing of ~30 km between 22.7° S and 24.3° S. Each OBH was operated with a single hydrophone, positioned 1-2 m above the seafloor. In the city of Antofagasta, 6 additional Kinemetrics ALTUS K2 strong motion recorders were installed for investigating engeneering purposes. These instruments were operated in triggered mode to register only the stronger aftershocks. All other on- and offshore stations registered contineously with a sampling rate of 100 Hz. The landbased network was operated for 52 successive days starting with the deployment of the first PDAS stations on 8th of August. They were followed by the first REFTEK stations on the 10th of August. The strong motion instruments were installed in Antofagasta on the 11th of August (Asch, 1995, internal report). The marine part of the network started to record on the 11th of September for a period of 15 days and was re-deployed for another period of 13 days (*Husen*, 1999). A detailed list of station names and sites is given in *Husen* (1999).

The aftershock sequence, as recorded with the previously described network, constitutes the basis for the investigations of the M_w=8.0 Antofagasta earthquake carried out in this work. During the two months of operation, the network recorded approximately 15000 events with a daily average of 200 to 300 events. The final catalogue for further studies holds ~7500 events, which satisfied the criterion of being triggered by at least 15 stations. For 1728 events (*Husen*, 1999) we were able to determine precise hypocenter locations. 1302 events of this sub-catalogue were used to derive the spatial b-value distribution as shown in Chapter 3. These 1302 events confine the area of highest hypocenter density in the seismogenic zone of the subduction interface. Based on this hypocenter concentration in the seismogenic zone, the conclusion was drawn, that the aftershocks do constrain the mainshock fault plane and that hypocenters of adjacent areas downdip the WBZ are events that belong to the usual background seismicity. *Delouis et al.* (1997) interpret a sharp east-west alignment of aftershocks at approximately 23.3° S in the first 20 hours after the main shock, recorded by the Chilean permanent local network, as the northern limit of the main shock fault plane. In our data set such an east-west alignment of aftershock hypocenters is also apparent just a little further to the south at ~ 23.4° S. Taking these alignments as a northern boundary of the fault plane, consequently the hypocenters north of the boundary do not belong to the fault plane anymore and might be caused by stress transfer from the rupture plane to the adjacent area in the north (Fig. 3.20, Chapter 3).

The histogram in Fig. 2.11 I shows the distribution in time of the 1302 aftershock events. It consists of two seperate observation periods A (19 days) and B (18 days) with 618 and 684 events respectively. The increase of events per day in the first week after the 11th of August is probably due to the ongoing deployment of stations. On the 18th of August the number of events reaches the average value of 38.4 events/day for the remaining period of 30 days. A typical decay in time of an aftershock sequence, according to the law of Omori, cannot be observed in this part of the sequence. There could be three reasons responsible for that:

- According to the histogram, the network started full operation on the 18th of August, which is 19 days after the main shock on 30th of July. Thus the expected strong decay with large magnitude events might have vanished already.
- The histogram displays a data set which consists of events, meeting a certain quality

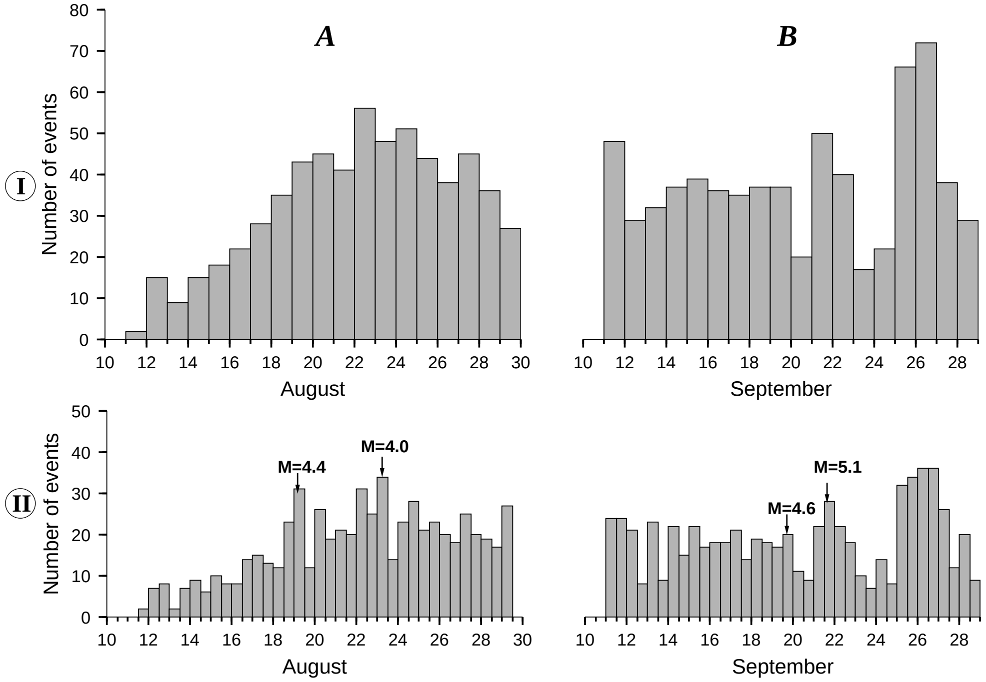

Figure 2.11: Histograms for the aftershock time sequences used in this study. I: Distribution of events per day, II: events per half day.

criteria for further studies and thus is a filtered data base, at least for magnitudes < 1.5.

- It could be possible, that if the decay rate is small, it cannot be resolved in the time sequence presented. Such longterm decay rates are observed especially following large earthquakes, resulting in an elevated level of background seismicity, which might last for several years.

The histogram of M>4 events taken from the ISC catalogue between 1990 and 1998 (Fig. 2.12) shows that obviously none of the listed explications apply. Here the Antofagasta aftershock sequence has a pronounced peak in number of events followed by a rapid decay of not more than half a year where the activity drops back to normal background activity defined by the rate in the years before the 1995 Antofagasta event. Despite this fast decay the period of the network operation lies well within the elevated rate of activity. Therefore the form of the histograms for sub-sequence A and B (Fig. 2.11) should result from a kind of "zoom"-effect which might cover the decay-effect. However, the histograms display different magnitude ranges; so including smaller events as in sub-sequence A and B could yield different decay rates than looking at large events only.

The second histogram in Fig. 2.11 II shows the same data set of 1302 aftershocks but for number of events per half day. This gives a higher resolution to detect sub-aftershock sequences that might be triggered by larger aftershocks. Two such events can be identified in sequence B: the peak on the second half of the 19th of September can be attributed to an aftershock of M_L=4.6 followed by an Omori-like decay in activity on the 20th and 21st of September. The peak on the second half of the 21st was probably caused by an

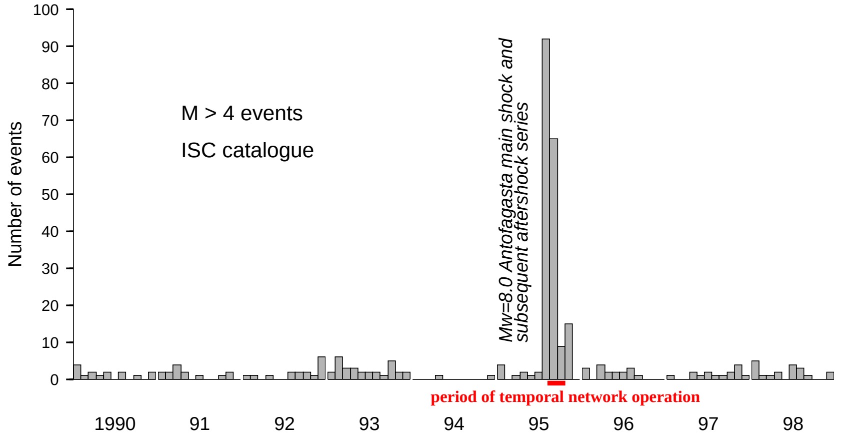

Figure 2.12: Number of events between 1990 and 1998 of M>4 events from the ISC catalogue. Note the sharp peak created by the aftershock sequence of the Antofagasta earthquake. The red bar marks the operation period of the joint CINCA'95 and Task Force network.

M_L=5.1 event. No significantly larger aftershock could be linked to the unusually active period from 25th to 27th of September. The mean magnitude of this period is M_L=1.8.

Several interesting features can be noticed in a 3D hypocenter distribution of the two sequences A and B. Both show a major spatial seperation of the aftershocks into two branches of activity, splitting up at a depth of ~40 km. The hypocenters give the impression that they are following track lines up to a depth of 25 km depth, where the centroid solution of the main shock is marking the center of the rupture (Fig. 2.13). The shallow activity seems to be more dispersively distributed. In the later sequence B, the southern branch of activity shows sharp contours on the upper edge but the area between the two branches now shows more diffusively distributed events. At depth the strong clustering of hypocenters continues. Such temporal variations in the spatial distribution of the aftershocks are also documented in aftershock hypocenters determined by *Delouis et al.* (1997). According to their images, the hypocenters of the first 20 hours after the main shock show more dispersion than the aftershocks in a later time sequence.

2.5 Data compilation and processing

2.5.1 *Pre-processing*

The pre-processing procedure began with the download of the data from the station storage devices to SUN workstations in the Antofagasta field headquater. This involved a visit to each station every 6 days. A data volume of 2.4 GByte was recorded every day and archived on CD-ROM. In case of the OBH stations, the data was stored on DAT devices and downloaded to SUN workstations on board the RV SONNE (*Husen*, 1999).

Already during station deployment, approximately 300 events were analysed and hypocenters determined to achieve an idea about the spatial development of the after-

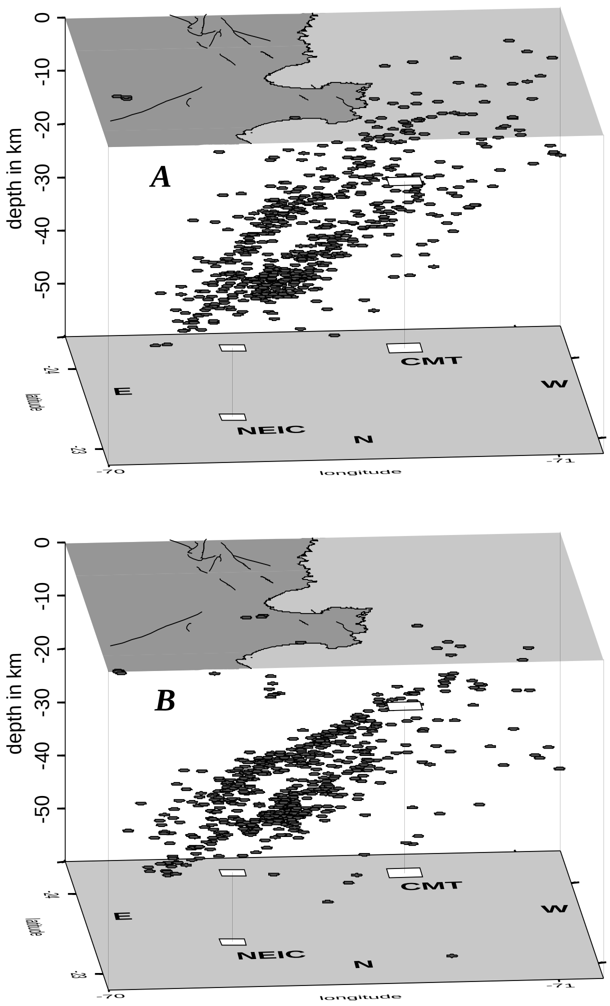

Figure 2.13: 3D image of the aftershock hypocenter distribution of part A (August, 1995) and B (September, 1995). Light squares give the hypocenter solutions from NEIC and Harvard (CMT). Note the northern and southern "branch" of activity in the distributions. Viewpoint is from NE to SW onto the subducting slab. Due to this viewpoint, note that W is on the right.

shock activity. A preliminary minimum 1D P-wave velocity model of 8 layers was used for this procedure. It resulted in an adjustment of the landward network configuration by transferring stations, previously installed in the north, to the southern end of the network. Locations for the OBH were chosen according to this preliminary event distribution.

To facilitate hypocenter determination, event detection had to be provided. For this purpose all continuous data streams had to be homogenized. This was done by applying an LTA/STA trigger algorithm to the data of the landward network, followed by a coincidence check within a time interval of 35 s, which is the maximum travel time difference between two stations (*Asch et al.*, 1996). In addition, a minimum of five stations had to record the event to be selected, what resulted in more than 15000 determinable events. To reduce this amount of data to manageable size and at the same time to raise the quality of the data set, the minimum number of stations to have recorded the event was set to 15. This resulted in 4426 events (*Husen*, 1999) which constitute the final catalogue with a volume of 13 GByte. OBH, PDAS and REFTEK data had to be merged. This was done by grouping the records for each event and convert them into a common format which was the PDAS format. The final catalogue is archived on 22 CD-ROM's.

weight	P-onset uncertainty [s]	S-onset uncertainty [s]
full (0)	0.05	0.1
3/4 (1)	0.1	0.175
1/2 (2)	0.15	0.25
1/4 (3)	0.2	0.3
0 (4)	> 0.25	> 0.35

Table 2.3: Table of weights to be assigned to P- and S-wave onsets and their meaning of uncertainty.

2.5.2 *Hypocenter determination*

The software package of GIANT/PITSA was used to identify the P- and S-wave first arrivals, to determine the hypocenter locations and to calculate a local magnitude for each event. Focal mechanism solutions were given if certain quality requirements were satisfied. The actual phase picking was done in PITSA (Programmable Interactive Toolbox for Seismological Analysis, *Scherbaum et al.* (1999)) using HYPO71 (*Lee & Lahr*, 1975) for locating the earthquakes. *Rietbrock* (1996) integrated PITSA into GIANT (Graphical Interactive Aftershock Network Toolbox) which provides an environment to visualize i.e. station distributions, combined traces and fault plane solutions, all manageable under an X-windows environment.

The accuracy of a hypocenter determination relies a good deal on how well P- and S-wave first arrivals are picked. In order to achieve a precise data set, emphasis was put on the picking routine by establishing a picking convention. This involved the attribution of a weight to each picked phase, reflecting the detectebility of the phase onset expressed as an uncertainty in time. Five gradual weights were used which are listed in Table 2.3

In addition, an onset-type, impulsive or emergent, as used also in global seismology, and the direction of first motion (up or down) was attached to P-wave first arrivals of good quality. As the onset of the S-wave often interferes with the P-wave coda, onset-type and first motion direction were usually not assigned to S-wave first arrivals unless a definately undisturbed onset was apparent. To improve the detectability of the S-wave first arrivals in general, the horizontal traces of the seismograms were rotated and integrated. This 2D type of rotation around the Z-axis makes the horizontal components (NS and EW) of the station coordinate system coincide with the transvers or radial component of the source coordinate system. Consequently, to perform rotation, a pre-determined location of the event must exist. That is why the time consuming manual work of picking had to be done twice for over 1700 analysed events. Integration is equivalent to the application of a filter to subtract disturbing higher frequencies from the lower frequent S-wave signal. Very important for the accuracy of hypocenter locations is how well the used velocity model is reflecting the real velocity structures in the investigated area. As mentioned before, a first minimum 1D velocity model was constrained in the Antofagasta field headquater, based mainly on information from reflection seismic profiling (*Wigger et al.*, 1994). With this velocity model first routine determinations of earthquake locations were carried out. After a certain amount of fairly good solutions were available, *Husen* (1999) calculated a final

1D velocity model for *P*- and *S*-waves (Fig. 2.14). For this iterative inversion process he used the software of VELEST (*Kissling et al.*, 1995), incorporating i.e. station corrections and the prominent discontinuity at 15 km depth, as identified previously by *Wigger et al.* (1994) and *Patzwahl* (1998). This final 1D velocity model was used for all hypocenter determinations for the events used in this work (see i.e. Fig. 2.13 and histograms of Fig. 2.11). Absolute error estimations for the event locations were possible by using mine blasts in the area of the network. This led to an absolute accuracy of +/- 0.5 km in epicenter determination and 2.5 km in depth determination (*Husen*, 1999).

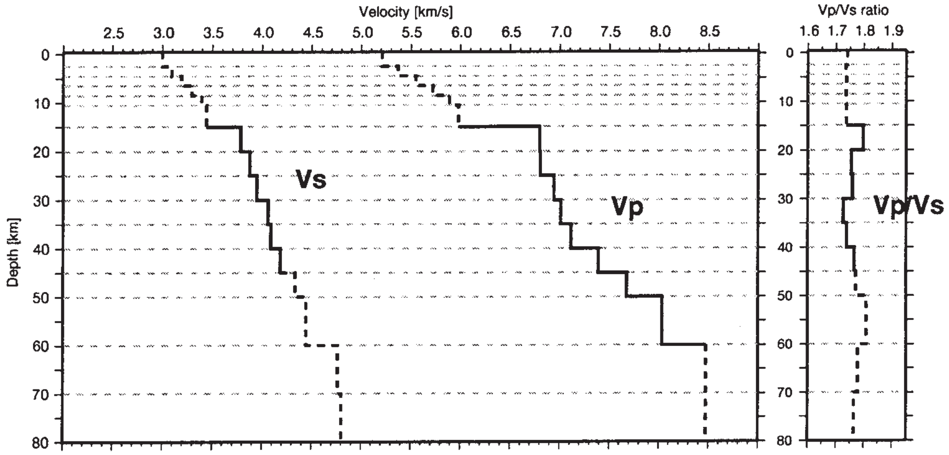

Figure 2.14: Final 1D velocity model for *P* and *S* phases from *Husen* (1999)

2.5.3 *Calculation of fault plane solutions*

The fault plane solutions of over 300 aftershocks (see also chapter 5) were calculated using the program FPFIT by *Reasenberg & Oppenheimer* (1985) based on the polarities of *P*-wave first arrivals. This program is implemented in the GIANT software, which offers an operation under X-windows environment and connects it to PITSA, where the polarities are assigned to the respective *P*-phases. Polarities are marked by a "U" for "up", and a "D" for "down" (see Fig. 2.15), describing in this way the direction of the very first *P*-wave motion in the seismogram of the Z-component. Following the geophysical convention, "up" is denoted positive and means compression at the focus. In terms of the "beach ball", compressional quadrants are shaded white. Thus "down" is denoted negative and means dilatation at the focus. Tensional quadrants are shaded dark. The ability to determine a polarity with adequate certainty implies that the seismic trace shows a good signal/noise ratio. As a matter of fact, this leads to a first selection of high quality data for the calculation of a fault plane solution.

According to the options in FPFIT, the following rules were applied to the acceptebility of a fault plane solution:

- A fine search of 1° in strike, dip and rake had to be performed to determine the best fitting fault plane solution.

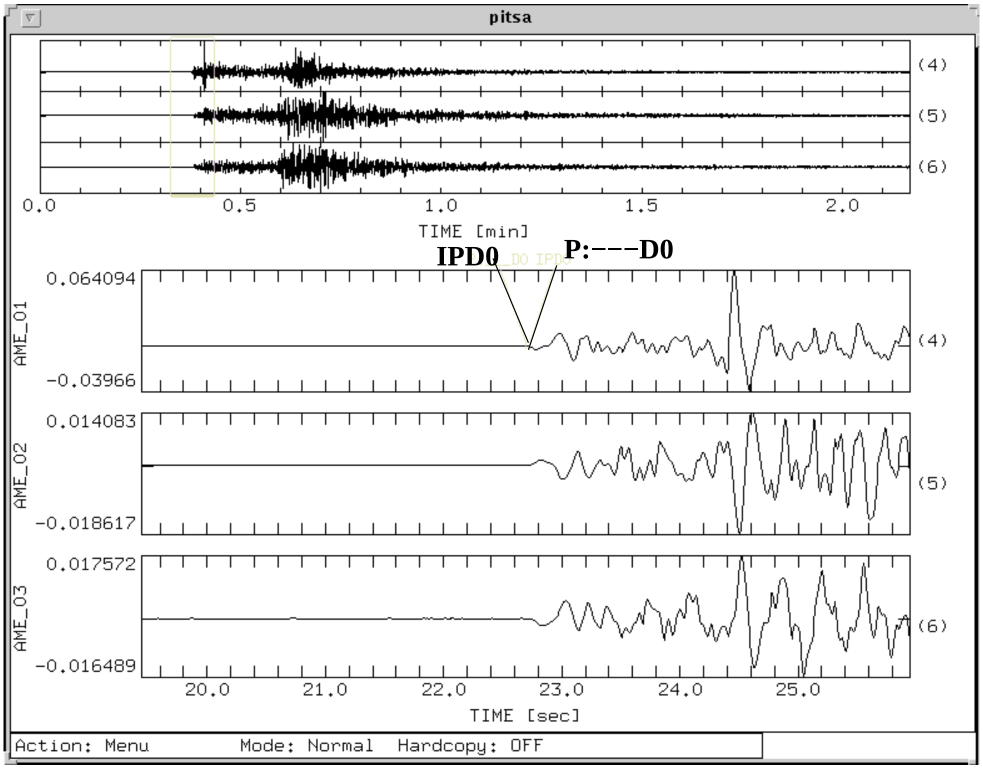

Action: Menu Mode: Normal Hardcopy: OFF

Figure 2.15: Example of the three components of the seismic wavetrain at station AME as displayed by PITSA. P:D0 denotes the "picked" (observed) *P*-wave first arrival, asigning to it a "down" polarity and full (0) weight. IPD0 denotes the calculated *P* arrival.

- No multiple solutions were accepted; only solutions with a rather stable unique result were taken for further investigations.
- Nodal planes had to be well "fixed" by stations near the denoting lines.
- The dispersion of the P- and T-axis (marked by a small p and t respectively in the resulting fault plane solutions as shown in Fig. 2.16) had to be small; solutions with largely varying P- and T-axis were not accepted. P- and T-axis are given at a 90% confidence level.

In Fig. 2.16 four calculated fault plane solutions are shown considering the above mentioned rules. The small map in Fig. 4.1 gives the geographical locations of the fault plane solutions and shows their position with respect to the network layout. The northern thrust fault example at the coastline of Mejillones Peninsula (solution A in Fig. 2.16) shows that most of the stations on the eastern compressional quadrant have the same angle of incidence. This is due to the position of the hypocenter at the western margin of the network. Such a problem arises for many fault plane solutions studied here. Nevertheless the solution can be qualified as fairly stable, as there are stations near the nodal planes which fix them (e.g. CAC, PA2 in Fig. 2.16). Dispersion of the T and P axes is small which also supports a rather stable solution. The strike slip example on Mejillones Peninsula (solution B in Fig. 2.16) displays a stable solution satisfying all quality criteria, although this is an event with a small magnitude of M_L=1.58. Solutions C (thrust) and D (dip slip) in Fig. 2.16 are also good examples for fairly stable solutions despite of their GAPs larger than 180°.

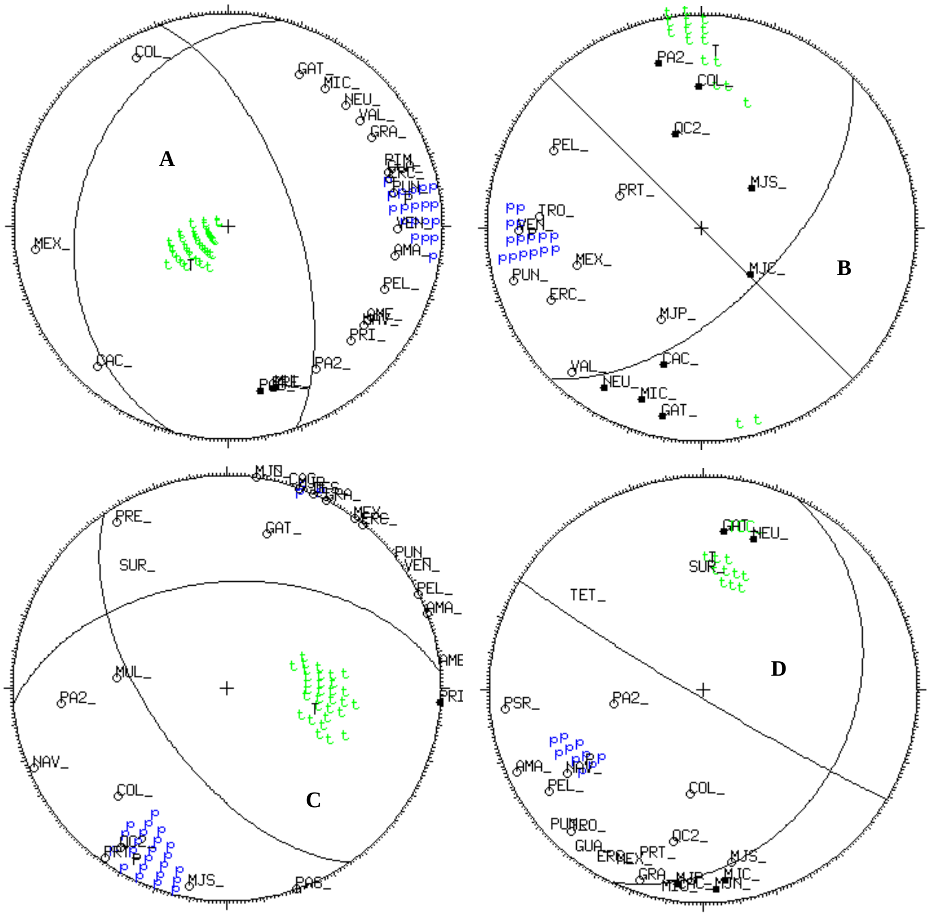

Figure 2.16: Four examples of calculated fault plane solutions. They have been accepted for further investigations according to the quality criteria as explained in the text. Small p's (blue) and t's (green) denote the possible P- and T-axis locations, based on a 90% confidence level. Black dots mark positive polarities and thus give the tensional quadrant in the fault plane solution. Unfilled dots mark negative polarities and compressional quadrants respectively. Station names are given by three letter code.

FPFIT includes estimations for parameter uncertainties and solution quality which is based on a letter code a), b), c) and d). The definition of the classes a) to d) is according to the variations of the solution in strike, dip and rake. Thus the strike, dip and rake of class a) solutions vary between 0 and 20°, b) between 20° and 40° c) more than 40°. Unfortunately this information is not stored in the GIANT database and thus gets lost after a new fault plane solution is calculated.

The variations in strike, dip and rake are the result of a misfit score, limited by the 90% confidence interval of a one-norm misfit function which assignes higher weights to stations more distant to the nodal planes and lower weights to stations near the nodal planes. This

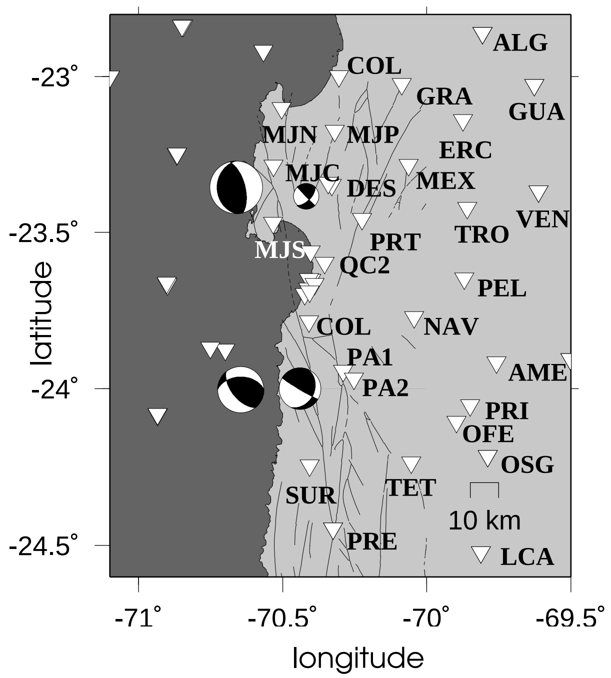

Figure 2.17: Locations of the four fault plane solutions in Fig. 2.16. White triangles give station locations with three letter codes to identify the stations used for calculation.

weighting is based on the theoretical P-wave radiation amplitudes and accounts for the fact, that first arrival amplitudes are much smaller near the nodal planes of a fault plane solution. Combined with a bad signal to noise ratio it makes sense to give more weight to larger amplitudes of stations further away from the nodal planes. This does not apply very well to the presented data, as 1) only good signal to noise ratio data is used for the calculation of fault planes, and 2) the quality of a fault plane solution depends also on stations located near the nodal planes to "fix" them.

We believe that the fault plane solutions presented here have variations in strike, dip and rake of no more than +/- 10°. Nevertheless, the discrepancy of the minimum 1D velocity model and a particular velocity structure at different sites and the specific geometry of a subduction zone environment will have influence on the stability of a fault plane solution.

2.5.4 *Determination of magnitudes*

For each investigated event of the aftershock sequence a local magnitude M_L is calculated, based on the definition by *Richter* (1958):

$$M_L = logA - logA_0 \tag{2.1}$$

where logA is the logarithm of the 0 to peak amplitude. The function $-logA_0$ is a correction term to account for the different epicentral distances Δ, and is scaled for an earthquake of M_L=3 at R=100 km to have a zero to peak amplitude of 1 mm measured on a Wood-Anderson seismograph (*Richter*, 1958; *Bakun & Joyner*, 1984).

Bakun & Joyner (1984) parameterized the $-logA_0$ function from Richter's relation, taking the amplitude A out of synthetic Wood-Anderson seismograms from CALNET (Central California Network) horizontal component data. They applied the relation

$$M_L = logA + [nlog(R/100) + K(R - 100) + 3] \tag{2.2}$$

where n is the geometrical spreading factor (taken here as n=1), R is the hypocentral distance and K is the attenuation coefficient defined as

$$K = \frac{\pi f ln10}{Q v_s} \tag{2.3}$$

with Q as the quality factor in the region covered by the hypocentral distances, v_s=3.5 km/s as shear wave velocity, and f as frequency. This formula of *Bakun & Joyner* (1984) is implemented in the GIANT software for M_L calculation, including the parameter values adopted for California which leads to K = 0.00301 +/- 0.00036 km^{-1} for n=1. When identifying *P* and *S*-wave arrivals in the seismograms in PITSA, the peak to peak value of the largest *S*-wave amplitude on one of the horizontal components is "picked" for each station (see example in Fig. 2.18). From each amplitude a magnitude is calculated according to Eq. 2.2. Then all magnitudes for one event are listed and a mean magnitude value is derived by summing up all station magnitudes dividing through number of participating stations.

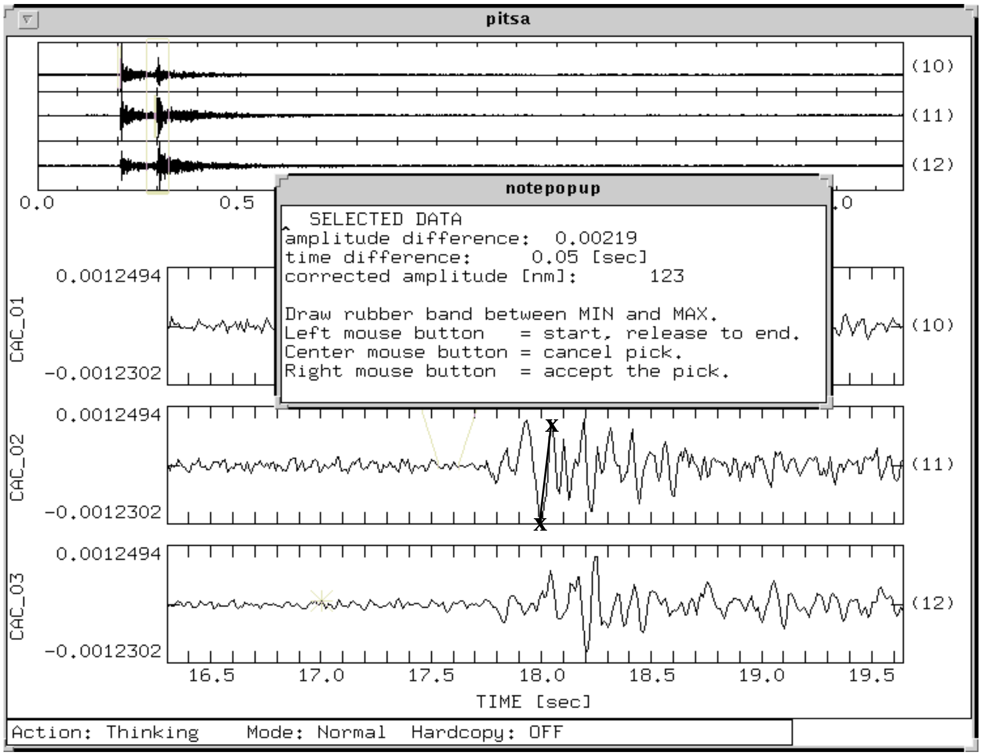

```
 SELECTED DATA
amplitude difference:  0.00219
time difference:     0.05 [sec]
corrected amplitude [nm]:      123

Draw rubber band between MIN and MAX.
Left mouse button   = start, release to end.
Center mouse button = cancel pick.
Right mouse button  = accept the pick.
```

```
Action: Thinking    Mode: Normal   Hardcopy: OFF
```

Figure 2.18: Example for determining the largest apparent *S*-wave amplitude on the horizontal components to calculate the magnitude of an event at a particular station.

The calculated local magnitudes for the used data base as shown in the previous sections, range from 0.8 to 5.1, where only three events occur with magnitude 0.8 and only one magnitude of 5.1 in the second part of the data base (see also Fig. 2.11). The mean magnitude of sub-sequence A is 2.1 and for sub-sequence B it is 2.0. According to the epicentral and hypocentral distances occurring in the data set (Fig. 2.19 a) and b)), the M_L magnitude seems to be appropriate for the CINCA'95 network, as the distances range from $0 < \Delta < 370$ km when considering only the earthquakes within the seismogenic zone. Nevertheless, the relation for M_L after *Bakun & Joyner* (1984), and especially its parameter K, are adapted to crustal conditions in California, and therefore the use of this relation needs some verification in case of the northern Chile data.

When plotting the individual station magnitude values for one event, the distribution deviates to some extent from a Gaussian type distribution. The histograms rather show discrete peaks which may be interpreted in terms of a distinct heterogeneous structure in the upper crust influencing the wave attenuation. Fig. 2.20 shows three examples of events with different magnitudes and depths.

For some events, an increase in magnitude with increasing hypocentral distance R could be observed (see Fig. 2.20 c)). As crustal conditions in the North Chilean subduction environment should be different from crustal conditions in California, the first idea was to vary the quality factor Q and to substitute $Q = 680$, as used in the formula of *Bakun & Joyner* (1984), by higher Q-values. These attempts were not successful, although tests with Q-values up to 8000 and a v_s velocity of 4.0 km/s were used to account for the plutonic structure and the proposed high Q-values for the coastal region (*Haberland & Rietbrock*, 2001). In a next step the radiation pattern of the aftershock focal mechanisms

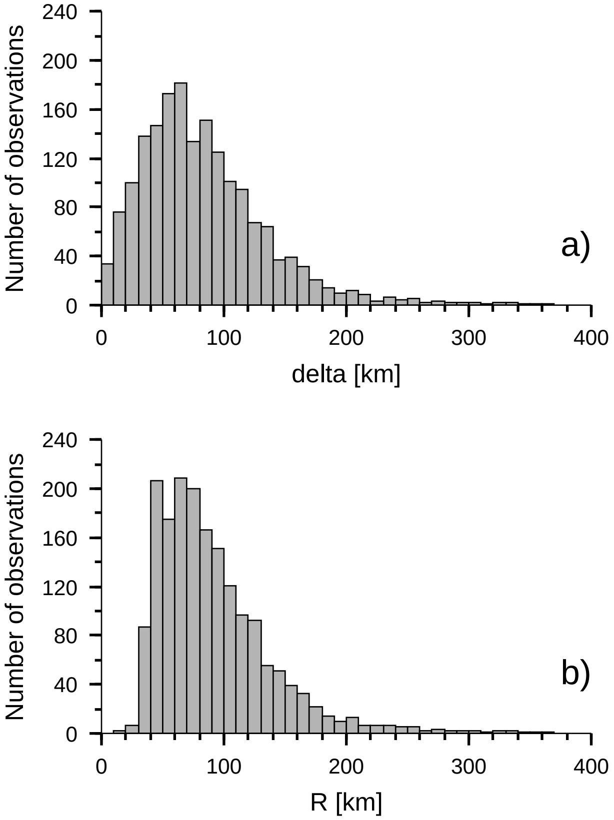

Figure 2.19: Distribution of a) epicentral distances and b) respective hypocentral distances for events occuring in the seismogenic zone.

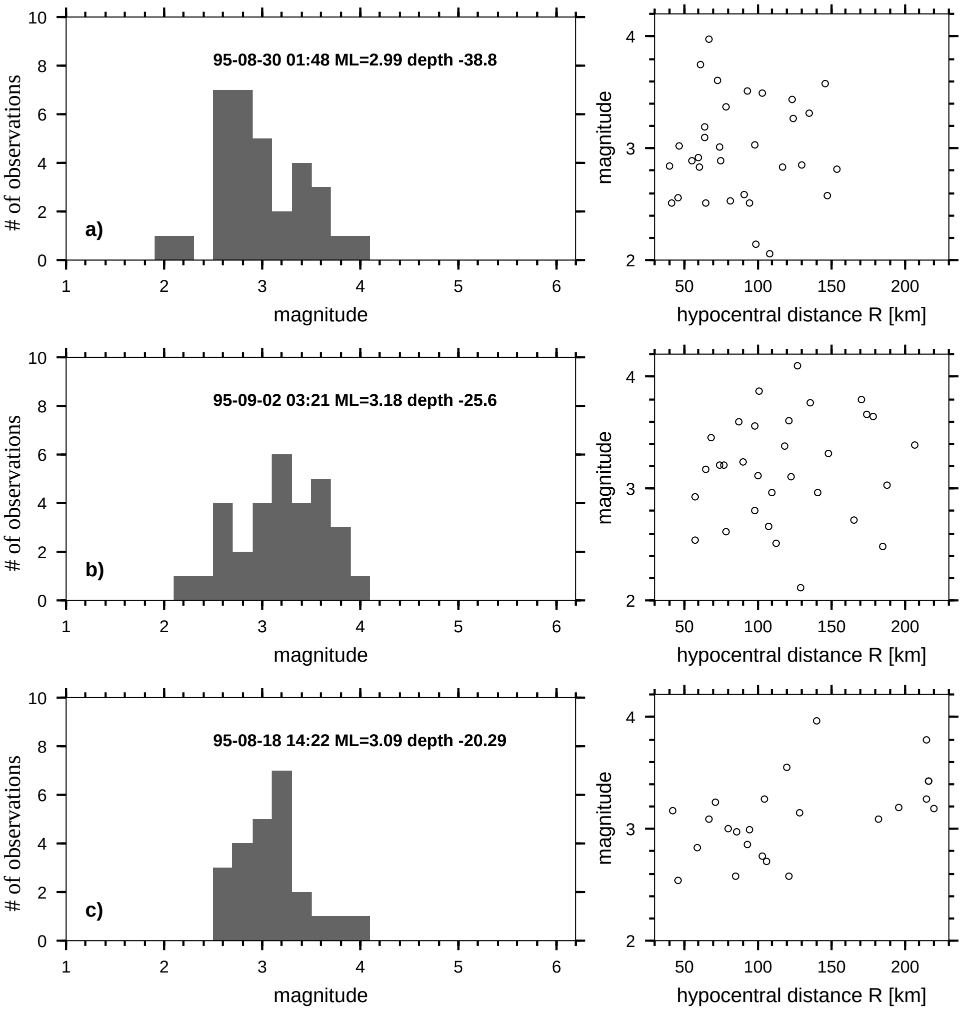

Figure 2.20: Magnitude histograms and magnitude distribution with hypocentral distance R for three (a), b), and c)) events with different M_L and depth ranges.

in combination with the subducting slab geometry were examined. In this procedure the picked zero-to-peak amplitudes were corrected with the calculated horizontal component S-wave amplitudes from the radiation pattern of a specified event. This reduced the effect of magnitude increase with distance considerably and led to the assumption that for the events considered, focal mechanism characteristics dominate over attenuation features. The events observed with the described magnitude increase are of thrust mechanism and reside more in the very shallow part of the subduction zone nearer to the trench. As only a few events with this characteristics were noted, the formula by *Bakun & Joyner* (1984) was applied without doing further corrections to the magnitudes. The correction term $-logA_0$ calculated with the presented data according to *Bakun & Joyner* (1984) is shown in Fig. 2.21 in comparison to Richters (1958) original attenuation curve.

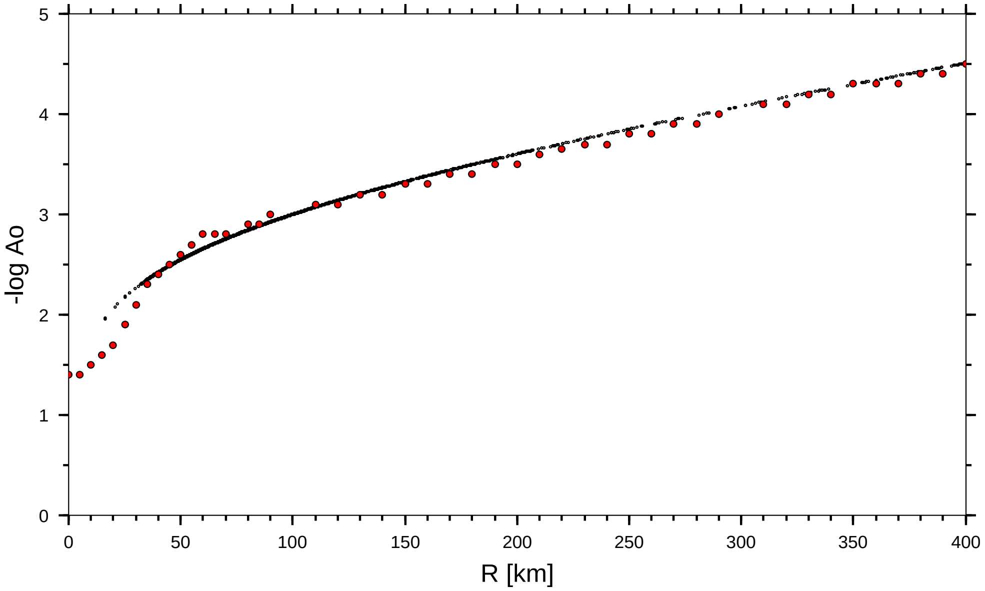

Figure 2.21: Distance dependent attenuation curves, $-logA_0$. Small black dots show the data used here calculated according to the relation of *Bakun & Joyner* (1984) for California. Red dots give the attenuation curve derived by *Richter* (1958).

3. *b*-value Mapping of the Fault Plane Area

Assuming that the seismic *b*-value is spatially varying in a significant way, it was chosen to persue the idea of mapping structural inhomogeneities on the main shock fault plane of the 1995 Antofagasta earthquake. The resulting map is compared to other geophysical parameters such as the moment release, isostatic residual field and the distribution of seismic energy to varify the physics behind the observed variations. The chapter starts with the general definition of the Gutenberg-Richter (GR) relation. With regard to the ongoing discussion whether *b* value variations in space and time are physically significant or whether the occurrence of earthquakes is a self organized critical process, the two approaches are described in one section.

3.1 The magnitude - frequency relationship of earthquake occurrence

3.1.1 *General definition*

The magnitude-frequency relationship, as established by *Gutenberg & Richter* (1944), was determined to improve the estimation of the frequency of destructive earthquakes in California by means of a statistical method rather than rely on historical records only. Their original formula $logN = a + b(8 - M)$ relates the frequency of earthquakes to the magnitude using the local magnitude M_L as a magnitude scale. The more general non-cumulative form of the Gutenberg-Richter relation is written as

$$log(N(M)) = a - bM \tag{3.1}$$

where N is the number of events with magnitudes $M \pm \Delta M$, a describes the level of seismic activity and b is the slope of the frequency curve (see Fig. 3.1). *Ishimoto & Iida* (1939) had defined earlier a similar relationship using the the maximum trace amplitude of an earthquake instead of the magnitude. To derive the cumulative form of Eq. 3.1, which is more appropriate to determine the number of events above a certain magnitude threshold, Eq. 3.1 can be written as (*Scherbaum, 1999, written comm.*)

$$N(M \pm \Delta M) = 10^{a-bM} = 10^{a} \cdot 10^{-bM} = \alpha \cdot e^{-\beta M} \tag{3.2}$$

where $\alpha = 10^a$ and $\beta = ln10 \cdot b$. This shows, that the magnitudes follow a power law distribution in the non-cumulative relation. The number of events $N(M_+)$ for which the magnitudes are $\geq M$, a certain magnitude threshold, is defined as

$$\begin{aligned} N(M_+) &= \alpha \int_M^\infty e^{-\beta m} dm = \frac{\alpha}{-\beta} \cdot e^{-\beta m}|_M^\infty \\ &= \frac{\alpha}{\beta} \cdot e^{-\beta M} \quad = \alpha_+ e^{-\beta M}. \end{aligned} \tag{3.3}$$

This means that in the cumulative relation the magnitude distribution also follows a power law. Eq. 3.3 can be changed into

$$N(M_+) = 10^{a_+ - bM} \quad or \quad log(N(M_+)) = a_+ - bM. \tag{3.4}$$

Fig. 3.1 shows the non-cumulative and the cumulative form of the magnitude-frequency relation as determined for the aftershock sequence and the data set used for the *b*-value mapping. The data set represented in this figure is the one described in detail in the previous chapter, which is the joint time series of sub-sequences A and B shown in Fig. 2.11.

The constant *b* in the magnitude-frequency relation is determined by the slope of the graph. A steep slope corresponds to a high *b*-value, when the slope flattens, the *b*-value is getting lower. Thus *b* reflects the relation between number of events with high magnitudes to the number of events with low magnitudes in a given volume or earthquake population.

Changes in time and space of this relation are observed, obviously correlated to changes in conditions of the environment in which the earthquake population is located. This will be addressed in the following section 3.1.2. On the other hand many attempts have been made, to describe the occurrence of earthquakes as a self organized critical phenomenon (SOC), which implies a constant *b*-value over all magnitude ranges. The SOC approach will be discussed then in section 3.1.4.

3.1.2 *Spatial variability of the b-value*

Gutenberg & Richter (1944) mainly focused on the use of the magnitude-frequency relationship (MFR) to find the number of large earthquakes to be expected in a certain time span. At first, a spatially varying *b*-value was not considered. The slope of the MFR was rather suggested to be constant and *b* to have a value around 1. Deviations of the MFR from a constant value were attributed to limitations in seismic monitoring at that time when smaller magnitude events hardly could be registered in a complete manner for larger areas, neither in California nor in any other region worldwide. However, complete data sets spanning over a large magnitude range are required to investigate spatially changing *b*-values. Therefore spatial and temporal *b*-value variations were first reported from laboratory experiments where controlled conditions guarenteed data sets with a sufficient

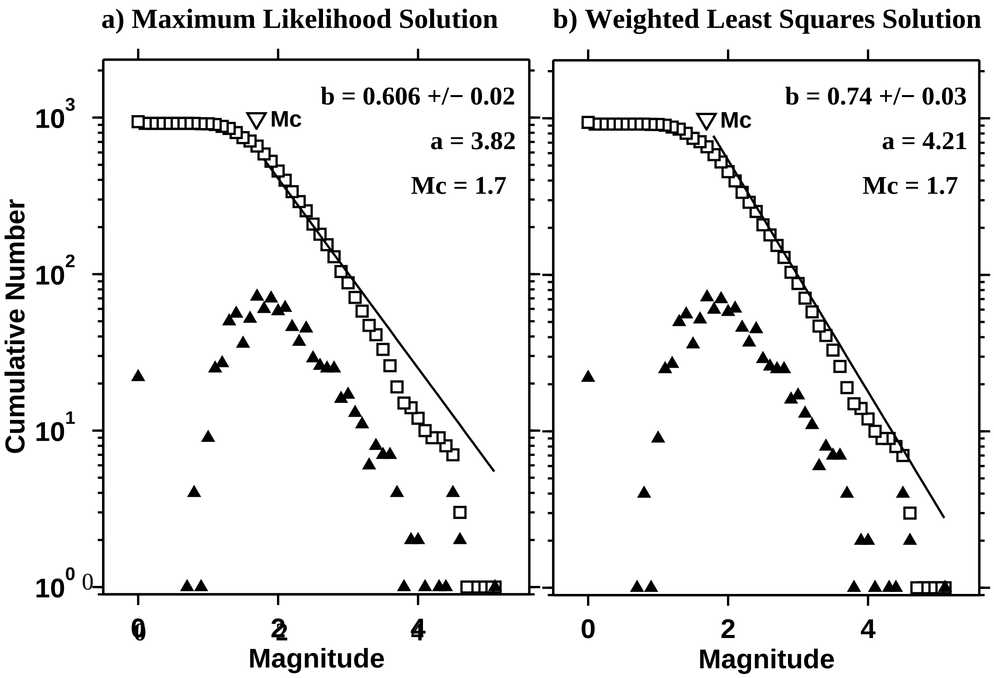

Figure 3.1: The cumultive and non-cumulative form of the Gutenberg-Richter relation for the data of the Antofagasta aftershock sequence used for the *b*-value mapping. Two statistical methods are applied: a) the maximum likelihood estimate and b) the weighted leasts squares method. The respective parameters *b*, *a*, and M_c are given in the figures.

number of events. Most of the knowledge about the physical relations between the *b*-value and parameters like stress or structural properties of materials thus comes from observations in the microscopic environment. However, they give first important insights into this relations and will be reviewed briefly in the following:

Two important contributions in this sense are the laboratory studies by *Scholz* (1968) and *Mogi* (1962). They investigated the dependence of the *b*-value on material heterogeneity, crack density, rock type, local stress distributions and confining pressure. *Mogi* (1962) describes the frequency-magnitude distribution for elastic shocks accompanying brittle fractures in heterogeneous material and finds that the MFR depends on both, the structural state of the material and on the spatial variation of the stress. From experimenting with artificial material samples he observed that *b* increases with the degree of heterogeneity, with increasing crack density, and with an increasing degree of spatial variations in stress distribution. It was possible to correlate certain ranges for *b*-values with specific material properties which are listed in Tabel 3.1.

Scholz (1968) corroborated these findings to some extent but emphasizes that the dominant dependence of *b* is on stress rather than on physical properties of the material. In uniaxial and triaxial compression experiments the *b*-value in the different investigated rock types showed a clear decrease with increasing stress (Fig. 3.2).

High *b*-values are found in the range of 0 to 30% of fracture stress whereas above 60% of fracture stress the *b*-value is permanently decreasing. The high *b*-value area is interpreted by the dominance of small events, as sliding takes place on pre-existing cracks. The *b*-values

type of material	b-value range
clastic or very porous material	2.0 - 2.7
heterogeneous but compact material	1.0 - 2.0
homogeneous material under uniform stress	0.3 - 1.0

Table 3.1: Characteristic b-values for different materials as derived from laboratory experiments by *Mogi* (1962)

above 60% of the fracture stress indicate that events become statistically larger as stress increases. According to Scholz's experiments the curves describing this dependence of b on the applied stress for a variety of rocks are all showing similarity although they are shifted in absolute values of b. A somewhat different result was gained from the examination of a marble. The MFR of this type of rock was characterized by high b-values throughout the experiment which supports the results by *Mogi* (1962). The major conclusions drawn by Scholz can be summerized as follows:

- The MFR of microfracturing events is a well defined property of brittle rocks with distinct characteristics.
- b depends strongly on the state of stress and only to a lesser extent on the physical properties of the rock.
- The MFR distinguishes between these two processes: At low stress, where crack opening, closing and sliding are important, high b-values are found. Above 50% of the fracture stress, new fractures are propagating, b is lower and in the range usually observed for earthquakes decreases as stress increases.

Another important observation, concerning temporal variations in b, is the precursory b-value anomaly before failure in a rock sample (*Main et al.*, 1989). The authors present a model which can explain qualitatively the major temporal fluctuations in b according to the applied stress and crack growth under constant strain rate. The observed behavior of stress σ, crack length X, the stress intensity factor K and the b-value can be seen in Fig. 3.3 for elastic failure (curve 1) and anelastic failure (curve 2). They quantified the decrease of b just before failure to a critical value of b_c=0.5. This pronounced decrease in b is positively correlated to a peaked decrease in accoustic emission rate immediately before the main event. Although on a different time scale, such temporal variations in b were also present in back ground seismicity several years before earthquakes with M>6 in New Zealand, which had a strong dip slip component (*Smith*, 1986). In this case the author observed volumes with anomalously high b-values for up to six years before a main shock located in the vicinity of the high b volume.

However, direct transfer of perceptions determined in laboratory experiments to macroscopic environments always inheres a number of problems. Therefore, in the following

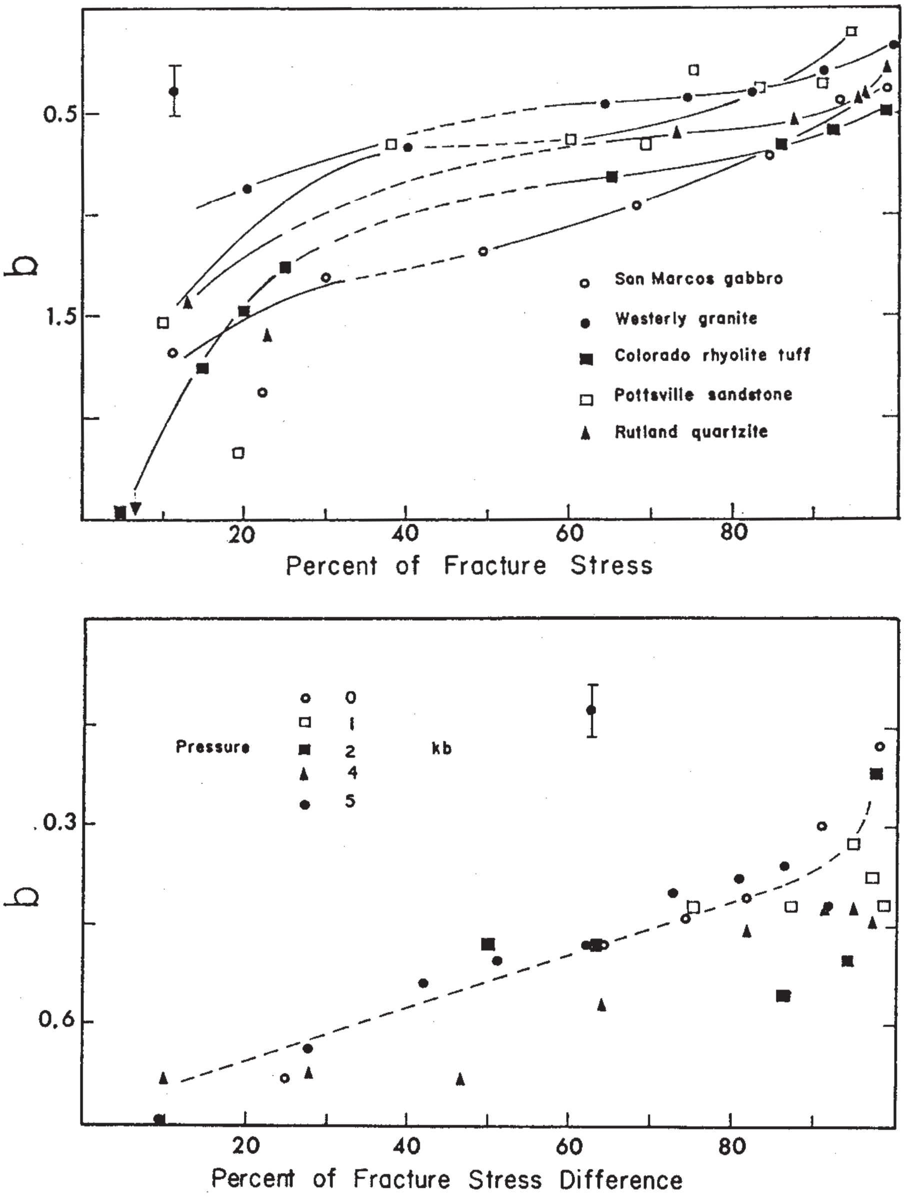

Figure 3.2: Uniaxial (upper) and triaxial (lower) laboratory experiments to show the dependence of b on stress. See text for further explications. From *Scholz* (1968).

several attempts will be reviewed where authors have varified the validity of microscopic b-value behaviour in macroscopic environment. For instance the strong dependence of b on stress is confirmed for earthquakes in a study by *Wyss* (1973) on fluid pressure induced events. He found that low b-values are an indicator for high stress in the source region. It was also found that higher stresses might explain the relatively low b-values of foreshocks (*von Seggern*, 1980) and the decrease of b-values in the crust with focal depth (*Mori & Abercrombie*, 1997; *Wiemer & Wyss*, 2000).

Recent results on the investigation of the brittle-ductile transition in rocks and associated seismicity (*Amitrano*, 2003) suggest that the b-value might be controlled by the

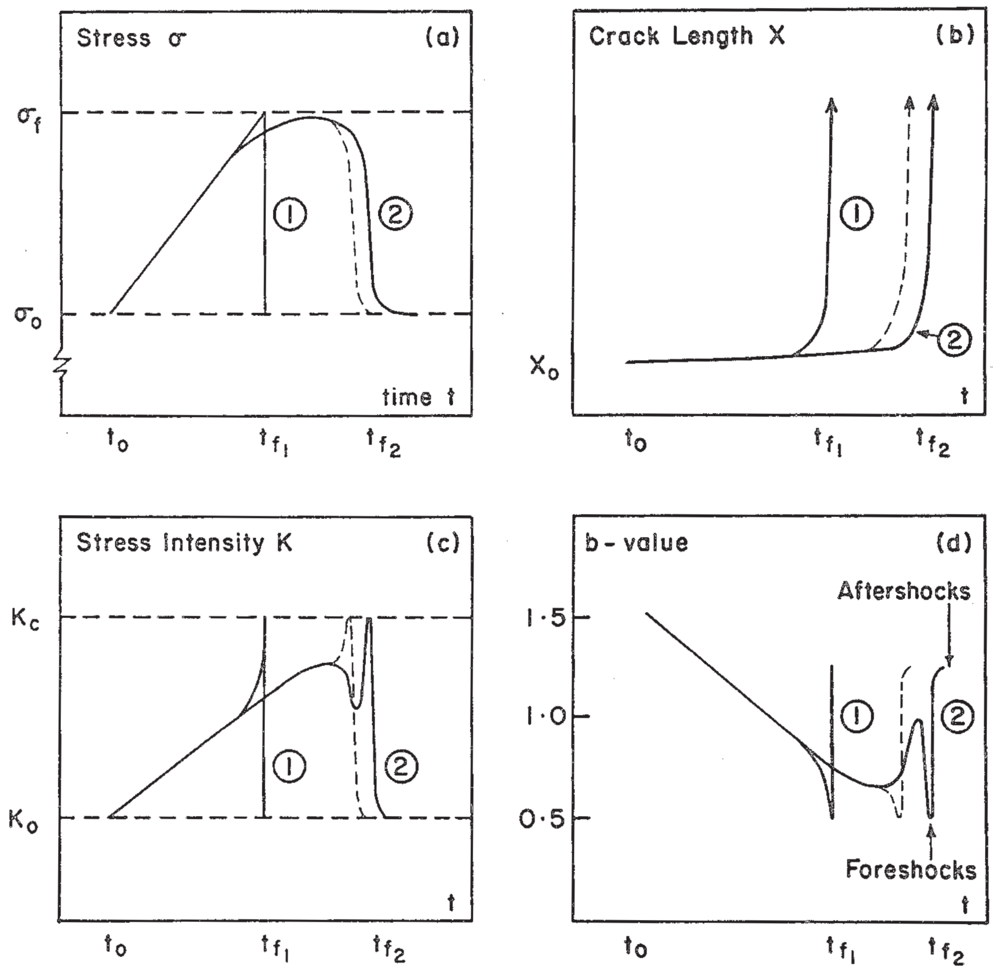

Figure 3.3: Behaviour of stress σ, crack length X, the stress intensity factor K, and the b-value during elastic (curve 1) and anelastic (curve 2) failure due to laboratory experiments. The b-value decreases to a critical value of 0.5 short before failure occurs. From *Main et al.* (1989).

variations of the internal friction angle induced through changes in confining pressure. The internal friction angle influences the degree of anisotropy in an area as low friction leads to quasi-isotropic states of the material and high friction to highly anisotropic states. At a macroscopic scale this leads to a "damage" distribution or degree of heterogeneity which varies from diffuse to localized depending on the internal friction angle. These results were used to explain successfully the mechanical behavior of geological structures in the Alps by doing a statistical anlysis of the related seismicity (*Sue et al.*, 2002).

Two further publications should be mentioned here as they are important in establishing a link between micro- and macro-scale observations: Jin's and Aki's investigations on coda Q^{-1} and the b-value in California (*Jin & Aki*, 1989) and Urbancic's obseravtion of space-time variations of b during rock bursts in a mine (*Urbancic et al.*, 1992). *Jin & Aki* (1989) found a convincing positive correlation with a correlation coefficient of 0.79 between coda

Q^{-1} and the the b-value for seismicity in California within a time window of 55 years in the vicinity of the station Riverside. By cross-correlating the two parameters the best correlation was determined at zero delay time between them, which suggests a common cause affecting both parameters simultaneously. As a first conclusion crack density in the lithosphere was proposed to be the influencing parameter. But doing a thorough review of similar investigations, Jin and Aki found that Q^{-1} and b can also correlate negatively, which was reported from other case studies of seismic active regions. *Jin & Aki* (1989) suggested a creep model to account for this more complex behaviour based on the fact that creep can correlate either positive or negative with seismicity depending on the spatial scale and earthquake magnitude. The concept includes the introduction of a magnitude threshold above which the b-value representing the seismicity and Q^{-1} as a measure for crack density correlate positively and below which the correlation is negative.

The rockburst in a mine and its related micro-seismicity (-2>M>0.5) before and after the main shock was used by *Urbancic et al.* (1992) to investigate temporal and spatial changes in the b-value. They found that decreasing b-values correlate with increasing stress release estimates and that larger events tend to occur where the b-value has its steepest gradient. Interestingly in this case the magnitude-frequency distribution had a non-similar character for the complete magnitude range but showed self-similar behaviour in the range between -1.1 and -0.4. Accounting for this magnitude range, the authors hypothesize that low magnitude b-value is a good indicator for the stress state within the rock mass. They further concluded that b-values ”provide the best estimates for stress conditions within the seismogenic volume as they include information from both spectral- (seismic moment) and time domains (peak amplitudes)” (*Urbancic et al.*, 1992).

Summerizing the previously described observations from laboratory experiments and investigations of seismicity, the two main conclusions that appear to be important for the physical meaning of the b-value variations and which will be taken as a basis for the interpretation of the presented b-value map are

- b is strongly dependent on stress, in such a way that b decreases with increasing stress
- b depends secondarily on the heterogeneity of the material concerned, in a way that b increases with increasing heterogeneity.

With the improvement of seismological networks, high quality data sets incorporating all magnitude ranges got available. The catalogues with densely distributed seismic events facilitated the use of mapping techniques to calculate spatial distributions of the b-value which all showed major and minor variations of b in space and time. The previously summerized observations about physical relations were used to interpret these mapped differences in b. Meanwhile a number of b-value mappings in different tectonic environments like volcanic areas (*Wyss et al.*, 1997; *Wiemer & McNutt*, 1997), subduction zones (*Wiemer & Benoit*, 1996; *Sobiesiak*, 2000), tanscurrent fault systems (*Wiemer & Wyss*, 1994, 1997; *Baumbach et al.*, 2004) confirm statistically significant variations of the parameter in the range of $\sim$ 0.4 to 2.0. Aftershock sequences have proofed to be suitable for this type of studies as a large number of earthquakes occur in a relatively short time (*Wiemer & Katsumata*, 1999). But recently also background seismicity of entire regions has been studied successfully by b-value mappings (*Bhattacharya et al.*, 2002; *Sue et al.*, 2002). A mapping technique is also applied to the Antofagasta aftershock sequence which will be described in section 3.2

3.1.3 *Causes for "kinks" in the MFR*

The previously reviewed space and time variations observed in b result in a non-linear slope of the MFR and consequently in different b-values for a population of N earthquakes in a considered area and magnitude range. Deviation from self-similarity of the frequency-magnitude distribution was observed for instance by *Aki* (1987) for earthquakes with $M < 3$ recorded with a borehole seismograph station in the Newport-Inglewood fault in California. Such a deviation from self-similarity has been reported also for seismic moment M_o scaling with rupture length. This break in self-similarity which seperates small from large earthquakes is found around M_o=1.0x10^{26} dyne·cm (*Shimazaki*, 1986; *Pacheco et al.*, 1992). Similarly for the b-value, *Pacheco et al.* (1992) assume that a break in the GR relation separates events with a rupture dimension equal to the width of the seismogenic zone from those which have smaller dimensions. Consequently, the tectonic setting effects the MFR and can produce likewise a "kink" in the distribution. Here a further cause for variable b-values will be discussed: seismogenic processes obviously have an influence on the MFR of earthquakes participating in this processes as observed in the aftershock data set of the M_w=6.9 Cariaco earthquake in north eastern Venezuela in July 1997. The aftershock b-value map of this strike slip event which ruptured a part of the El Pilar fault in a major transcurrent fault system, is shown in the last figure of this thesis. As some uncertainty exists about the actual extent of the fault plane, we were looking for hints on this subject in the b-value map. A sharp limit between intermediate and low b-values can be seen west of the high b area beneath Cariaco. This limit was suggested to be the western end of the fault plane (*Baumbach et al.*, 2004). The eastern end at first was defined as to the east of the last earthquake cluster, which would be at the hight of the village El Pilar. For more clearity, the epicentral distribution of the aftershocks is shown in Fig. 3.4 again

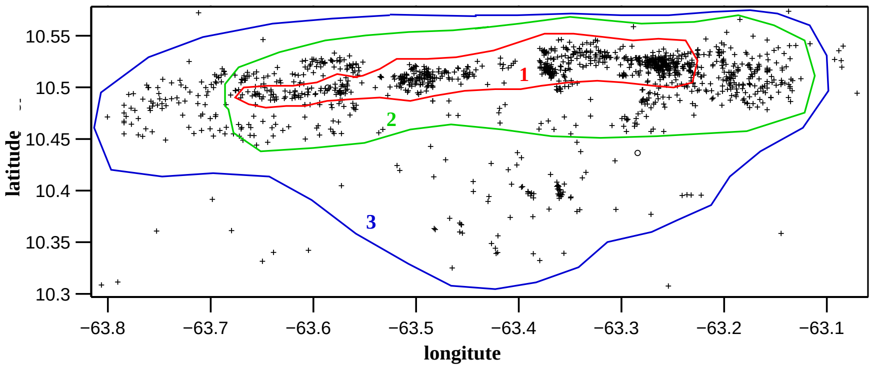

Figure 3.4: Epicentral distribution of the Cariaco aftershock sequence. Colored limits mark the sub-sequences studied for their power law behaviour. See Fig. 3.5.

Now an individual MFR was calculated for different sub-sequences 1, 2, 3 (marked with different colors in Fig. 3.4 and 4, where 4 is the entire data set with events also outside the map viewed in Fig. 3.4 Using the earthquakes of the inner fault strand (1), the respective MFR in Fig. 3.5 shows a "perturbation" at the higher magnitude end towards lower *b*-values. This perturbation persists but is less pronounced in the MFR for sub-sequence (2), encompassing events on sub-parallel fault strands. The best power law fit is achieved with the sub-sequence of (3), comprising the event clusters at both ends of the fault plane and the southern cluster, off the fault. Using the entire data set (4) is provoking a "kink" in the MFR again. Thus the events of sub-sequence (3) presumably do reflect the "real" aftershocks; events which might have a common source in the local stress field.

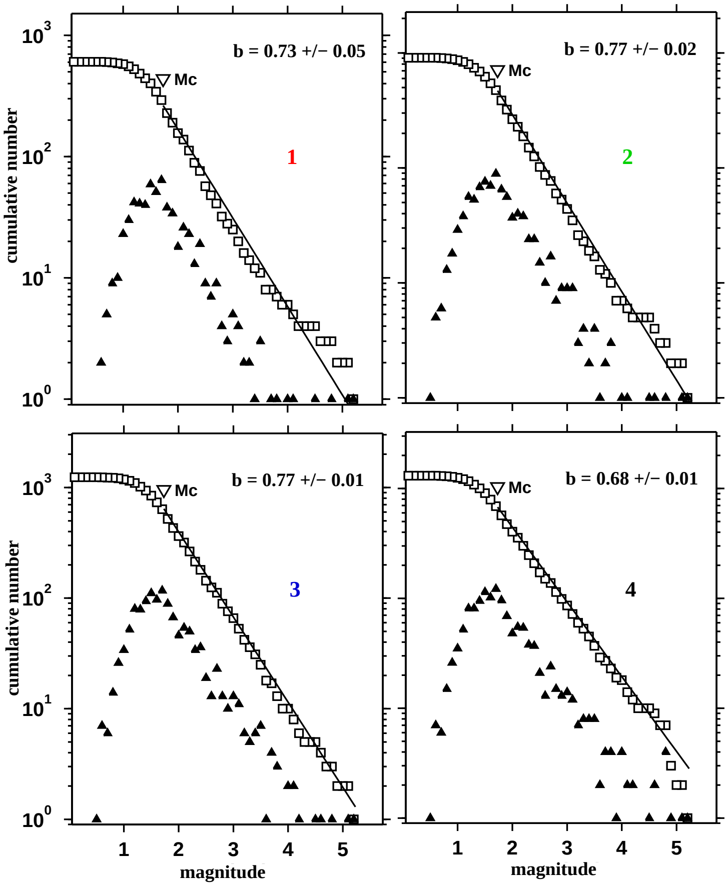

Figure 3.5: Cumulative and non-cumulative frequency-size distributions for four sub-sequences of the Cariacao aftershock data set as marked in the epicentral distribution of events in Fig. 3.4

This observation on the Cariaco data set is less clear for the Antofagasta data set. Excluding the northernmost aftershocks from the data set results in a less pronounced "kink" in the MFR but the quality of the MFR in Fig. 3.15(3) cannot be reached. However, it can be noted that either the more precisely the selected earthquake population participating in the MFR represents the definately ruptured fault plane itself, or the selected events represent the population under similar stress conditions, the more the frequency-size distribution approaches a power law. This would mean that 1) the b-value map of an aftershock sequence can help to constrain the actual extent of the ruptured part of the fault and 2) the frequency size distribution is related to a seismotectonic process. This seismotectonic process might be defined by a local stress field which determines exactly the ruptured fault plane. The aftershocks precisely in this part show another behaviour as the aftershocks outside of this zone belonging to areas of transient stresses.

3.1.4 *The GR-relation and the process of self-organized criticality*

The spatial b-value variations discussed in the previous sections are found on very local scales either in laboratory studies or specific geographical areas. This implies that the GR-relation comprising earthquake populations on such local scales is not self-similar. On local scales the GR-relation rather reflects small scale processes and conditions in the area concerned. At a first glance, this is a contradiction to the model of self-organized criticality (SOC) which a number of authors applied to explain general features on the occurrence of earthquakes (*Bak & Tang*, 1989; *Ito & Matsuzaki*, 1990; *Turcotte*, 1997).

In self-organized complex systems macroscopic structures evolve spontaneously, forming spatio-temporal patterns. These systems have to be dissipative and have to have an infinite amount of degrees of freedom (*Bak & Tang*, 1989; *Hainzl*, 1998). Criticality of such a system is given if it is developing towards a critical state at which the contineous phase transitions follow power law spatial and temporal correlation functions (*Bak & Tang*, 1989). Scale invariant behaviour is observed if self-organized critical systems are near a critical point which is defined as the phase transition between ordered and disordered states of equilibrium (*Main*, 1996; *Hainzl*, 1998). It means that the macroscopic structures of the system have no characteristic length and show the same appearance at all magnifications. Isotropic scale invariance is called self-similarity, meaning that the structures appear similar in all directions and at all scales (*Main*, 1996).

So provide that the seismogenic process is a self-organized critical phenomenon, the GR power law defines the critical state of the system and the size distribution of the earthquakes is related to geometric self-similarity. The assumptions to be made are that the system is large and that tectonic plate motion as a driving force, feeding energy to the system, is slow (*Bak & Tang*, 1989).

Simple SOC models are able to reproduce the GR-relation with a b-value of approximately 1 for large catalogues with several thousand earthquakes such as the catalogue for i.e. Armenia or Northern California (see Fig. 3.6. The deviation from the the GR-law at higher magnitudes has been explained by statistical fluctuations (*Hainzl*, 1998) or finite size effects as they cannot become lager than the brittle seismogenic zone (*Pacheco et al.*, 1992; *McCloskey*, 1983).

However, simple SOC models fail to reproduce more realistic characteristics of spatio-temporal seismicity patterns like intervals of reduced seismic activity before a large earthquake (quiescence), fore- and aftershock sequences. *Hainzl et al.* (1999) and *Hainzl et al.* (2000) introduced a homogeneous spring-block slider model similar to the Burridge-Knopoff model (*Burridge & Knopoff*, 1967) but implementing additional elements with a dashpot and a parallel spring to account for transient creep on a fault. Artificial cat-

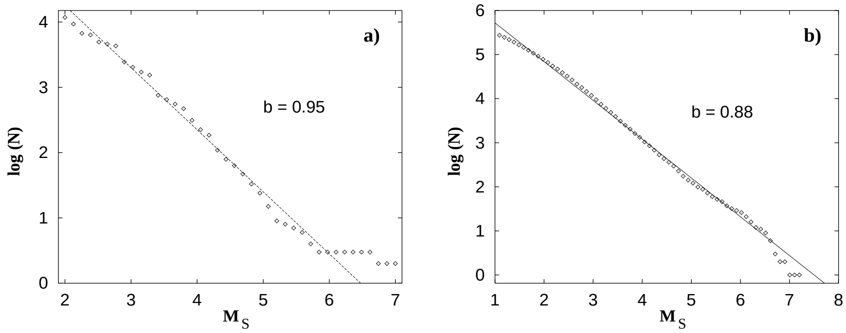

Figure 3.6: The magnitude-frequency distribution of earthquakes of a) the Armenian catalogue (Armenienkatalog 1996), and b) the catalogue of Northern California (NCSN-catalog 1998). Note the different types of deviation from the GR-relation (straight lines) at higher magnitudes. From: *Hainzl* (1998).

alogues produced by this model clearly exibit phases of quiescence, reproduce fore- and aftershock activity and show smaller b-values for foreshocks than for aftershocks, which is also observed in natural seismicity (*Wyss & Habermann*, 1988).

Also to account for the aftershock phenomenon, an interesting approach was made by *Christensen et al.* (2002) to verify a unified scaling law for earthquakes, connecting the GR-relation, the Omori law for aftershock decay, and the assumption that fault systems and the spatial distribution of earthquakes are fractal. Using the Southern California catalogue from 1984 to 2000, the authors calculated the probability distribution $P_{S,L}(T)$ for interoccurrence times (e.g. waiting times) between successive events for different cutoff magnitudes (magnitude of completeness) and grid cell sizes (Fig. 3.7 a)). The range of the power law region, where the graph displays as a straight line, varies with cutoff magnitude and cell size, leading to the appropriate scaling relations for size S of the earthquakes (which is the GR-law written as $N(S > s) \propto s^{-b}$) and cell size L. The Omori law is written as $N(T) \propto T^{-\alpha}$. Unifying the two scaling relations in $P_{SL}(T) \propto T^{-\alpha} f(TL^{d_f} S^{-b})$, considering only interoccrrence times with $T > 38s$ and rescaling the coordinates of the graph in Fig. 3.7 a), yields the unified graph in Fig. 3.7 b). This graph demonstrates that all data points coincide on a single curve. The authors experimentally fitted the indices to obtain $\alpha \approx 1$ (Omori law), $b \approx 1$ (GR-law), and $d_f \approx 1.2$ (fractal dimension).

The most striking perception of this investigation is the fact, that obviously aftershocks and mainshocks can be equally simulated by the unified scaling law. Thus the aftershocks are only the short term distribution of the general earthquake occurrence. Consequently the driving mechanism for both phenomena should be the same and the commonly practised declustering of catalogues to distinguish aftershocks from mainshock activity becomes unnecessary.

In a most recent publication by *Davidsen & Goltz* (in press) the authors also investigate waiting time distributions for catalogues in California and Iceland applying the same method proposed by *Christensen et al.* (2002) and *Bak et al.* (2002). They find separate power law distributions for intermediate and short waiting times where the transition point

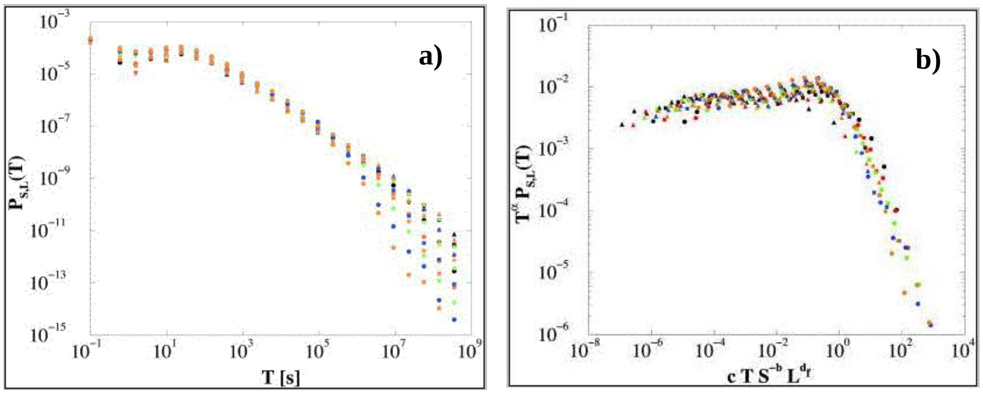

Figure 3.7: **a)** The probability distribution $P_{S,L}(T)$ of interoccurrence times T with magnitude greater than S. The symbols correspond to different cutoff magnitudes m = 2, 3, 4. The colour coding represents the grid cell size L=0.25°, 0.5°, 1°, 2°, and 4°. **b)** The data in a) rescaled by $T^{\alpha} P_{S,L}(T)$ as a function of $cTS^{-b}L^{df}$ with $c = 10^{-4}$ (see text for further explenation). From: *Christensen et al.* (2002).

of these two regimes is proportional to the size of the considered area. But in contrast to *Bak et al.* (2002) they come to the conclusion that the full distribution is not universal but depends on the complexity of the geological structure and the size of the considered area. The authors state that this is due to the spatial distribution of epicenters which does not form a simple mono-fractal (*Davidsen, 2004, pers. comm.*).

The previous examples describe the attempts to incorporate observed variations like foreshocks and aftershocks into the general appearance of seismicity patterns and explain it by SOC behaviour. However, *Main* (1995) and *Main* (1996) resumes that strict SOC behaviour is not seen in all models. *Rundle & Klein* (1993) for instance introduced a division of states into subcritical, critical, and supercritical as shown in the respective magnitude-frequency distributions in Fig. 3.8. The types of critical states correspond to structural differences and variations in the driving force in such a way that **a)** a subcritical state is observed when strong heterogeneities exist, **b)** a real critical state when weak heterogeneities and intermediate plate driving forces are apparent, and **c)** a supercritical state when weak heterogeneities and fast driving velocities are acting. It is interesting to note, that the different GR-relations calculated for the Cariaco aftershock sequence (Fig. 3.4), section 3.1.3 have a similar appearance to the proposed subcritical, critical, and supercritical states.

The introduction of the different critical states (*Main*, 1995; *Rundle & Klein*, 1993) can be taken as a first attempt to combine observed local *b*-value variations with statistical models that reproduce the general features of earthquake occurrence. Where the local mapping of *b*-values wants to reveal changes in physical parameters which influence the rupture process of one single earthquake, the idea of SOC for instance is rather focused on the assumption that the earth's crust as a whole is at a critical state (*Bak & Tang*, 1989). In this sense the local *b*-value mapping and methods from statistical physics are like a "small scale" and "large scale" approach to investigate spatio-temporal seismicity patterns. A detailed link between both is still missing.

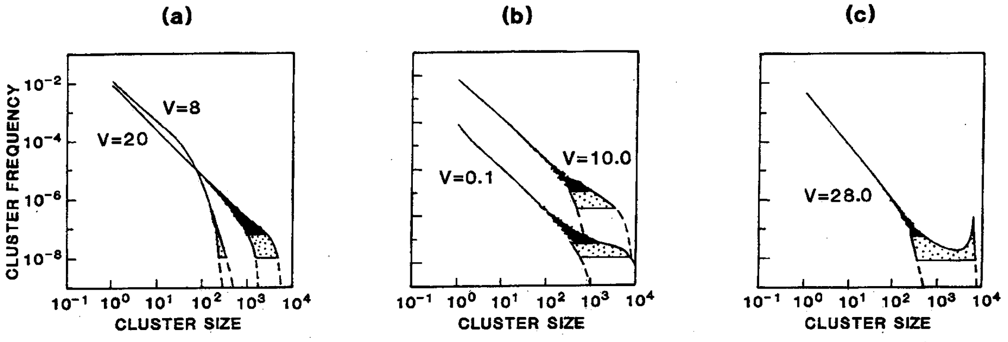

Figure 3.8: Theoretical frequency-magnitude distributions for different conditions, from: *Rundle & Klein* (1993). They correspond to a) subcritical, b) critical, and c) supercritical behaviour.

3.1.5 b-value and the fractal dimension

Among the geological phenomena which are said to be scale invariant are the frequency-size distributions of rock fragments, faults and earthquakes (*Turcotte*, 1992). This is part of the SOC concept as described in the previous section. A fractal distribution requires that the number of objects larger than a specified size has a power law dependence on the size. This is equivalent to the definition of the Gutenberg-Richter relation which thus describes a fractal relationship between the number of earthquakes and the characteristic size of the rupture. For the earthquakes the fractal scaling implies that

$$N = CA^{-\gamma} \tag{3.5}$$

where N is the cumulative number of earthquakes with rupture areas greater than A occurring in a specified area and time i.e. (*Rundle et al.*, 2003). C and γ are constants with D=2γ as the fractal dimension (*Kanamori & Anderson*, 1975). It was demonstrated that the latter equation is entirely equivalent to the Gutenberg-Richter relation with

$$\gamma = b = \frac{D}{2} \tag{3.6}$$

(*Aki*, 1981; *Turcotte*, 1992). Recent mappings of both parameters, of the b-value and the fractal dimension D, in northeast India confirms the dependence of both parameters on heterogeneity related to different geological environments. The results show that isolines of higher b-values are comparable to isolines of high D-values (*Bhattacharya et al.*, 2002). In this study the authors determine D by using the correlation dimension, which measures the spacing of a set of points defined in this case as distance between epicenters of earthquakes. *Bhattacharya et al.* (2002) prefer the correlation integral technique to the box-counting algorithm for estimating the correlation dimension.

3.2 Mapping the *b*-value of the Antofagasta aftershock sequence

3.2.1 Data processing

For the *b*-value mapping of the Antofagasta aftershock sequence the program ZMAP of *Wiemer & Wyss* (1994) was used which is a software tool to investigate and visualize statistical seismicity parameters like seismicity rate changes, magnitude of completeness, decay rates of aftershocks (*p*-values) etc. of an earthquake catalogue for a given area. The mapping technique applied to the data set is based on a grid with a certain cell size to be chosen according to the hypocenter density in the area to be investigated. At each grid node a *b*-value is calculated with a constant number of earthquakes. This means that at each grid node (x, y) the N_i nearest epicenters are selected. This constant number N_i thus leads to circles around the grid nodes with varying radii, with $r(N_i)$ being the maximum distance of an earthquake from the ith grid node. So the relation between size of the circles and density distribution of the earthquakes can be written as $r_i \sim \frac{1}{D_E}$ (*Wiemer & Wyss*, 1994; *Wiemer & Benoit*, 1996). As mentioned before, cell size and N_i have to be chosen appropriately as there is a trade off between the significance of a *b*-value anomaly and the resolution of the map. To calculate a *b*-value at a grid node with a small number of earthquakes leads to less significant features but gives a higher resolution in the mapped region.

As shown previously, the calculation of an individual *b*-value is done by using those data points of the MFR which follow a straight line. Consequently there is a lower limit towards the small magnitude end of the graph and an upper limit towards large magnitudes. This upper limit can depend on the length of the observation interval which will be addressed again in the following sub-section. The lower limit is determined by the magnitude of completeness M_c. It defines a lower magnitude threshold; so it is assumed that all earthquakes in the catalogue with $M \geq M_c$ are registered completely. In ZMAP the M_c can be either estimated visually or automatically. In case of the automatic option, M_c is the maximum of the derivative of the frequency-magnitude distribution which is the non-cumulative curve in Fig. 3.1. As the M_c strongly depends on homogeneous earthquake reporting, it varies for most catalogues in space and time. This is due in general to network configurations (reporting at network boundaries or outside of the network will get poorer), changes in network design and station distribution, or to changes in seismicity rates provoked by physical processes in the crust.

The error estimation of the *b*-value is usually done by using one of two common fitting techniques which are the maximum likelihood method (*mlh*) and the weighted least squares method (*wls*) or $\chi^2 fitting$. Both methods are integrated as options to use in the ZMAP program. While the maximum likelihood method is based on the assumption of constant standard deviations, the weighted least squares method allows for varying standard deviations (*Press et al.*, 1988). *Bender* (1983) compared various fitting techniques in *b*-value calculation to find out that *mlh* for continuous magnitude data and *wls* are both equally suitable for the *b*-value estimation. *Bender* (1983) and *Marzocchi & Sandri* (2003) studied the influence of the bin width in magnitudes on the estimation of the *b*-value. They could show that magnitude grouped data with an interval size $\delta M = 0.1$ behaves as continious data. This is the magnitude interval size also used in ZMAP. *Utsu* (1965) proposed that

b is given by

$$b = \frac{loge}{\overline{M} - M_{min}} = \frac{0.4343}{\overline{M} - M_{min}} \tag{3.7}$$

which *Aki* (1965) identified as equivalent to the maximum likelihood estimate for b. *Shi & Bolt* (1982) found the standard deviation of b as:

$$\delta b = 2.3 b^2 \delta(\overline{M}) \tag{3.8}$$

where

$$\delta^2(\overline{M}) = \sum_{i=1}^{n} \frac{(M_i - \overline{M})^2}{n(n-1)} \tag{3.9}$$

and n is the sample size. This estimation for the standard deviation is used in ZMAP.

The mapping procedure is carried out in the following steps:

- plotting the catalogue in the area to investigate, define interactively the area to be used for the calculation of the spatial b-value distribution (usually the area with the densest hypocenter distribution, hypocenters with larger uncertainties outside the network can be excluded)
- estimation of the magnitude of completeness M_c for the entire sub-catalogue to be used (this can be done also automatically and interactively by the program)
- determination of grid cell size and N_i (constant number of nearest earthquakes to be used to calculate a b-value at each grid node) by try and error, optimizing grid cell size and N_i to get a coherent map of b-values
- mapping the spatial distribution of b by computing a b-value at each grid node for the entire selected area using the maximum likelihood method as standard error estimation for b

In case of the Antofagasta aftershock sequence a grid cell size of $\sim$ 11 x 11 km (0.1° $\approx$ 11 km) and a constant number of N_i=100 was used for the b-value mapping. The average M_c is 1.8 for the sub-catalogue to represent the final mapping result. The final map calculated according to this parameters is shown in Fig. 3.9 As a first independent control for the stability and resolution of the areas of high b-values, the events with M_L > 4 are plotted in the map. It can be noted, that the epicenters of those events are most abundant in the northern low b-value area on Mejillones Peninsula, or line out the area of high b-values as to be seen around the southern area of high b-values. Here the epicenters

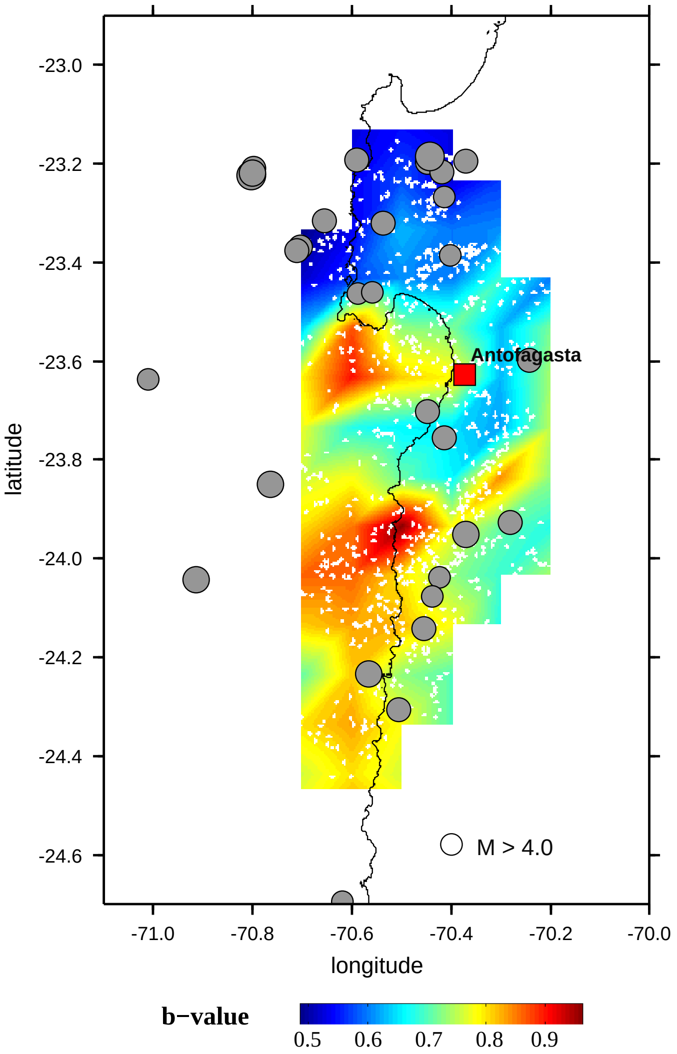

Figure 3.9: Spatial distribution of *b*-values calculated from the Antofagasta aftershock sequence (small white dots are epicenters of the aftershocks). Large grey dots denote aftershocks with M ≥ 4.0. They either line out areas of high *b*-values (red) or are located within areas of low *b*-values (blue).

are located in a rim of intermediate *b*-values of ∼ 0.8. This observation will be addressed again in sections 3.2.3 and 3.3.3.

The magnitude-frequency relation for the entire catalogue including all aftershock events for performing the *b*-value map in Fig. 3.9 has a *b*-value of 0.73 ± 0.03 (see Fig. 3.10 A)). The other two graphs in Fig. 3.10 give the GR relation for the area with the lowest *b*-values in the map, which is determined to 0.54 ± 0.03 (Fig. 3.10 B)), and for the area with the highest *b*-values respectively, determined to 1.08 ± 0.08 (Fig. 3.10 C)). For additional explanation, see also Fig. 3.11.

To examine the statistical significance of the lowest and highest *b*-values existing in the map, a significance test proposed by *Utsu* (1992) is applied. It examines the probability

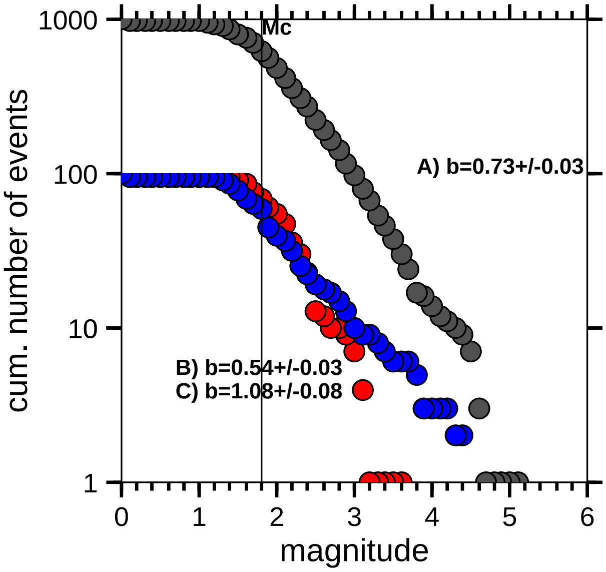

Figure 3.10: The magnitude-frequency relation for the Antofagasta aftershock sequence. Graph A gives the relation for the entire catalogue used for the b-value map in Fig. 3.9. B and C show the relation for the area of lowest and highest b-values respectively occurring in the map.

P that the two earthquake populations, n_1 and n_2, which determine the values b_{min} and b_{max}, are different (*Utsu*, 1992; *Wiemer & Benoit*, 1996). The relation taken from Utsu is written as:

$$P = exp(\frac{-dA}{2} - 2) \tag{3.10}$$

where dA is defined as:

$$dA = -2nln(n) + 2n_1ln(\frac{n_2b_{min}}{b_{max}} + n_1) + 2n_2ln(\frac{n_1b_{max}}{b_{min}} + n_2) \tag{3.11}$$

The difference of the b-values at a 99% confidence limit corresponds to $P = 0.01$. The corresponding probabilities found here for b_{max} and b_{min} is $P = 0.00034$. Further tests with neighbouring areas have been performed (see Fig. 3.11 for respective areas). In Table 3.2 (next page) the probabilities for the differences are listed.

As previously mentioned, the magnitude of completeness M_c is important for the homogeneity of the catalogue to be used for the b-value mapping and thus for the reliability of the result. Therefore M_c will be examined here in more detail for the used data set. Fig. 3.12 shows the spatial distribution of M_c for the entire catalogue in a broader map view. It can be noted that the there is a change in M_c from north to south ranging from $M_c \leq 1.5$ to ~ 2.4 at the southern end of the rupture area. The small area of $M_c > 2.5$ lies off

areas to be compared	b-values of the areas	probability P
b_{min}/b_{max}	0.54/1.08	0.00034
b_{max}/b_1	1.08/0.62	0.008
b_{min}/b_2	0.54/0.91	0.004
b_2/b_3	0.91/0.59	0.012

Table 3.2: Probabilities P for events participating in a b-value determination to be dependent on each other. To identify the respective areas, see Fig. 3.11.

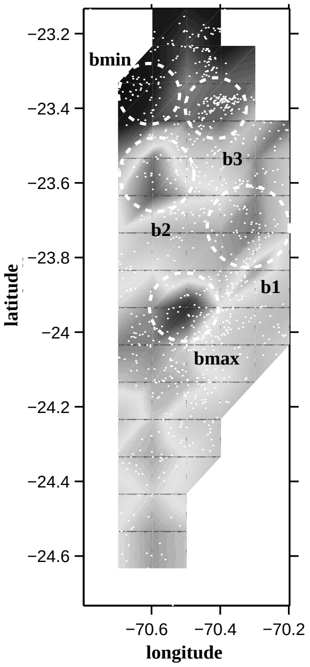

Figure 3.11: Black and white image of the b-value map. Marked by white circles are the areas which are compared according to Utsu's probability test wether the populations of earthquakes are independent. See Table 3.2 for respective probabilities.

shore. M_c increases contineously from the north to south. At $\sim$ 24.7° S on the coast (70.6° W) the map shows a jump in M_c from 2.0 to 2.5. Off shore this discontinuity is even more pronounced going from $\sim$ 1.8 to $\sim$ 2.5. This deterioration in M_c in the southern part of the study area seems to be caused by an observed decrease in number of events towards the south which at the same time is linked to a decrease in station spacing. Especially offshore there are no OBH anymore in this southern part and the onshore station density is significantly reduced.

M_c can also vary in time as examined in Fig. 3.13. The test was performed with a moving window having a sample size of 50 events per window and an overlapping of 5 events with each step. The gap in time between 95.66 and 95.69 corresponds to the time interval between sub-sequence A and sub-sequence B (see also Fig. 2.11). Each triangle gives a value for M_c. In general the values are distributed around the average M_c of 1.8 although fluctuations are somewhat broader for sub-sequence B and are more constrained for sub-sequence A. The first two values of sub-sequence A are probably due to ongoing deployment or change in network configuration and thus might be considered as outliers.

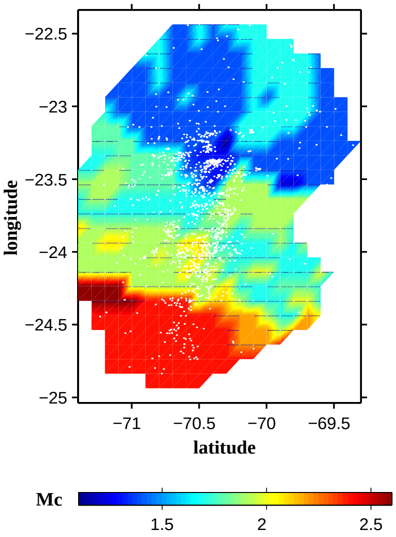

Figure 3.12: Map view of the magnitude of completeness M_c for the entire catalogue. Note the pronounced jump in M_c at the southern end of the rupture area and off shore. Coastline approximately at 70.5° W. White dots mark the epicenters of the catalogue.

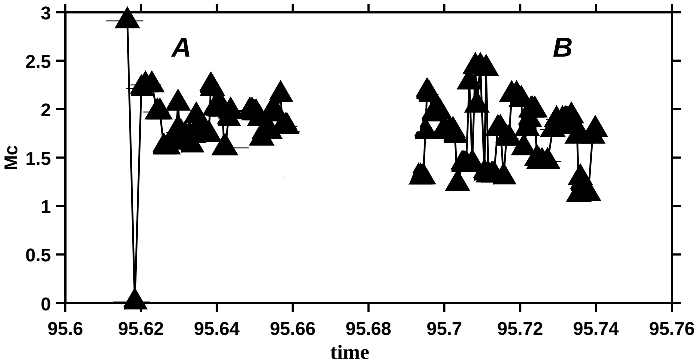

Figure 3.13: Magnitude of completeness M_c with time, examined by a moving window of 50 events sample size and an overlap of 5 events. A and B refer to the catalogue sub-sequences (see also Fig. 2.11). Each triangle marks a value for the M_c.

Fig. 3.14 examines the resolution of the b-value map in Fig. 3.9. As previously described, the radius r, which results from a constant number of events of N_i=100 at each grid node to be used to calculate b, is used to control the resolution. The map view in Fig. 3.14 thus shows, that the resolution is quite homogeneous from 23.2° S to 24.3° S with r between 10 and 20 km. r=20 km is only apparent on a small outer rim of a good resolved area of $r \sim 12$ km. The area of the pronounced aftershock cluster at 23.4° where the main shock rupture began, is characterized by a higher resolution of $r \leq 10$ km.

The standard error for each b-value at a grid node calculated according to Eq. 3.9, ranges from 0.03 to 0.11. This latter value is a single one for the grid node at 23.8°S and 70.5°W which is the area of lower b-values between the two northern and southern high b-value patches. All other values are $\delta\ b \leq 0.09$.

In Fig. 3.15 the a-values, which give the level of the seismic activity at each grid node, are shown as a funtion of the latitude. For comparison, the upper diagram in Fig. 3.15

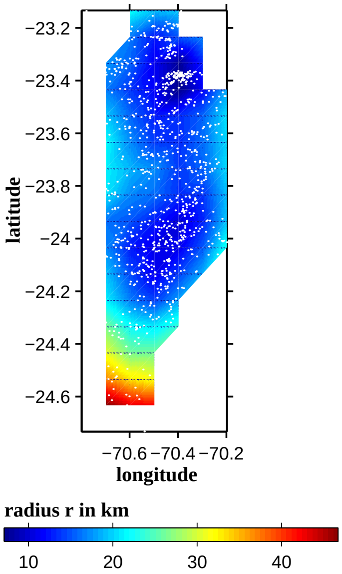

Figure 3.14: Spatial distribution of the resolution for the b-value map in Fig. 3.9. The resolution is given by the radius r in km resulting from the constant number N_i=100 event per grid node to calculate a b-value.

shows the b-values again. The general conduct of both, a- and b-values, is the same along the rupture area from north to south. Both, a- and b-values are lower in the north and higher in the southern part of the rupture zone.

For completeness of the examination, Fig. 3.16 shows the b-value map calculated with the weighted least squares method (*wls*)(left) and calculated with the maximum likelihood method (*mlh*). Both maps reveal the same features: a pronounced high b-value patch around 24°S and another patch of elevated values north of it, both seperated by a strip of lower b-values. Further to the south, b seems to stay high. The northern end of the rupture area in both maps is characterized by the lowest b-values occurring in the map. Although the general character of the map is retained, there is a difference in the absolute b-values of approximately 0.1 b in some areas. This can be seen more clearly in Fig. 3.17 where the variation in b along strike is given for the maximum likelihood method (yellow graph) and for the weighted least squares method (green graph). The highest b-value at $\sim$ 24°S is almost identical in both methods. A difference can be noted mainly between 23.6°S and 23.8°S. The streak of lower b-values ($\sim$ 0.7 in the *wls* map) and the seperation between northern high and southern high b-value patch, is better resolved in the *wls* map. (Find Fig. 3.16 and Fig. 3.17 on page 56.)

3.2.2 What can produce bias in b ?

As mentioned before, the lower limit in the MFR from where calculation of b starts is determined by M_c. The upper limit depends on the length of the observation period which determines whether the largest earthquake corresponding to the investigated sample is included or not. It can be observed, that in many case studies there are difficulties to estimate the proper limits in the MFR. This is often due to the fact that reliable seismological catalogues qualified for the application of statistical investigation methods are

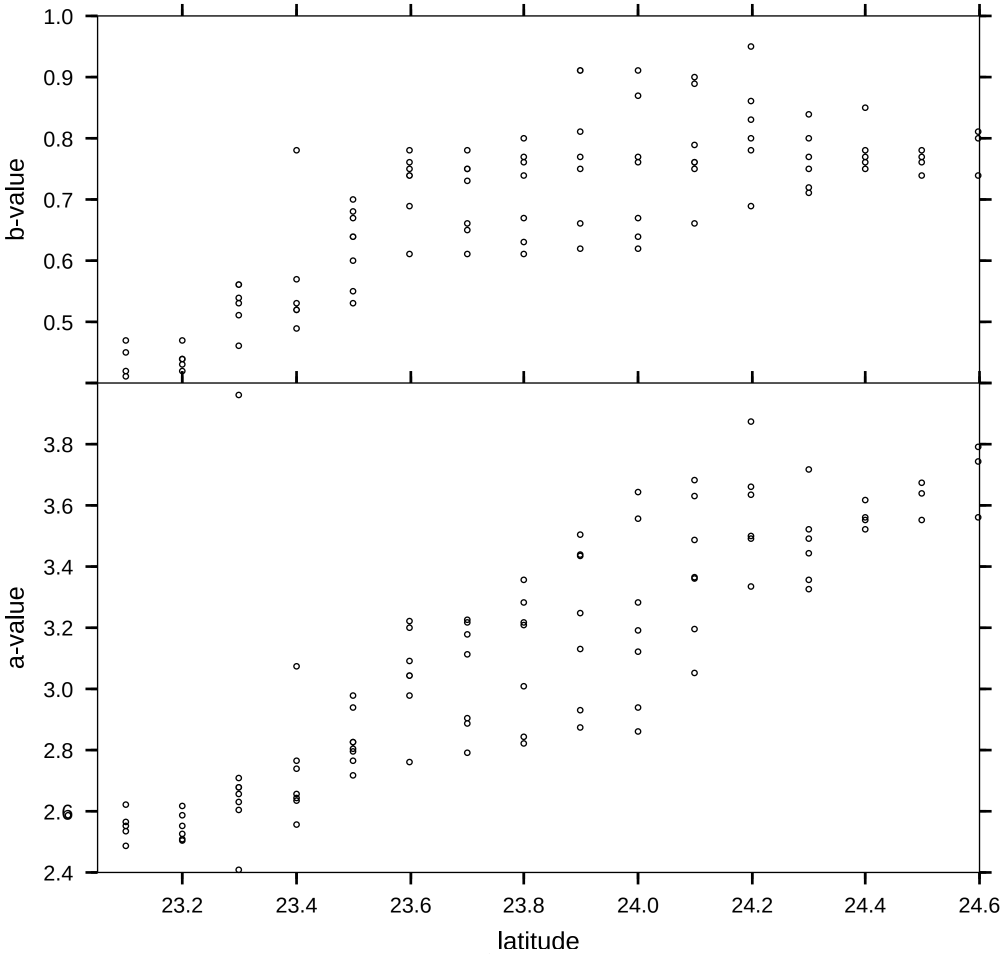

Figure 3.15: a- and b-values along strike of the rupture area. The dots mark the values at each respective grid node.

available for not more than the last twenty years except for some specific catalogues in California or Japan. However, estimated recurrence times for large earthquakes comprise often several hundred years. Thus in many cases the observation period based on instrumentally acquired data is quite short in comparison to the seismic cycle. The problem that arises is well known in seismic hazard studies when historical earthquake data should be linked to modern instrumentally recorded data. *Stepp* (1973) established a method to combine historical data of the Puget Sound area with instrumentally derived earthquake catalogues for reducing the bias in the b-value estimation caused by too short observation periods. Using intensity classes instead of magnitudes as the intensity reporting was more complete over the 100-years examined time interval, the author calculated a minimum time interval for each intensity class in which a stable mean rate of occurrence could be estimated through minimizing the error of estimation. The determined intervals, over which the earthquakes in the different intensity classes were reported completely, were then used to create an artificially homogeneous data sample which was used to calculate a corrected b-value for risk assessment in the respective area.

A similar problem can arise when an area is monitored by a temporal seismic network as used for the investigation of aftershock sequences (*Scherbaum, 1999, written comm.*). Assuming that the investigated regions have n_x events with magnitudes $\geq M_x$ and the

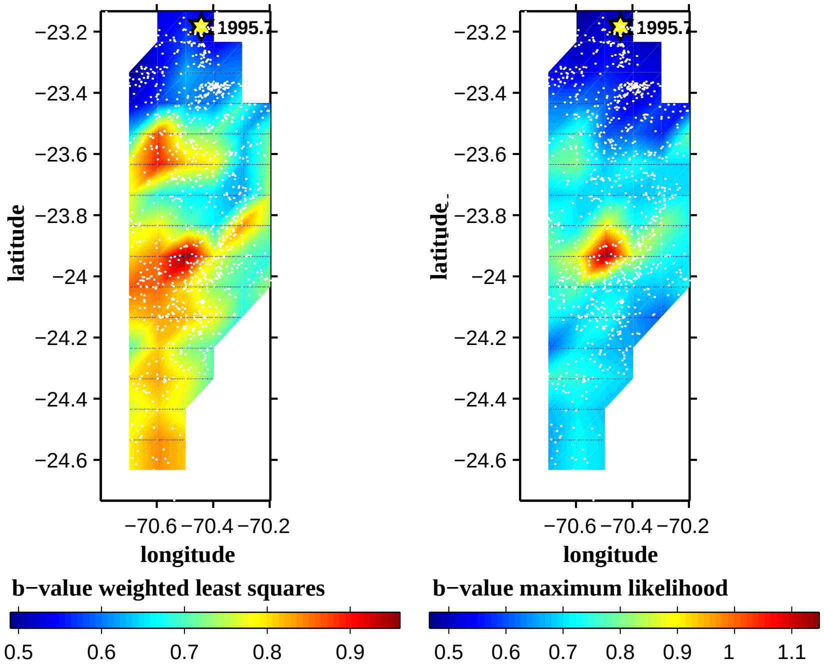

Figure 3.16: The weighted least squares method (left) versus the maximum likelihood method (right) for calculating a b-value map.

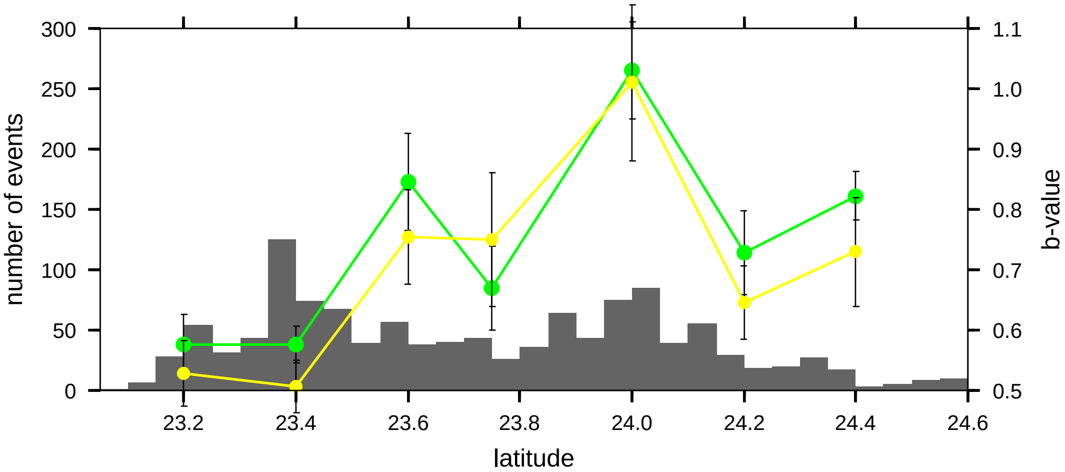

Figure 3.17: Average b-value along strike of the rupture area calculated by *wls* (green graph) and *mlh* (yellow graph). For comparison, a histogram of the number of events with latitude is also given in grey shade.

observation period is T in years. This is equivalent to a number N_i of events at each grid node to be used for the estimation of a b-value, so $N_i = n_x$ The most probable number of events N_P with magnitudes $\geq M$ which will be observed in T corresponds to the long time average of this number of events, multiplied by the probability that these number of events occur during the observation period T. Thus it can be written:

$$\begin{aligned} N_P(M_+,T) &= \overline{N}(M_+,T)\cdot P(m\geq M,T) = \overline{N}(M_+,T)\cdot(1-G(M,T)) \\ &= T\cdot\alpha_+\cdot e^{-\beta M\cdot(1-e^{-(T\alpha_+e^{-\beta M})})}, \end{aligned} \tag{3.12}$$

where α_+ and β are known from equation 3.3 and $G(M,T)$ is the distribution of the maximum magnitudes in T. The estimated frequency per year is then

$$N_P(M_+,1) = \alpha_+\cdot e^{-\beta M}\cdot(1-e^{-(T\alpha_+e^{-\beta M})}). \tag{3.13}$$

Considering this frequency per year, a distorted frequency-magnitude distribution can be written as

$$log(N_P(M_+,1)) = log(\alpha_+\cdot e^{-\beta M}) + log(1-e^{-(T\alpha_+e^{-\beta M})}). \tag{3.14}$$

With $\alpha = 10^a$, $\alpha_+ = 10^{a_+}$ and β=ln(10)b, $10^b = e^\beta$ it results

$$log(N_P(M_+,1)) = a_+ - b\cdot M + log(1-e^{-(T\alpha_+e^{-\beta M})}), \tag{3.15}$$

or

$$\begin{aligned} log(N_P(M_+,1)) &= a_+ - b\cdot M + log(1-e^{-(T\cdot 10^{a_+-bM})}) \\ &= a_+ - b\cdot M + log(1-10^{-(log(e)\cdot T\cdot 10^{a_+-bM})}). \end{aligned} \tag{3.16}$$

This means that for short observation periods the frequency-magnitude distribution is not linear. For large enough T the non-linear term is getting zero and the distribution can be described by the Gutenberg-Richter relation. For a synthetic data set of n_x=100 events, an observation period of T=3 months and M_x=1.0 it is

$$log(n_x\cdot\frac{12}{3}) = a_+ - b\cdot 1.0 \quad\Rightarrow\quad a_+ = log(n_x\cdot\frac{12}{3}) + b\cdot 1.0 = 2.6 + b \tag{3.17}$$

For the parameters used in the b-value map, which are $N_i = n_x = 100$, an observation period of 1.5 months adding up sub-sequence A and B, and M_c=M_x=1.8, the result is $a_+ = 5.2 + b$.

-	$b = 0.5$	$b = 1.0$	$b = 1.5$
M=3	-0.00002	-0.2	-1.0
M=4	-0.02	-1.0	-2.5
M=5	-0.2	-2.0	-4.0

Table 3.3: Bias in b in case of a M=3,4, and 5 event for b=0.5, 1.0, and 1.5 respectively.

The previous equations and the example show that the influence of the observation period T has universal character from the statistical point of view. This means that the bias caused in b by shorter periods of T is not related to any length of a seismotectonic process causing different type of earthquake populations like earthquake swarms, volcanic clusters, aftershock sequences or a whole seismic cycle. To cheque the influence for shorter observation periods, the data set of the final b-value map used for interpretation (Fig. 3.9), was splitted up into the sub-sequences A and B and a individual MFR was calculated for A and B respectively. In Fig. 3.18 the cumulative and non-cumulative MFR's for A and B are plotted, estimated by the weighted least squares method. The b-values of A (0.7) and B (0.75) do not differ very much from the overall b-value of 0.73 although both sequences are half as long as the complete catalogue. The FMR graphs for the sub-sequences do show a "kink" in the slope around magnitude 4.3 but it seems less pronounced than in the overall graph for the entire data set (Fig. 3.10).

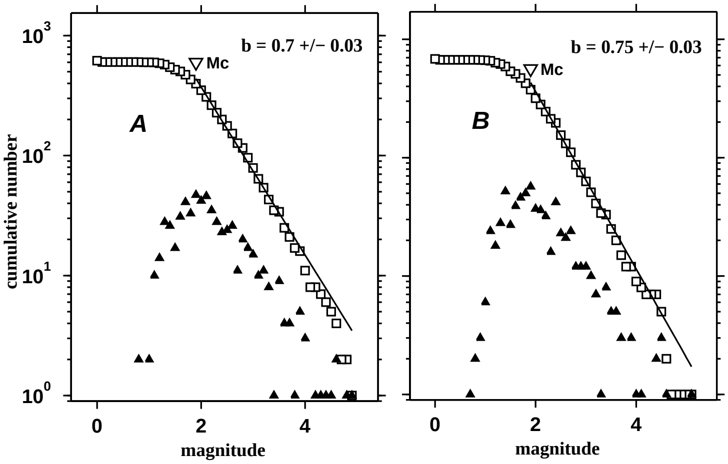

Figure 3.18: The cumulative and non-cumulative frequency-size distributions for sub-sequences A and B.

3.2.3 Summary of results

The resulting b-value map (Fig. 3.9) calculated by a weighted least squares method to estimate a b-value at each node of a grid with a grid cell size of approximately 11x11 km and a constant number of N_i=100 earthquakes, shows spatially varying b-values between 0.54 and 1.08. To test the significance of the mapped b-values, the significance test by

Utsu (1992) was applied. Table 3.2 shows that the probabilities P to be dependent are very small for two compared populations of earthquakes. Thus the mapped b-values in the characteristic areas can be considered as significant. The standard error of apparent b-values in the map ranges from 0.03 to 0.11. The mean standard error for the map in Fig. 3.20 is $\overline{\delta b}$=0.06.

Another check for the reliability of the b-value map was done through mapping the magnitude of completeness M_c for the entire catalogue of the aftershock sequence. As mentioned previously, M_c increases with latitude, exhibiting even a jump to $M_c \sim 2.5$ at the southern end of the fault plane area. North of this discontinuity at ∼ 24.3°S M_c varies between 1.1 and 1.8, which can be called fairly homogeneous. Thus for further interpretations of the b-value map in Fig. 3.9 only the area between 23.2°S and 24.3°S is considered. The temporal variations of M_c (Fig. 3.13) are fairly constant with a fluctuation around a mean M_c of 1.8. This can be attributed to a homogeneous reporting of events throughout the inspected sub-sequences A and B of the data set.

Homogeneity of the data set is evidenced by the resolution map in Fig. 3.14 for the area which is considered for further interpretation. Between 23.2°S and 24.3°S corresponding to the area of rather homogeneous M_c, the resolution is equivalent to radii ranging from 8 to 20 km with a stable "inner" region of r=10 km.

The frequency-size distribution for the aftershocks, which constitute the b-value map (grey graph in Fig. 3.10) shows a slight deviation from power law behaviour with two small kinks at M 3.7 and M 4.5. It can be observed that the number of kinks in the GR relation for the entire catalogue used corresponds to the number of high b-value patches. The M 3.7 magnitude seems to be a threshold for large aftershocks, which line along the outer limits of the high b-value structures (Fig. 3.19). Events smaller than M 3.7 can be found on the entire fault plane, events larger than M 3.7 do not appear on the high b-value sites.

Possible interpretations for the "kinks" in GR relations were discussed in detail in the previous sections. The GR relations for the area of the highest b-values around 24°S (red graph in Fig. 3.10) and the area of lowest b-values in the north of the rupture zone (blue graph) are rather undisturbed and changes in the slopes are not apparent. There are some gaps in the graphs saying that events are missing for intermediate and higher magnitudes. This might be due to the temporal gap between sub-sequence A and B (see Fig. 2.12).

For further interpretation and correlation to other seismological parameters, the b-value map resulting from estimating b by the weighted least squares method will be used. The preference to the *wls* method results on one hand from a better fit of the frequency-size distribution to a power law according to Fig. 3.1. In case of the *mlh* solution the distribution deviates much earlier from a straight line fit than the wls solution. Consequently in the wls b-value map more details in b-value variations are mapped than with the *mlh* method. The general conduct of b-values calculated by *wls* and *mlh* is the same as demonstrated in Fig. 3.17, inspecting mean b-values along strike of the fault plane area. But the absolute values differ from 0.01 to 0.1 comparing *wls* against *mlh* with the mlh values generally being lower than the *wls* values.

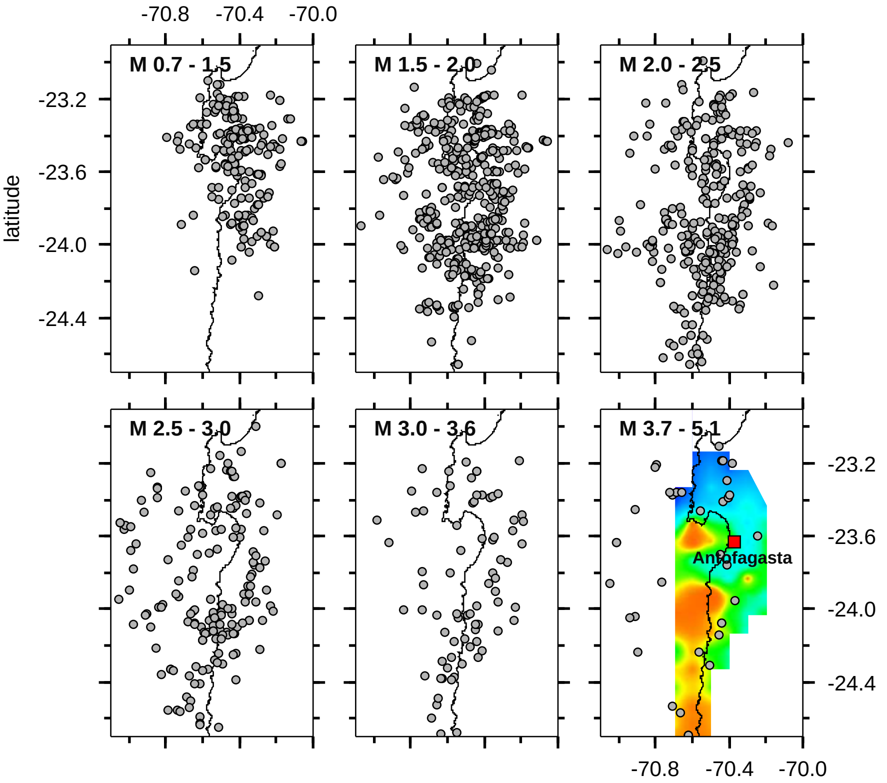

Figure 3.19: Distribution of different magnitude ranges on the fault plane. Note that the larger the magnitudes are, the more they avoid the high *b*-value patches. Magnitude M 3.7 seems to be a threshold for large aftershocks. Events with magnitudes larger than this threshold do not appear on the high *b*-value sites.

3.2.4 Description of the *b*-value map

As it was previously examined, the resulting *b*-value map for the Antofagasta fault plane area exhibits significantly varying *b*-values (Fig. 3.20). From north to south, the spatial distribution gives an alternating pattern of low and high *b*-values with dominating low *b*-values in the northern part of the map in the area of Mejillones Peninsula. From 23.9°S towards the southern end of the rupture area, high *b*-values are dominating. These areas of high *b*-values aline along the coast around 70.6°W. Besides this southward elongated distribution of elevated *b*-values, the highest *b*-values are apparent on two patch-like structures. The northern patch is located just south of Mejillones Peninsula, seperated by a "channel" of 0.1° in width of intermediate *b*-values from the southern patch of highest *b*-values on the map. This second patch is located around 24°S and has a larger size than the northern patch. This pattern suggests two assumptions:

- the division of the mapped area into a smaller northern part, dominated by low *b*-values, and a much larger southern part, incorporating the two patches of pronounced high *b*-values,
- a presumable segmentation of the area with segmentation borders between northern and southern part and eventually south of 24.2°S.

As mentioned in Chapter 2, the most conspicuous aftershock cluster at 23.4°S and 70.4°W denotes most probably the rupture start. Consequently, most of the low b-value area lies outside the main shock fault plane. So the northern part of the fault plane, still characterized by low b, has a NS extension of only 12 km from 23.4°S to 23.5°S, where the first high b-value patch begins.

According to the MFR the patches of high b-values are dominated by small aftershocks. This could result from a higher degree of heterogeneity in the structure of the material hosted in these areas, and/or lower local apparent stress. In contrast, the areas of low b-values should be dominated by larger events, suggesting a higher level of stress and/or a homogeneous structure of the material concerned. To gain some ideas for the interpretation of the b-value map and the possible physical or seismotectonic processes behind the spatial variations, the following section deals with correlations to other spatially distributed geophysical parameters in the fault plane area.

3.3 Correlation of the b-value map with:

The attempt to map the Antofagasta aftershock sequence by the GR-relation resulted in a spatially varying b-value. However, summerizing the previous sections, there are several limitations to such a b-value map. Where the centers of high or low b-value areas can be called fairly stable, the outer limits of these areas can change considerably by using different computational settings. Some statistical models explaining general patterns of earthquake occurrence even doubt whether locally varying b-values are significant.

Thus it is helpful to justify such a b-value distribution by correlating it to independently obtained parameters. In this case study the b-value map will be correlated to the main shock source time function (STF), the anomalies of the isostatic residual field (IRA), the distribution of radiated seismic energy (RSE) by aftershocks, and to v_p/v_s ratios from a local earthquake tomography (LET) study. All four parameters have in common, that they comprise material properties and thus are expected to contribute to understanding the nature of the local b-value variations.

3.3.1 - the source time function of the main shock

The source time function (STF) of an earthquake represents the release of seismic moment in time during rupture propagation. The rupture of a perfectly smooth fault would appear as a simple trapezoid in the far field time function with a single average slip value $\overline{D}$ (*Lay & Wallace*, 1995) (see also Chapter 4). But the morphology of a fault causes the structure of the STF to be more complex (*Scholz*, 1990). Usually the STF is composed of several pulsus of distinct moment or slip releases (subevents), attributed to the failure of individual asperities. This failure of asperities radiates most of the high frequency seismic energy during the main shock rupture and thus is important in earthquake hazard analysis (*Kanamori & Stewart*, 1978; *Scholz*, 1990; *Lay & Wallace*, 1995).

The STF of the 1995 Antofagasta earthquake which will be correlated to the b-value map was calculated by *Delouis* (1996), and *Delouis et al.* (1997), using broadband teleseismic data from the global seismic network. Station sites used were located at distances between

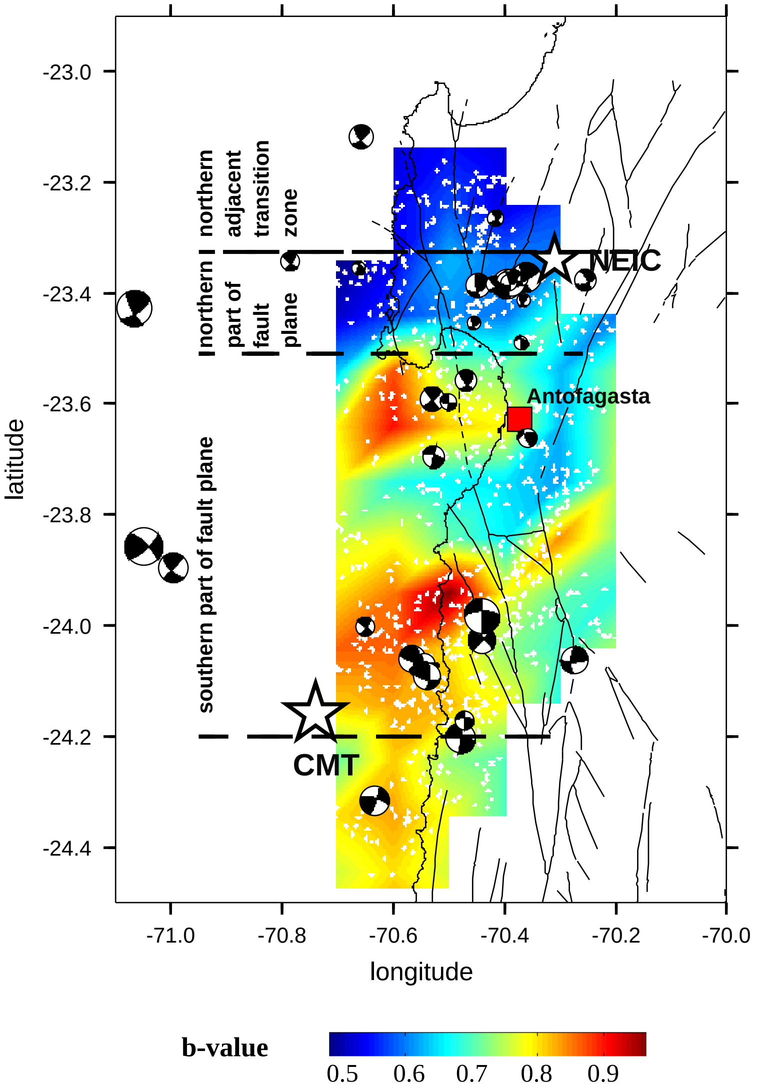

Figure 3.20: b-value map of the fault plane and its suggested partitioning into a northern and southern part. Black lines mark the suggested boundaries of the segments. Strike slip events are plotted as they are assumed to be linked to segment boundaries (for further explanation see also Chapter 5). White stars mark the start of the rupture in the north (NEIC solution for hypocenter) and the center of the rupture (CMT solution).

30° and 96°. The total STF consists of six subevents of which four confirm the principle rupture modeled by four individual propagating line-sources in a final inversion (Fig. 3.21).

The first 115 s of the P-wave signal and 170 s of the SH-wave signal were used for the body-wave modeling applying the algorithm of *Nabelek* (1984). Filtering of the signals was performed by a Butterworth filter with cutoff frequencies of 0.01 Hz to 0.8 Hz for P-waves and 0.01 Hz to 0.4 Hz for S-waves. Sampling rates were 2 samples/s and 1 sample/s respectively. Before the inversion the seismograms were normalized to an epicentral distance of 40° and to the same amplification (*Delouis et al.*, 1997).

For the crustal model the authors assumed a homogeneous half space. Density at the

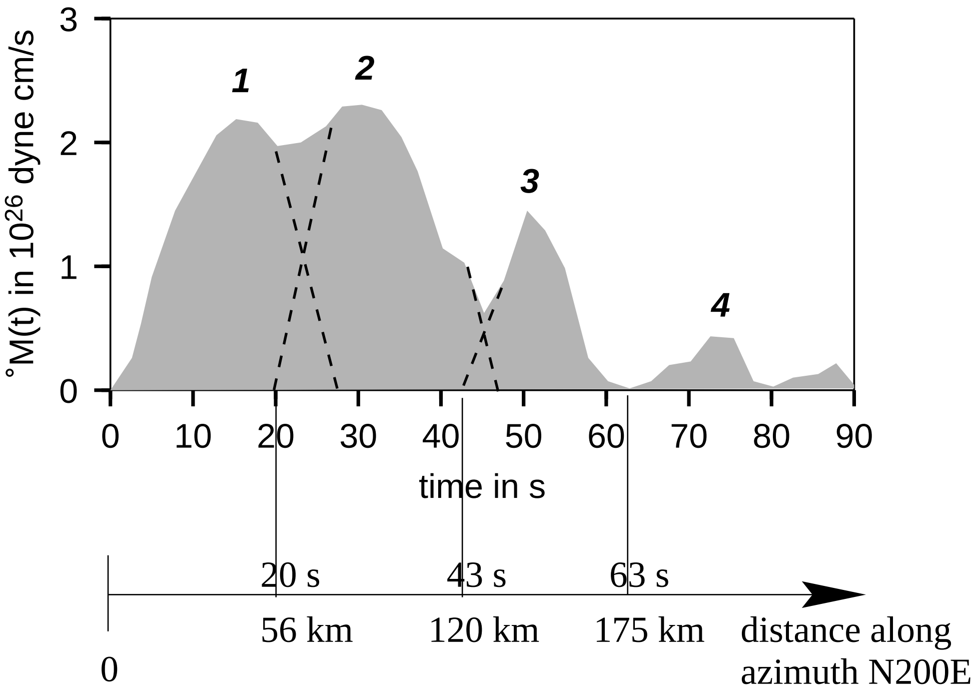

Figure 3.21: Source time function for the 1995 Antofagasta earthquake as calculated by *Delouis* (1996). The numbers above the peaks of the curve name the four subevents which are resolved by a final inversion using a propagating line source. A constant rupture velocity of 2.8 km/s was assumed.

source was set to 2.85 $\frac{g}{cm^3}$ and 2.75 $\frac{g}{cm^3}$ at station sites; Poisson's ratio had a value of 0.25. The velocity for the P-wave ranged from 6.0 km/s underneath the stations to 6.6 km/s at the source. Regarding anelastic attenuation t^* was taken as 1.0 s for P-waves and 4.0 s for SH-waves. Weighting was attributed to the signals to account for the azimuthal distribution of the stations.

As a first step an individual inversion for seismic moment rate at each station was performed to solve for directivity of the rupture propagation. This yielded a clear southward directivity of the propagating rupture somewhat oblique to the trench. As the point source representation is inconvenient for large earthquakes, four propagating line sources were implemented in a final inversion procedure. The first line source starts at the nucleation point of the event which is taken as the hypocenter determined by the local network (see Table 2.2 in Chapter 2). The recovered STF is therefore subdivided in at least four liberation episodes of seismic moment, which begin at 20, 43 and 63 s respectively after rupture initiation. The total duration of the STF is 90 s; more than 90% of the moment release takes place in the first 120 km of rupture propagation (see Fig. 3.21) (*Delouis*, 1996).

Correlation of the STF to the b-value map:

For the correlation with the b-value map it is convenient to link the starting point of the STF with latitude 23.2°S. This is somewhat further north to the starting point used by *Delouis* (1996) at 23.43°S according to the hypocenter determination of the local network. ISC and NEIC report the hypocenter around 23.3°S (see Table 2.2 in Chapter 2). However, the area comprising 23.2°S to 23.4°S will be interpreted later as a transition zone between ruptured and unruptured part of the fault. These 0.2° are equivalent to a distance of approximately 20 km which is well within error ranges for hypocenter determinations. Correlating the STF with the b-value map using the geographical coordinates as reference frame for both is justified by the unilateral rupture propagation with southward directivity.

The visual inspection of the correlation shows a striking congruence of the first two maxima in the STF with the center areas of the two respective high b-value patches ($b>0.9$) (Fig. 3.22). Discribing the correlation from north to south, the transition and the northern part of the fault plane, governed by low b-values, correspond to the first 10 s of the STF. The kink in the STF at 10 s seems to correlate to the northern limit of the first high b-value patch, the kink at 20 s links to the southern limit of this area respectively. The low b-value space, which seperates the northern from the southern high b-value patch, could have a correspondence in the STF where the increase in seismic moment rate is rather small (20 s to $\sim$ 24 s). After 24 s, $\dot{M}(t)$ is increasing again to maximum 2 of the STF. The part of the STF between 40 s and 43 s features an indentation into the elongated high b-value area towards the south by lower b-values around 0.7 to 0.75. The exact minimum in the STF at $\sim$ 42 s appears to be shifted further south in comparison to the low b-value indentation. South of approximately 24.3°S, which lies between 40 and 43 s in the STF, the b-value map gets rather speculative due to the lack of recorded aftershocks. In Fig. 3.14 it can be seen that the resolution of the b-map decreases drastically south of 24.4°S.

Comparing the first three episodes of the STF (Fig. 3.22) with the *wls* determined b-value curve along strike of the fault plane in Fig. 3.17, the positive correlation between both curves is obvious. This indicates clearly that high moment release caused by the main shock correlates to high b-values in the aftershock sequence.

As a general result of the correlation it can be stated that the largest part of the main shock related moment release (80%) within the first 120 km of the rupture (*Delouis*, 1996; *Delouis et al.*, 1997; *Carlo et al.*, 1999) comprises the area where the two distinctive high b-value patches are located. Within this framework, maximum 1 and 2 are perfectly correlated to the highest apparent b-values. Even the respective northern and southern limits of the two high b-value patches seem to be confirmed in changes in the STF. The congruence of high seismic moment release with high b-values suggests the interpretation that these areas are asperities, which rupture in a distinctive manner during the main shock. The two maxima in the STF, corresponding to two subevents, can be identified in the seismograms as seperately arriving signals (*Delouis*, 1996; *Delouis et al.*, 1997). Following the interpretation it is deduced that the spatial distribution of b-values obtained from the aftershocks of the 1995 Antofagasta earthquake identify the locations and, with some limitation, also the size of the asperities ruptured during mainshock propagation.

Four published slip models for the Antofagasta earthquake could be found in literature: **1)** the STF from *Delouis* (1996), as discussed in the previous paragraphs, **2)** the STF calculated by Tanioka and Ruff, which has very similar characteristics to the STF of *Delouis* (1996), **3)** a spatial slip distribution by *Ihmlé & Ruegg* (1997), where two separate patches of high slip can be distinguished. These patches are similar in appearance to the patches of high b-values identified in the b-value map. **4)** The STF by *Carlo et al.* (1999) in not as detailed as the previous ones, but shows a concentration of high slip release in

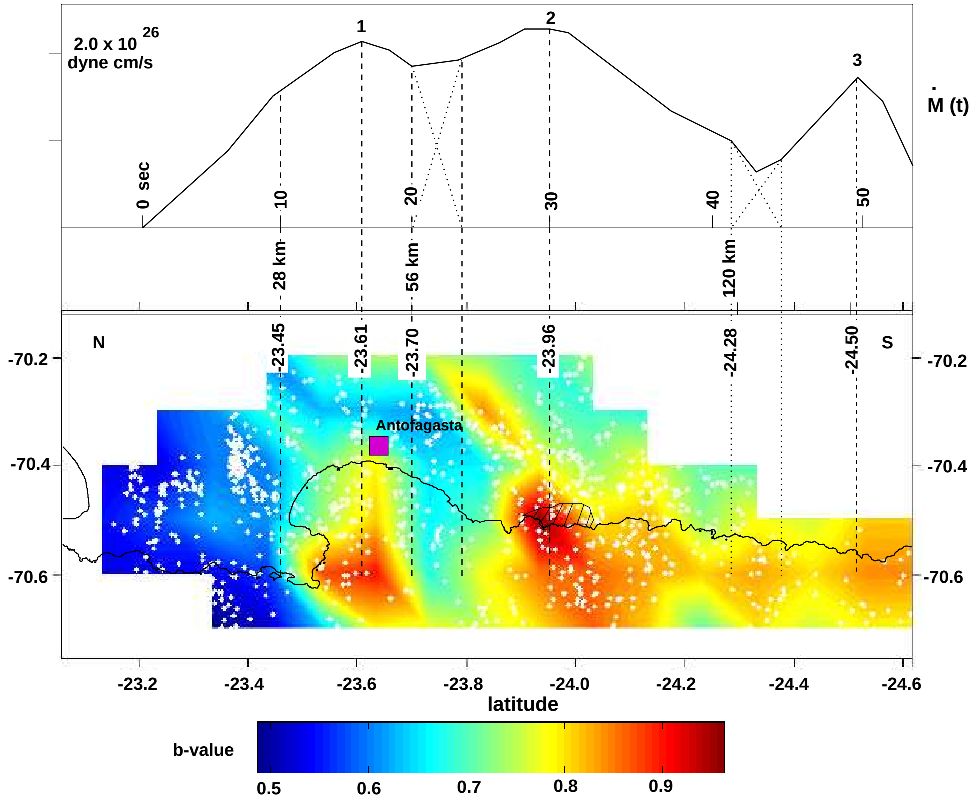

Figure 3.22: Correlation of the STF of the Antofagasta earthquake with the spatial *b*-value distribution derived from the aftershock sequence. The different episodes of moment release in the STF are numbered (1, 2, 3). Dashed lines link features of the STF to features of the *b*-value map for which distances from rupture start are given in seconds, respective kilometers, and geographical coordinates. The small hatched area in the second patch of large *b*-values locates the outcrops of the Coloso Coastal Gabbro Complex (*Pichowiak*, 1994).

the first 120 km of rupture history. Comparing the STF's of *Delouis* (1996), Tanioka and Ruff and *Ihmlé & Ruegg* (1997) with respect to the first maximum in the functions which is used to define the position of the center of the northern asperity, some variation in the position of the maxima can be seen. Where the the maximum in Tanioka and Ruff's STF appears $\sim$ 4.2 s earlier in the function, the first patch of large slip in *Ihmlé & Ruegg* (1997)'s begins approximately 10 km further to south of the *b*-value patch. This gives a variability in position of approximately ± 20 km.

3.3.2 - the isostatic residual field

Within the framework of the SFB 267 (see Chapter 2), investigation of the gravity field was a major target (*Götze et al.*, 1994). Therefore a high resolution data set of gravity measurements and also the inversion for the isostatic residual field are available for the area around Antofagasta and Northern Chile. As the fault plane of the Antofagasta earthquake comprises an area along the coast, gravity data from onshore as well as offshore measurements had to be considered. The onshore gravity data was recorded by landbased stations with a spacing of approximately 5 km along the track lines. For computational purposes this resulted in a grid cell size of ~ 15 x 15 km which is similar to the grid cell size of 11 x 11 km used to derive the b-value map. Taking into account the strong topography onshore, the complete station Bouguer anomaly is terrain-corrected within a radius of ~ 167 km. A standard density value for the crust of 2.67 $\frac{g}{cm^3}$ has been applied for mass corrections (*Götze & the MIGRA group*, 1996). Line data from recent marine gravity surveys during the CINCA'95 and SPOC experiments (*Kösters et al.*, 1997; *Götze & Kirchner*, 1997) were used for offshore gravity data compilation. Along track, approximately 15 observation sites were recorded per 1 km. The marine gravity surveys were tied to the Chilean National Gravity Network at reference stations in Valparaiso, Antofagasta, and Iquique. The computation of the isostatic residual anomalies was done by using a Vening-Meinesz model with a rigidity of $D = 10^{23}$ Nm (*Banks et al.*, 1977). The isostatic regional field, representing the long wavelength effect of the crustal root compensating the topography, was computed assuming a crustal density of 2.67 $\frac{g}{cm^3}$ and a mantle density of 3.17 $\frac{g}{cm^3}$. This means that for isostatic calculations, the crust-mantle density contrast is approximately -0.50 $\frac{g}{cm^3}$. The reference crustal thickness is set to 35 km.

According to the computing of the isostatic residual field (IRF) (*Götze et al.*, 1994; *Götze & Krause*, 2002), two pronounced anomaly structures of up to 150 mGal evolve in the Antofagasta section presented in Fig. **??**. There are a rather small one south of Mejillones Peninsula at ~ 23.6°S and a large elongated anomaly, starting north of 24°S, heading southward. Both anomalies discussed here, belong to a conspiceous chain of positive isostatic residual anomalies, which can be traced along the entire South American Pacific coastline reaching the city of Concepción in Southern Chile. The two anomalies located in the Antofagasta section, are attributed by *Götze & Krause* (2002) to the uplifted Jurassic batholiths El Cobre and Coloso Coastal Gabbro Complex (*Pichowiak*, 1994) which intruded into the settings of the Formación La Negra.

Fig. 3.23 shows the isostatic residual anomaly map next to the b-value map. Despite the discussed limitations in resolution for both maps, the correlation is remarkably good. The northern smaller patch of high b-values coincides well with the small IR anomaly south of Mejillones. The larger southern high b-value patch and the pronounced IR anomaly starting north of 24°S coincide well and have both an elongated character with southward directivity. In general, areas of $b > 0.8$ coincide with areas of $\delta g_i > 50$ mGal in the IRA map.

Non-zero isostatic residual anomalies occur where bodies of higher or lower densities were used for the gravity anomaly computation. In addition, structural processes which hinder isostatic compensation or even work against it, can produce IR anomalies. In case of northern Chile it is most likely, that both processes play a role in the generation of the proposed asperities (*U. Meyer, 2004, pers. comm.*).

If the isostatic residual anomalies are identical with the dense bodies of the intruded batholiths, the following mechanical process can be proposed to have a major part in generating the asperities in the Antofagasta region (see Fig. 3.24): Due to density differences a buoyant force is operating on the subducting Nazca plate in the area of the seismogenic zone which is directed upward. The gravitational force, acting on the batholith structures

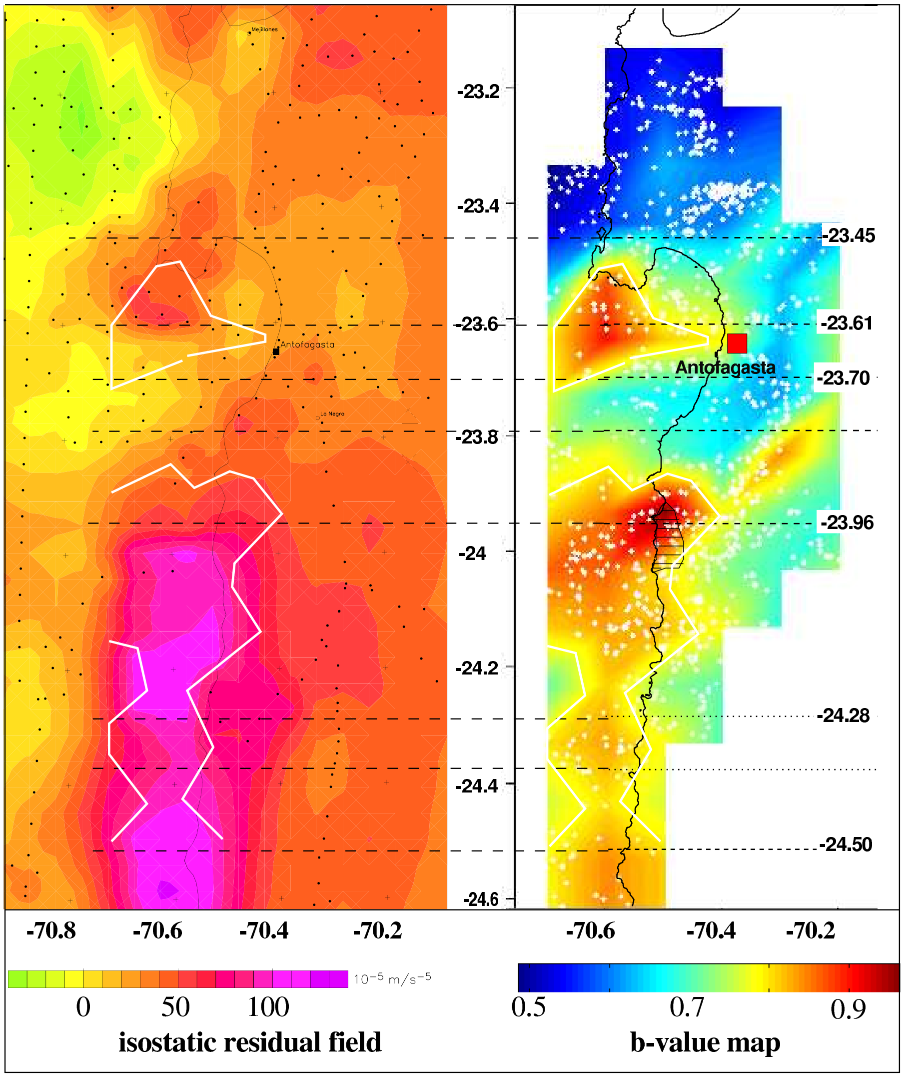

Figure 3.23: Correlation of the isostatic residual anomalies located in the Antofagasta region with the b-value map. Hatched lines are taken from the correlation of the STF with the b-value map and are projected to the IR map. Note that the centers of the high b-value patches match very well with the largest gradients in the isostatic residual field. White isolines give the outer limits for areas of $b > 0.8$. They are also projected onto the IRF. The IRF is plotted after *Götze et al.* (1994). See text for further explanation.

is opposing this buoyant force. As a consequence, the area where this happens gets locked. These locked zones are forming the asperities which themselfs are part of the seismogenic zone (Fig. 3.24). Considering this mechanical process, two substantial statements can be made about the nature of the asperities:

- The "loading" of the asperities is driven through the permanent convergence of the Nazca and South American plates in combination with the opposing forces acting on the seismogenic zone caused by the buoyancy of the Nazca plate and the extra load of the batholitic structures located in the upper crust.

- The material involved in forming the asperities is either very compacted material constituted of erroded and subducted sediments and rocks or consists of the respective compositions of the batholithic structures like diorites to granodiorites or low- to highgrade metamorphic rocks from intrusions (*Pichowiak*, 1994).

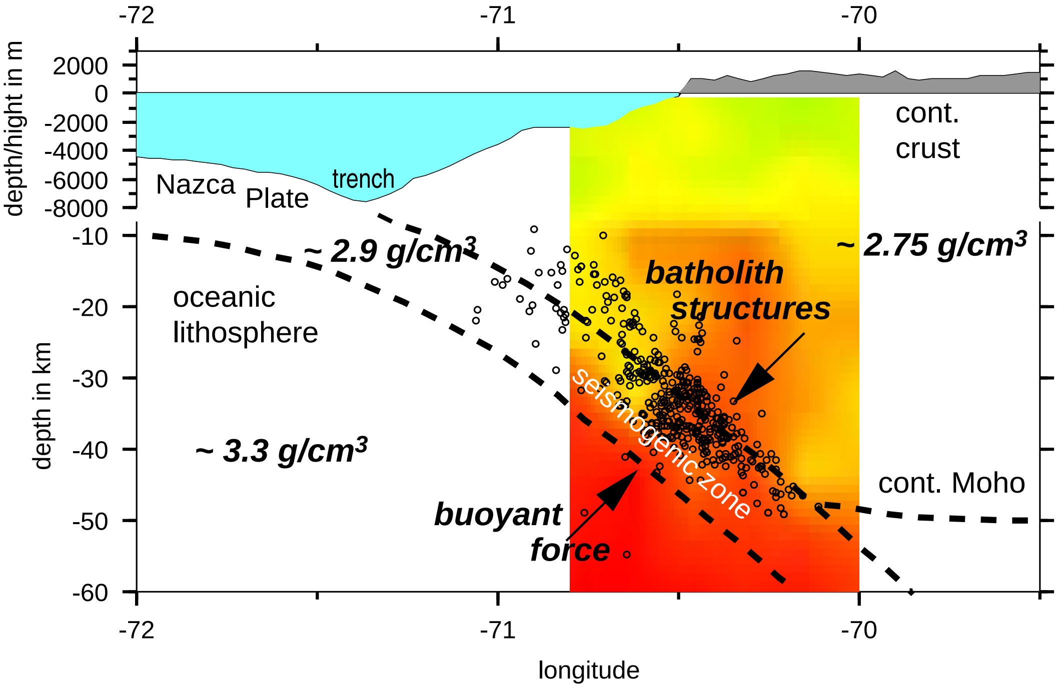

Figure 3.24: Scheme of a vertical WE profile of the subduction zone at 24°S. The small black circles give the aftershock hypocenters. The arrows mark the opposed forces of buoyancy of the Nazca plate and the extra load of the batholitic structures in the area of the seismogenic zone. The numbers marked in the figure give the approximate densities of the subducting oceanic crust, the oceanic lithosphere, and the continental crust respectively. The batholith structures are taken from a local earthquake tomography study by *Husen* (1999). See text for further explanation.

Considering now the congruence of the high b-value patches with the high IRA's, it can be concluded that the high b-values have some relation with the dense or compacted material forming the asperities. Taking further into account the positive correlation of high b with high main shock moment release, the following hypothesis can be developed: The main shock rupture, often initiated in some distance to any inhomogeneity or asperity on the fault (*Mai*, 2002), yields to exeed the strength of the locked asperity structures which results in high moment release when the main shock rupture "hits" the asperity. As high moment release is identical with high slip, this action could lead to a degree of damage which is similar to a shattering of the area. Thus a large number of relatively small ruptures with low magnitudes could evolve in favour of larger ruptures with high magnitudes in the affected areas. Successively this setting would cause a high b-value. It should be most likely, that the shattered area characterized by a high degree of damage, is confined to the high density material. Thus it can be proposed, that the high *b*-values consequently map out the damaged material zones which are evidently congruent with the main shock high moment release and the dense bodies of the batholiths in the Antofagasta region.

3.3.3 - the aftershock radiated seismic energy distribution

The radiated seismic energy E_s is a measure of seismic potential for damage, as it is calculated from the velocity power spectra of seismograms and thus represents the high frequency part of the earthquake process (*Choy & Boatwright*, 1995). E_s is related to the seismic moment M_o through the apparent stress which is defined as $\tau_a = \mu E_s/M_o$ (*Wyss & Brune*, 1968) and describes the difference between the stress causing slip and the frictional stress resisting slip (*McGarr & Fletcher*, 2002). In general, all three (E_s, M_o, and τ_a) are fundamental earthquake source parameters which allow to relate earthquakes to important aspects such as damaging ground motion, crustal deformation, and lithospheric strength as functions of space and tectonic setting. For instance *McGarr & Fletcher* (2002) and *Choy & Boatwright* (1995) found systematic variations of E_s and τ_a between compressional and extensional tectonic settings in such a way that the parameters showed higher peak values in compressional environments and that lowest apparent stresses could be associated with thrust earthquakes in subduction zones.

An important observation for the discussion here is the heterogeneous spatial distribution of both parameters on fault planes as described by i.e. *McGarr & Fletcher* (2002) and *Ide* (2002). Examining the distribution of main shock derived E_s and τ_a on the fault planes of five major earthquakes, *McGarr & Fletcher* (2002) could summerize that high values of each parameter tend to correlate with high estimates of slip. But also areas of high slip rates were observed to be subject of high E_s and τ_a. However, the authors also found that this patch on the fault which radiates the most seismic energy is not always near the hypocenter of the main shock.

Ide (2002) studied the spatial distribution of E_s of two japanese earthquakes and found that the radiated energy was concentrated either near the hypocenter and/or the initial rupture points of asperities. He further could identify areas of negative radiated energy near the edges of areas with large slip. *Ide* (2002) calls these areas relaxation barriers, which are characterized by a difference between elastic potential energy and frictional work. The effect of such an area would be the deceleration of the rupture front and the reduction of the total radiated energy.

The previous examples of mapped spatial variations in E_s are all derived from main shock teleseismic data. To find further evidence for the physics of the presented *b*-value map, here the post-seismic distribution of E_s derived from the aftershocks will be estimated and mapped in the fault plane area. For this purpose, the empirical relation

$$\begin{aligned} logE_s &= a + bM_s \\ &= 4.4 + 1.5M_s \end{aligned} \tag{3.18}$$

after *Choy & Boatwright* (1995) was used which is an improved version of the original

Gutenberg-Richter relation of $logE_s = 4.8 + 1.5M_s$ (*Gutenberg & Richter*, 1956). *Choy & Boatwright* (1995) computed E_s for a set of 397 global shallow earthquakes from velocity-squared spectra of body waves and thus were able to correct the constant a in the original GR relation. In Fig. 3.25 a) and b) the radiated seismic energy versus magnitude for the data set of *Choy & Boatwright* (1995) and the respective graph of the aftershock sequence studied here are shown.

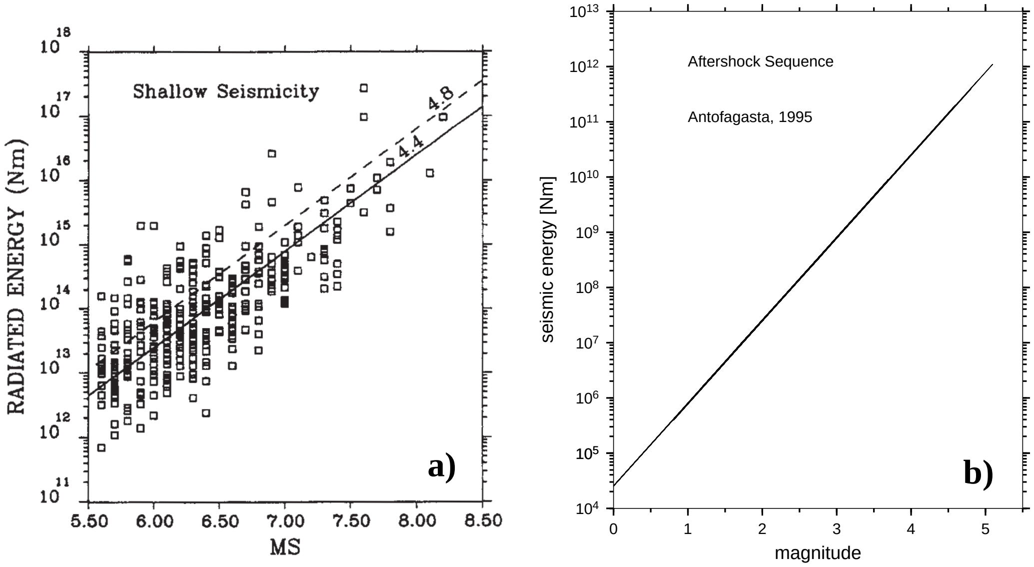

Figure 3.25: a) Radiated seismic energies versus magnitudes (M_s) for 397 shallow global earthquakes after *Choy & Boatwright* (1995). A least-squares regression analysis of the data yields 4.4 for a in relation 4.2. The dashed line shows the regression from the original GR relation. b) Radiated seismic energies versus magnitudes from the Antofagasta aftershocks.

The empirical relation (Eq. 3.18) uses M_s as a magnitude scale. The aftershocks have a local magnitude M_L and thus would have to be transformed into M_s. Trying to do this by using the correlation relations of *Gutenberg & Richter* (1956), $M_s = 1.27(M_L - 1) - 0.016M_L^2$, and another one by *Ambraseys & Bommer* (1990), $0.80M_L$ - $0.60M_s = 1.04$, just shifted the graph on the y-scale in Fig. 3.25 b). Simply assuming $M_L = M_s$ yields the graph in Fig. 3.25 b) which is a perfect continuation of the graph in a) for the smaller magnitude aftershocks. To have an idea about individual values for the aftershock energy estimations Table 3.4 gives some examples for larger afterhocks. The values derived here are in good agreement to calculated E_s for smaller global events listed in *Choy & Boatwright* (1995).

For further processing the fault plane area was gridded into cell sizes of 10x10 km which is identical to the grid cell size used for the b-value map. The individual energies of aftershocks in each cell were summed up to obtain a radiated seismic energy density. The interpolated version of this spatial distribution can be seen in Fig. 3.26 b).

Considerable variations of the energy are apparent in the map ranging from 8.2x10^{-6}

M (M_s=M_L)	E_s [Nm]
5.1	1.1 x 10^{12}
4.8	3.98 x 10^{11}
4.6	2 x 10^{11}
3.9	1.8 x 10^{10}
3.7	8.9 x 10^{9}

Table 3.4: Radiated seismic energy E_s for some large aftershocks.

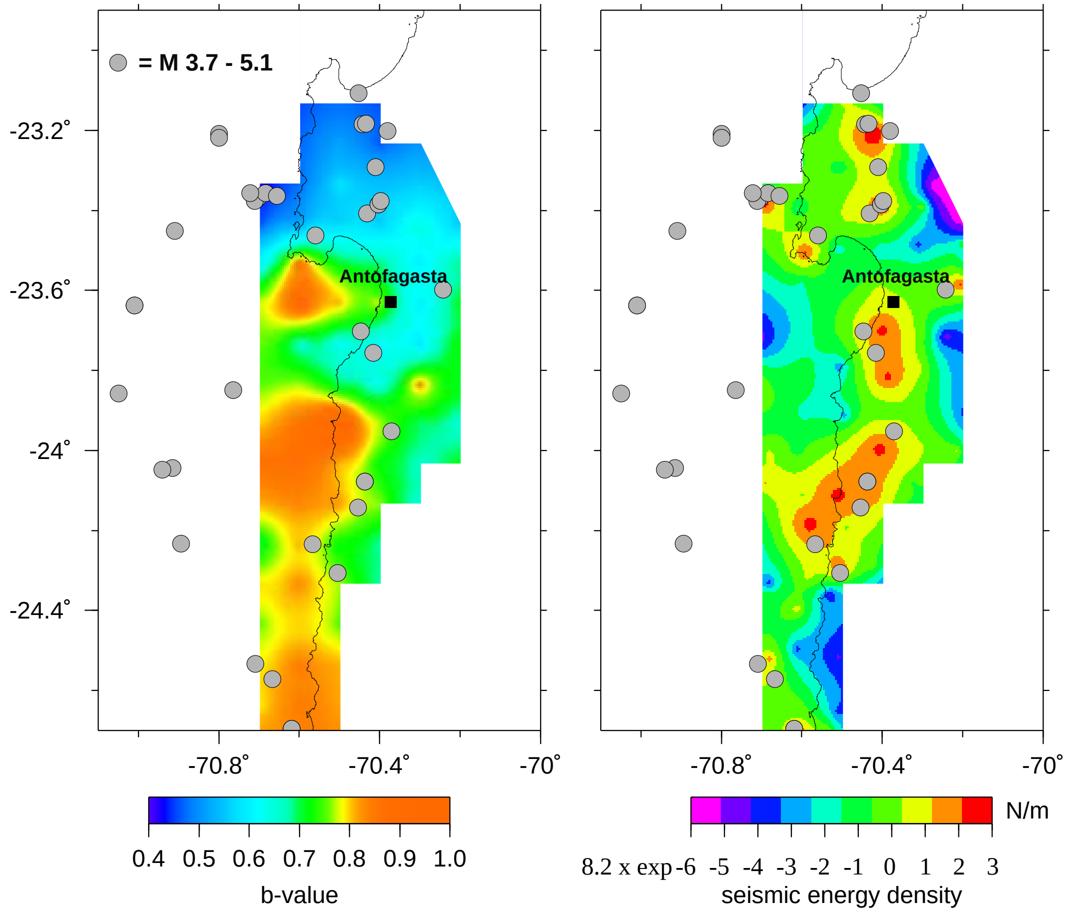

Figure 3.26: a) *b*-value map. b) Spatial distribution of radiated seismic energy densities derived from the Antofagasta aftershocks (e-map). Grey dots in both figures give the hypocenters of aftershocks with M > 3.7.

Nm to 8.2x10^3 Nm (Fig. 3.26 b). A concentration of high radiated seismic energy can be noted as an elongated NNE-SSW trending feature starting north of 24°S, ending approximately around 24.2°S. Other patches of high aftershock E_s are located south of Antofagasta and in the area of Mejillones Peninsula.

Comparing the *b*-value map to the seismic energy density map (e-map) (Fig. 3.26), it can be recognized that the energy tends to be high where *b*-values are low. This is especially true for the northern part of the fault plane and the adjacent transition zone underneath Mejillones Peninsula. The low *b*-value "channel" seperating the two high b patches, is at least in its onshore part marked by high energies. The southern high energy elongated feature is situated in an area of intermediate *b*-values, even overlapping in some part the southern high *b*-value patch. This could be due to the slightly different mapping technique for the *b*- and *e*-map.

Combining these observations with the previously obtained knowledge about the tectonic setting and the main shock moment release in the fault plane area, the following statements can be made:

- The southern elongated high energy area (Fig. 3.26 b) orientates itself obviously along a boundary between high and intermediate *b*-values which can be interpreted also as a material boundary. This argument is valid since the high *b*-values are found to map out most likely the impression of the batholiths on the fault plane. Consequently aftershock energy density is sensitive to material gradients or tend to be located along bodies of high density.
- High aftershock energy density can be found in transition zones marked by low *b*-values. Here stresses are getting higher in the post-seismic interval due to the stress release in the neighbouring high slip areas.

Comparing *b*-map and *e*-map again it can be noted, that the general character of the *b*-map is a more plainary one, mapping areas and surfaces whereas the *e*-map is characterized by the concentration of peak values in a more linear manner. This can be explained by the fact that the spatial distribution of radiated energies is dominated by the aftershocks with larger magnitudes (*Shcherbakov & Turcotte*, in press). It is varified in Fig. 3.26 through the grey dots that give the hypocenters of aftershocks with M>3.7. They aline well with the peak values of the energy density distribution. In contrast, the spatial distribution of *b* results from the proportion of small to large magnitudes in the seismogenic volume. Considering a material to have a characteristic relation between large and small fractures opening under certain stress conditions, the *b*-value would be similar to a material property and consequently could map the spatial extent of this material.

From these observations it can be hypothesized that the *b*-value distribution might be more useful to map the spatial extent of asperities and transition zones whereas energy densities are high in both cases: at material boundaries and in transition zones. Consequently from the *e*-map alone, it is not possible to distinguish between those two settings. In general the *e*-map could be useful in aftershock hazard as it represents the locations of large aftershocks. The *e*-map further helps to evaluate the *b*-value map. As high radiated seismic energy appears to be located at material boundaries, it can proof the outer limits of the *b*-value mapped asperities. The energies also confirm the transitions zones characterized by low *b*-values as they take up stress in the aftershock re-distribution process and thus should be subject to high magnitude aftershocks.

3.3.4 - v_p/v_s ratios from local earthquake tomography studies

A high resolution 3D velocity tomography was carried out by *Husen* (1999) with the same data set used for the presented work. This data set contains 32525 *P*-wave first arrivals and 17453 S-wave picks which made it possible to image v_p/v_s ratios through the final tomographic model. The ratios were obtained by the 3D simultaneous inversion of v_p, v_p/v_s and hypocenter locations (*Husen*, 1999; *Husen & Kissling*, 2001).

In general, velocity ratios are functions of the structure and micro-structure of rocks and thus can be used to characterize different types of rock (*Schön*, 1983). In hydrocarbon exploration the v_p/v_s ratio is used as an indicator for consolidated or unconsolidated formations and for the presence of gas or oil in these formations (*Gregory*, 1977). This implies that parameters like crack density, porosity, pore pressure, confining pressure and type of fluids influence the v_p/v_s ratio, which is defined as

$$\frac{v_p}{v_s} = (2\frac{1-\nu}{1-2\nu})^{1/2} \tag{3.19}$$

where ν is the Poisson's ratio, which is the ratio of the radial to axial strain when a uniaxial stress is applied (*Schön*, 1983; *Lay & Wallace*, 1995). It has been observed, mostly under laboratory conditions, that v_p/v_s increases with i.e. increasing crack density but also with increasing pore fluid pressure and fluid flow in general (*Schön*, 1983; *Eberhart-Phillips & Michael*, 1993; *Husen & Kissling*, 2001).

Fig. 3.27 shows spatial variations of v_p/v_s ratios mainly on a NS profile along strike of the main shock fault plane. On this profile two conspicuous high v_p/v_s areas can be identified above the assumed top of the subducting Nazca plate which is marked in the figure by a grey plane with a dip angle of $\sim 20°$. Comparing these high v_p/v_s areas to any of the previously shown b-value maps it can be noted that the smaller northern area is located around 23.6°S which coincides well with the location of the northern high b-value patch. Around 24°S the area of high v_p/v_s ratios is much larger than in the north and seems to be congruent with the southern high b-value patch or assumed asperity. To draw a conclusion from this correlation, the b-values and v_p/v_s ratios seem to be positively correlated in such a way that the patches of high b-values on the fault plane are congruent with high v_p/v_s ratios either on or above the fault plane in the upper crust. Taking into account the correlation of high b-value patches with the locations of the batholiths it can be hypothesized that high post-seismic v_p/v_s ratios have some relation with the batholitic structures in the upper crust.

A plausible interpretation for this observation could be an increase in crack density through shattering of the medium in the high moment release areas which are identical with the high b-value patches, caused by the interaction of the rupture front with the material of higher density. This shattering of the medium by high moment release takes place during main shock rupture propagation, resulting in a high crack density at the corresponding sites on the fault plane. In addition more aftershocks with small magnitudes will frequently occur on these sites and continue to contribute to the crack density increase. Also high b-values can be found where crack densities are high and events of small magnitudes are more frequent than high magnitudes. This would connect the high b-values with high v_p/v_s ratios, assuming increasing crack density as a cause for both. *Husen & Kissling* (2001) suggest post-seismic fluid flow resulting from their study of temporal changes in v_p/v_s ratios in the Antofagasta region. They see an evolution in time from low v_p/v_s ratios two weeks after the mainshock to high v_p/v_s ratios six weeks after the earthquake. This

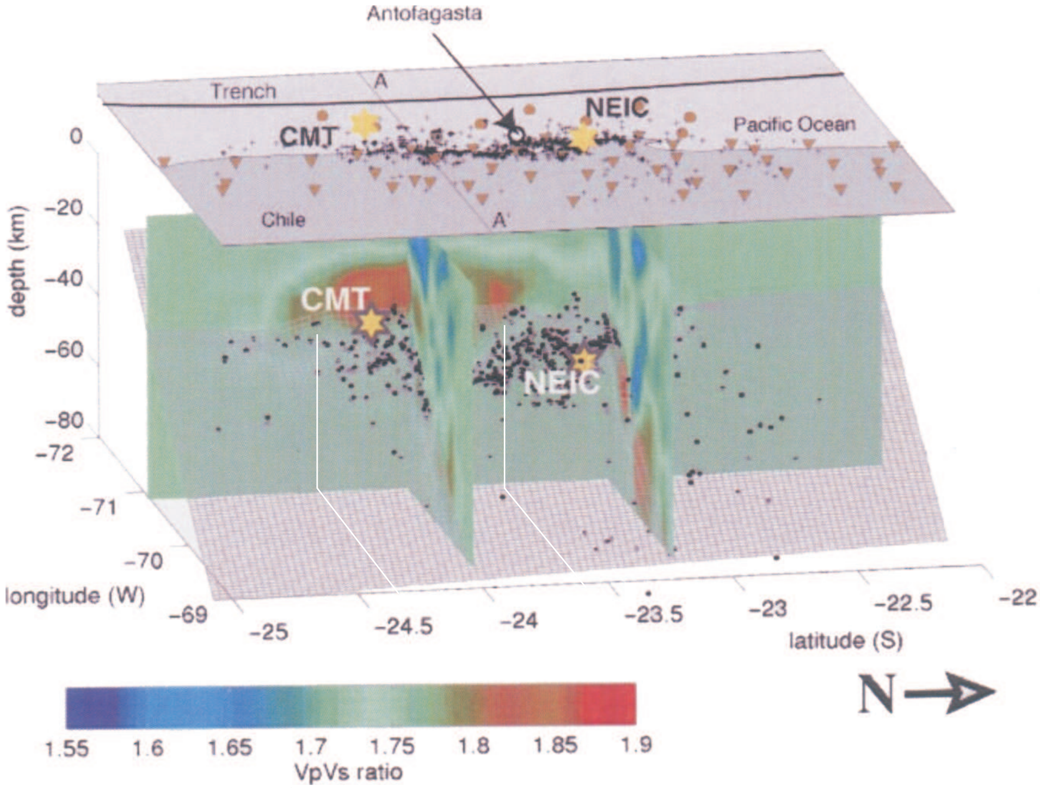

Figure 3.27: Distribution of v_p/v_s ratios in the Antofagasta subduction zone derived from the aftershock sequence of the 1995 event (*Husen & Kissling*, 2001). Note the two pronounced high v_p/v_s areas on a NS profile just above the interface, which coincide well with the high b-value patches in Fig. 3.20. The subducting Nazca plate is marked by a grey grid surface, dipping approximately 20°. The white lines help to attribute the correct latitude to the areas.

development mainly takes place in the overriding crust above the interface, but is obviously connected to the seismogenic zone. So the conclusions of *Husen & Kissling* (2001) should support the correlation found here, as captured fluids of the subducting slab might ascend more easily through strongly fractured material. The cracks or fractures caused by the main shock rupture could make the medium more permeable at first for to start fluid ascend. Fluid intrusion afterwards could serve again as a trigger for new cracks and fractures. Such fluid triggered aftershocks are also suggested by *Shapiro et al.* (2003). The authors propose a diffusion-like relaxation of a pore pressure perturbation in the fractured rocks along the subduction plane as a component of the triggering mechanism for aftershocks. Large CLVD components of summed moment tensors of thrust type aftershocks were found on the segment of the fault plane which hosts the proposed asperities or high b-value patches (see Chapter 5). Taking these large CLVD's as first indicators for fluid driven crack opening, this could be a further support for the discussed models of fluid intrusion.

3.3.5 Concluding hypothesis

Summarizing the results from the correlations of mapped parameters on the Antofagasta fault plane:

The positive correlation of the STF to the b-value map assigns high b-values in this aftershock sequence to main shock high moment release. This is particularly interesting as the correlation links co- with post-seismological observations. According to the classical asperity model (see also Chapter 4), areas of high main shock moment release are called asperities.

Correlating the isostatic residual anomalies to the b-values links the proposed asperity structures to the high density bodies of the uplifted batholiths in the Antofagasta region. This implies that the asperity structures obviously have a higher density than the surrounding material. The hypothesis for the generation of the asperities suggests that these dense bodies resist the contineous motion of the converging plates by inter-locking the upper crust with the downgoing oceanic slab, accumulating stress in the area of the seismogenic zone in the interface.

The suggestion that the high b-value patches also give the size of the asperities is supported by the radiated seismic energy distribution derived from the aftershocks. Linear features of high seismic energy are congruent with the outer limits of the proposed asperities. Furthermore the congruence of high aftershock E_s with low b-value areas confirms the transition zones of increased post-seismic stress between asperities and on adjacent areas to the fault plane.

Considering that high moment release is identical with large slip values leads to the assumption that the high b-values in these areas result from a high degree of damage of the material at these sites. A high degree of damage will express itself in a larger number of relatively small cracks and fractures and thus in a high crack density. This proposed mechanism is confirmed by the positive correlation of the high b-value patches with areas of high v_p/v_s ratios.

Conclusive statements on the b-value distribution:

Including all results of Chapter 3 the following general remark can be made: The identified "kinks" in the GR relation for the entire part of the aftershock sequence (Fig. 3.10) constituting the b-value map are significant in such a way that they seem to represent sub-processes in the aftershock activity connected to the two pronounced asperity structures. This is evidenced by the individual GR relations for the earthquake populations responsible for highest and lowest b-values apparent in the map. It can be noted that these individual GR relations follow very well a power law behaviour in contrast to the overall relation. One could speculate, that the number of "kinks" in the GR relation for the entire set is related to the number of sub-processes in the aftershock sequence where the definition for sub-process would be the aftershock decay activity of the events belonging either to the high b-value patches or to the transition zones of low b-values.

In the introductory sections of this chapter it has been suggested that b depends primarily on the local stress field and secondarily on material properties. The observations made by investigating this aftershock sequence show, that both dependences seem to be relevant for the spatial b-value distribution. According to the correlations of high b-values in the map to the batholiths and high moment releases it is suggested, that b reflects the degree of damage in these areas. As a certain degree of damage obviously results from micro-structural conditions like grain sizes and friction angles, it can be called a material property. Regarding the temporal development of an asperity during one seismic cycle, it can be expected that relevance of either stress or material property having more influence on b will change with time.

From the correlation of the b-value map to the different parameters described previously it can be further evidenced that

- the spatial distribution of aftershock b-values is capable to map out fault plane structures which can be defined as asperities, influencing main shock rupture propagation,
- that the precision of the achieved b-value map is high enough to resolve the size of the asperity structures, enabeling us to estimate source parameters like seismic moment, stress drop, slip and apparent stress on these sites (see Chapter 4),
- the local b-value variations on the fault plane have a physical meaning, which is tied to the degree of damage distribution in the respective volumes concerned.

Conclusive statements on the nature of the asperities:

Regarding the physical properties of the asperities it can be stated that they should be constituted of material of higher density than their surrounding environment according to the correlation between areas of high b-values, the isostatic residual anomalies, and the locations of the batholiths in the Antofagasta region.

The suggested interaction of the dense batholiths with the interface and the subducting plate creates the local stress field situation which loads the asperity transferring it to a highly stressed area prior to the main shock (see further discussion on the final model in Chapter 6). After the main shock the asperities are changing to areas where stresses are released showing high slip values, a higher degree of damage and consequently high crack densities (see also Chapter 6 for detailed discussion of the evolution of asperities during the seismic cycle).

4. Application of an Asperity Model

In the previous chapter the results of the b-value mapping indicates the heterogeneity on the fault plane, revealing fault plane structures which should be tested for their relevance to the rupture mechanism. The aim of this chapter is to apply a common asperity model to these obtained fault plane structures assuming that the areas or "patches" of high b-values and high moment release are asperities. The following parameters will be determined: size S_A, seismic moment M_{oA}, average slip $\overline{D}_A$ and stress drop $\Delta\sigma_A$ of each asperity and the respective values for the "overall" rupture plane.

4.1 General outlines of the model

The permanent descent of the Nazca-Plate beneath Southern America is applying stress to the seismogenic zone of the subduction environment of Northern Chile (Fig. 4.1).

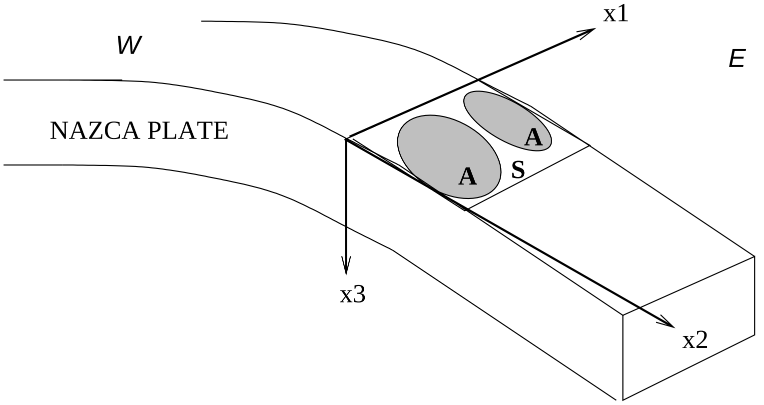

Figure 4.1: Sketch of the Antofagasta fault plane and the simplified tectonic stress regime. According to the cartesian coordinate system in the sketch σ_{33} is the stress acting normal to the fault plane and σ_{31} and σ_{32} are acting in plane and are thus the shear stresses. The letter A denotes the asperities and S the surface of the fault plane area.

For the model discussed here it is assumed that large parts of the seismogenic zone are reacting on the applied stress by slipping constantly. Within this constantly deforming parts of the seismogenic zone we find "patches" of higher resistance against the general motion caused by structural unconformities or varying material properties. Due to this resistance, stress is build up in the vicinity of these "patches" called asperities. A displacement deficit is created between asperities and surrounding areas during one seismic cycle. During earthquake rupture the asperities are reacting by showing higher moment releases, stress drops and slip values. This is causing a multiple event with a number of subevents corresponding to the number of asperities on the fault plane.

How these heterogeneities in the source area influence stress drop and slip as source parameters was described by *Madariaga* (1979) studying three numerical models. Model a) simulates the case of a "smooth" fault without any heterogeneities, model b) contains asperities in the fault plane area, and model c) includes heterogeneities which brake during mainshock rupture but unbroken areas remain between the unconformities (Fig. 4.2). This last model is called barrier model and simulates the one proposed by *Das & Aki* (1977).

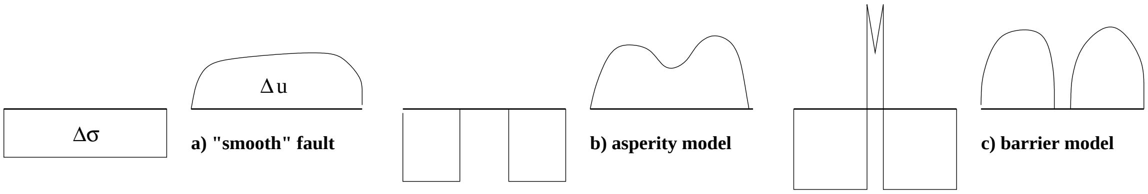

Figure 4.2: From *Madariaga* (1979): stress drop $\Delta\sigma$ and slip Δu after the mainshock for three numerical models simulating a) a smooth fault, b) a fault with two distinct asperities and c) a fault with barriers.

The corresponding far-field radiation of each model shows the influence of asperities or barriers on wave trains *Madariaga* (1979). The far field P and S -waves generated by model b) and c) exhibit double pulses whereas the pulse of model a) is single. The spectra of P and S pulses for the relevant model b) can be seen in Fig. 4.3.

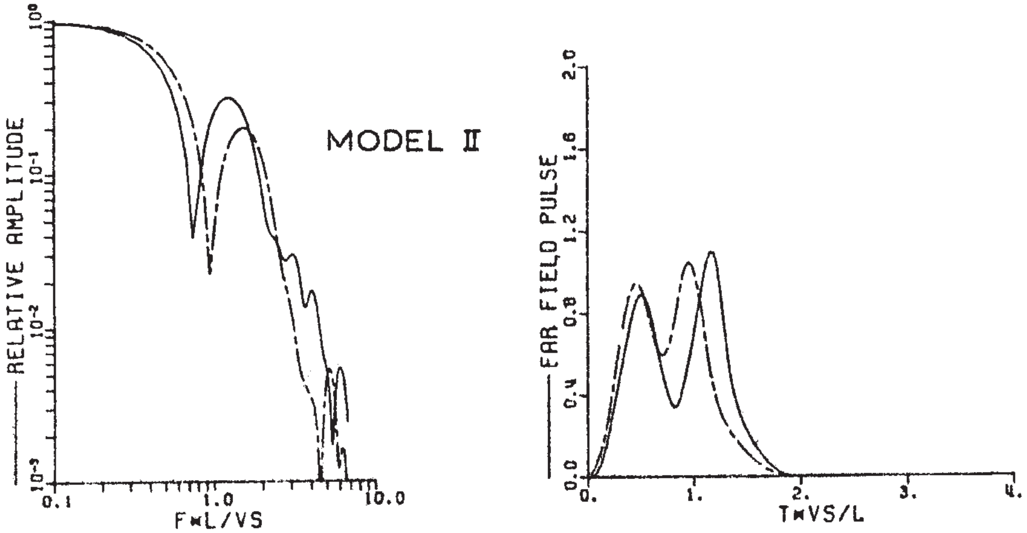

Figure 4.3: Far field radiation as generated by model b) in Fig. 4.2. Solid lines correspond to P-waves, dashed lines to S-waves. From: *Madariaga* (1979).

The displacements corresponding to P and S-waves in the far field are proportional to $\dot{M}(t)$, which is the time derivative or source time function STF of $M(t) = \mu SD(t)$ (*Lay & Wallace*, 1995). Using a simple step funtion as M(t) creates a δ-impulse as $\dot{M}(t)$. Using a ramp function for $M(t)$ considering a rise time τ for the particle motion leads to a boxcar, then $\dot{M}(t) = B(t)$. The area beneath the STF is equivalent to the seismic moment M_o of the entire rupture (Fig. 4.1). The areas beneath certain episodes of the STF correspond to the seismic moments M_{oA} of denoted sub-events of the total rupture process (see also Fig. 4.5).

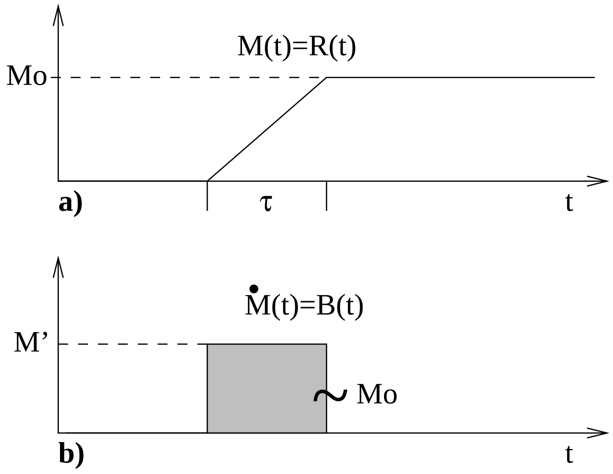

Figure 4.4: From *Lay & Wallace* (1995). a) The moment function as a ramp function $M(t) = R(t)$ with rise time τ. b) The ramp function generates a boxcar in the far field, $\dot{M}(t) = B(t)$.

Following *Burridge & Knopoff* (1964) and *Aki* (1965) the discontinuities in displacement or slip are specified in time and space as $U_2 = B(x_1)B(x_2)R(t)$ where $B(x_j)$ is a boxcar and $R(t)$ the ramp funtion. U_1 and U_3 are zero.

The seismic moment can be written in its general form as

$$M_o = \mu \int_S dSD_o = \mu \overline{D} S \tag{4.1}$$

A seismic moment is defined for each episode or sub-event in the STF of the main shock and is related to distinct areas on the fault plane which in this study are the proposed asperities. Then the above general relation for M_o can also be written as

$$M_{oA} = \mu \int_{S_A} dS_A D_A = \mu \overline{D}_A S_A \tag{4.2}$$

where M_{oA} is the moment released by the rupture of the asperity and S_A and $\overline{D}_A$ are the size and average slip on the asperity.

Once the seismic moments M_{oA} are determined from the source time function for each sub-event and the sizes of the corresponding sub-areas or asperities are taken from the b-value mappings of the fault plane area, the average slip $\overline{D}_A$ can be determined by

$$\overline{D}_A = \frac{M_{oA}}{\mu S_A} \tag{4.3}$$

or by $\overline{D} = \frac{M_o}{\mu S}$ for the average slip on the entire rupture plane respectively.

A more complex parameter is the static stress drop $\Delta\sigma$ as it is known to be very sensitive to the area size and geometry for which $\Delta\sigma$ is calculated. The stress drop is given by $\Delta\sigma = C\mu(\frac{\overline{D}}{L})$ (*Kanamori & Anderson*, 1975). Large differences of the order of magnitudes were found between $\Delta\sigma$ for entire rupture planes of complex earthquakes and $\Delta\sigma_a$ as a local value for sub-event areas or asperities (*Rudnicki & Kanamori*, 1981; *Madariaga*, 1979). Considering this geometry dependence we used the classical formula of *Keilis-Borok* (1959) for a circular crack to determine $\Delta\sigma_a$ on the asperities

$$\Delta\sigma_A = \frac{7}{16}\frac{M_{oA}}{R^3} \tag{4.4}$$

For the calculation of an average value of $\Delta\sigma$ on the entire rupture plane the specific relations for strike slip and dip slip geometry were used (*Starr*, 1928; *Knopoff*, 1958; *Kanamori & Anderson*, 1975):

	Antofagasta
strike slip	$\Delta\sigma = \frac{4}{\pi}\frac{M_o}{w^2L}$
dip slip	$\Delta\sigma = \frac{16}{3\pi}\frac{M_o}{w^2L}$

(4.5)

where w is the width and L is the length of the fault. The shape factor $C = \frac{4}{\pi}$ is valid in case of a burried fault (Antofagasta). $C = \frac{2}{\pi}$ applies for a strike slip fault which has the free surface as upper limit of the fault plane. For Antofagasta both relations , strike slip and dip slip ($\lambda = \mu$ is assumed) were used to constrain the influence of the geometry on the result for $\Delta\sigma$.

4.2 Resulting values for moment, slip and stress drop

The complete STF for the Antofagsta earthquake as calculated by *Delouis* (1996) was taken to determine the total seismic moment M_o for the main shock (see Fig. 4.5). The darkened areas in Fig. 4.5 mark the areas used to derive the seismic moments M_{oA} for the asperities.

The average slip $\overline{D}$ on the entire fault plane is computed using Eq. 4.1 and 4.3, where S is achieved from the spatial distribution of the aftershocks as outlined in Fig. 2.10, Chapter 2. The sizes S_A of the asperities are taken from the mapped high b-value areas in combination with the STF assuming the asperities to be circular sub-faults in the rupture process (Fig. 3.22 Chapter 3). The radii of these sub-faults yield for $R_{A_1} = 14$ km and $R_{A_2} = 21$ km respectively. The average slip $\overline{D}_A$ on each asperity is determined according to Eq. 4.3. The rigidity μ was calculated by $\mu = v_s^2\rho$ obtaining an average value for v_s between 8.5 and 45 km depth from the 1D veloctity model for the Antofagasta region (*Husen*, 1999). The density $\rho = 2.96\frac{g}{cm^3}$ is taken from a density model by *Götze et al.*

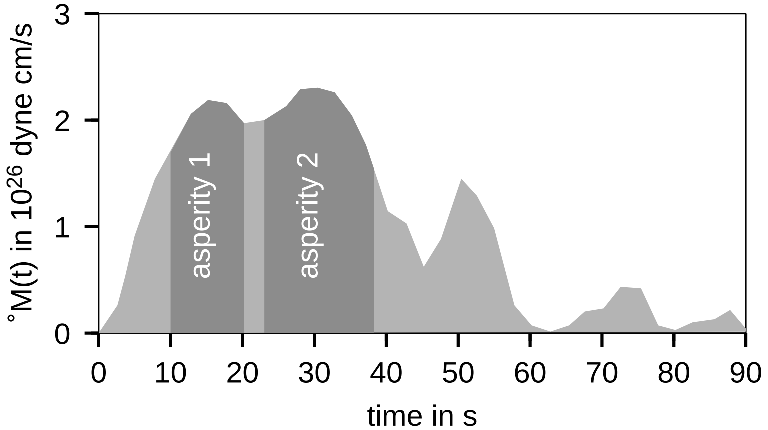

Figure 4.5: The total seismic moment rate, assuming a rupture propagation velocity of 2.8 km/s as calculated by *Delouis* (1996) of the Antofagasta main shock. Darkened areas denote the portions of the STF corresponding to the proposed asperities as identified from the b-value distribution.

Antofagasta	S [km^2]	M_o [10^{20}Nm]	$\Delta\sigma$ [bar]	$\overline{D}$ [m]
total rupture plane	15445	9.3	12	1.3
asperity 1	615	2.1	335	7.4
asperity 2	1385	3.2	151	5.0

Table 4.1: The source parameters fault area S, seismic moment M_o, stress drop $\Delta\sigma$, and average slip $\overline{D}$ for the entire rupture plane and asperity 1 and 2 respectively, calculated by combining STF and b-value map as shown in Fig. 3.22, Chapter 3.

(1994). This leads to a relatively high value of $\mu = 4.61 \text{ x } 10^{10} \frac{N}{m^2}$. All calculated values are listed in Table 4.1.

Table 4.2 is listing the respective parameters E_s (radiated seismic energy), and τ_a (apparent stress). The values were calculated by using the relations

$$E_s = \frac{1}{2}\Delta\sigma\overline{D}S \tag{4.6}$$

from *Kostrov* (1974), and

$$\tau_a = \mu E_s / M_o \tag{4.7}$$

according to *Wyss & Brune* (1968). τ_a is just a re-calculation of the stress drop $\Delta\sigma$ as this parameter is also calculated from the empirical equation 4.4. It is listed in Table 4.2 for completeness.

-	E_s [Nm]	τ_a [MPa]
total	1.2 x 10^{16}	0.6
asperity 1	7.6 x 10^{16}	16.7
asperity 2	5.2 x 10^{16}	7.5

Table 4.2: Radiated seismic energy E_s and apparent stress τ_a as attributed to the total fault plane and the asperities 1 and 2.

4.3 Discussion and interpretation

As mentioned previously, various authors (*Aki et al.*, 1977; *Madariaga*, 1979; *Aki*, 1979; *Rudnicki & Kanamori*, 1981; *Lay & Kanamori*, 1981; *Das & Kostrov*, 1988) found that the introduction of asperities and barriers can help to explain the observed variations in source parameters on fault planes. Most important was the perception that stress drop and slip can have much higher values on small scale asperity structures than for average values on the entire rupture plane. This general finding can be corroborated by the results obtained for the fault plane of the Antofagasta earthquake. The values as listed in Table 4.1 show that the average stress drops $\Delta\sigma_A$ for the asperities are much higher than the average $\Delta\sigma$ for the entire fault plane. The largest slip in Antofagasta occured on asperity 1 reaching more than 7 m. In comparison the average displacement along the fault is 1.3 m.

To evaluate the achieved results for M_o, $\Delta\sigma$ and $\overline{D}$ (entire fault plane) and M_{oA}, $\Delta\sigma_A$, $\overline{D}_A$ (asperities) in the case of the Antofagasta earthquake, results from other authors were reviewed and are listed in Table 4.3.

authors	Seismic Moment	slip	rupture plane	methods used
Dziewonski et.al., 1996	1.2 x 10^{21} Nm	-	-	global network data
Delouis, 1996	1.2 x 10^{21} Nm	2.5 - 3.5 m on 4 sub-areas of the fault plane (northern part)	185 x 90 km^2	inversion of teleseismic data
Ruegg et.al., 1996	a) 9.0 x 10^{20} Nm b) 1.5 x 10^{21} Nm	$\sim$ 5m (average)	180 x 60 km^2	a) VBB body wave modelling (IRIS and GEOSCOPE data) b) geodetic data
Klotz et.al., 1999	1.78 x 10^{21} Nm	$\sim$ 3.2 m down dip (maximum) at 24° S, $\sim$ 1.4 m in strike direction	180 x 60 km^2	GPS data inversion
Ihmle and Ruegg, 1997	1.4 x 10^{21} Nm	a) from GPS data: average 2-4 m at 60-100 km from start of the rupture, b) from joined inversion: 5-6 m at 40 km south of rupture start, 6-7 m at 80-90 km south of rupture start	195 x 75 km^2	GPS data and GPS-Rayleigh wave joined inversion
Carlo et.al., 1999	1.6 x 10^{21} Nm	10 m (maximum) at 80-100 km and 110-140 km south of rupture start	-	spectral inversion of surface waves, directivity analysis
Pritchard et.al., 2002	1.6 x 10^{21} Nm	4 m (maximum) at $\sim$ 24° S	-	joined inversion of GPS and InSAR data

Table 4.3: List of seismic moment, slip and size of rupture plane as determined by various authors using different methods for the Antofagasta earthquake.

The obtained results as given in Table 4.1 are well compatable with the results by *Ruegg et al.* (1996) and *Ihmlé & Ruegg* (1997). *Ruegg et al.* (1996) calculated two values for the seismic moment for the entire event using body wave modelling from VBB data yielding M_o = 9.0 x 10^{20} Nm and M_o = 1.5 x 10^{21} Nm by inverting GPS data. Their first value agrees well to M_o = 9.3 x 10^{20} Nm resulting from the integration of the total SFT by (*Delouis*, 1996). In general the seismic moments obtained from geodetic data are higher than those determined from seismological data. *Ruegg et al.* (1996) argue that this discrepancy is due to a considerable amount of co-seismic moment release at low frequencies. This low frequency radiation is mainly resolved by GPS data whereas seismological data involves more higher frequencies.

An important support for the suggested Antofagasta fault plane structure with two prominent asperities is coming from the results of Ihmlé and Ruegg's (1997) simultaneous inversion of long period surface waves and GPS data using the method of simulated

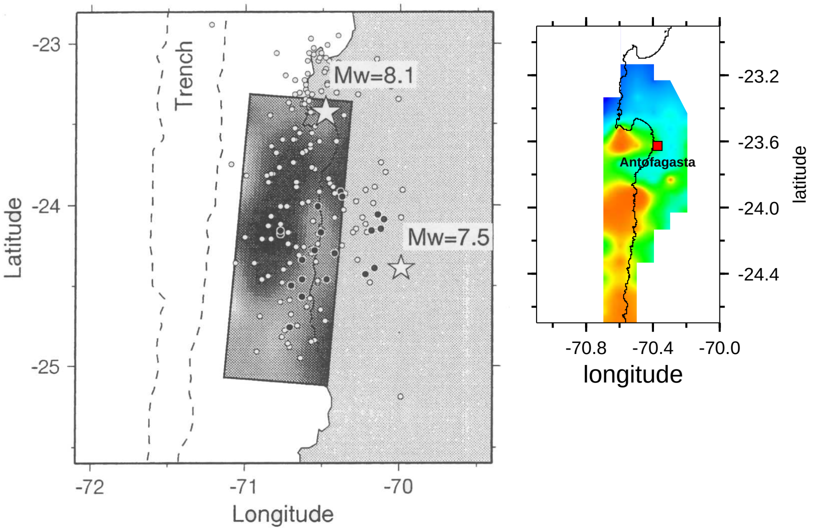

Figure 4.6: Areas of large slip as derived from simultaneous inversion of teleseismic data and GPS data using simulated annealing. From: *Ihmlé & Ruegg* (1997). The structure characterized by two distinct areas of large slip are similar to the fault plane structure as derived from the b-value map (for comparison, see small sketch to the right).

annealing. Their discretization of the fault plane with a grid of 15 x 15 km^2 is very near to the 11 x 11 km^2 grid used for the b-value map. They obtain two areas of large slip on the fault plane of which the northern slightly smaller area is situated 40 km south of the hypocenter exhibiting a maximum slip of 5-6 m and a southern area with a slip maximum of 6-7 m at 80 to 90 km south of the rupture start. This is almost identical with the results found here by combining the b-value distribution and the asperity model. The two areas identified by *Ihmlé & Ruegg* (1997) seem to be shifted southward by approximately 10 km in comparison to the asperity locations found here which could result from averaged rupture velocities used for inversion. Most of the maximum slip values obtained from inversion of geodetic data (see Table 4.3) are smaller than the slip on the asperities given by the asperity model. This might be due to the fact that obviously a large part of the slip occured off shore in front of the coast which is difficult to resolve by geodetic data relying on land based stations (*Pritchard et al.*, 2002).

Fig. 4.7 shows the result for the deformation caused by the Antofagasta earthquake as derived by *Klotz et al.* (1999) and *Xia et al.* (2003) (see also Table 4.3). The deformation vectors are the result of an observation time of 21 months before the 1995 Antofagasta earthquake and three months after the event. Although 21 month of interseismic loading is depicted in this image, the deformation field is clearly dominated by the co-seismic deformation. The arrows demonstrate, that the largest deformation can be found south of Mejillones Peninsula with a culmination around 24°S. This is in accord with the fault plane structure suggested here and the largest slips occurring on the proposed asperities south of Mejillones. The yellow arrows show the residual motions to the best fitting fault slip model from GPS data modeling. The direction of the inter-seismic motion is in accordance to directions of the Nazca plate motion as derived by *Angermann et al.* (1999). Note that the angle of this direction of plate motion is the same as the angle of lineaments formed by aftershocks on Mejillones Peninsula and near Antofagasta, as can be seen in Fig. 5.9, Chapter 5.

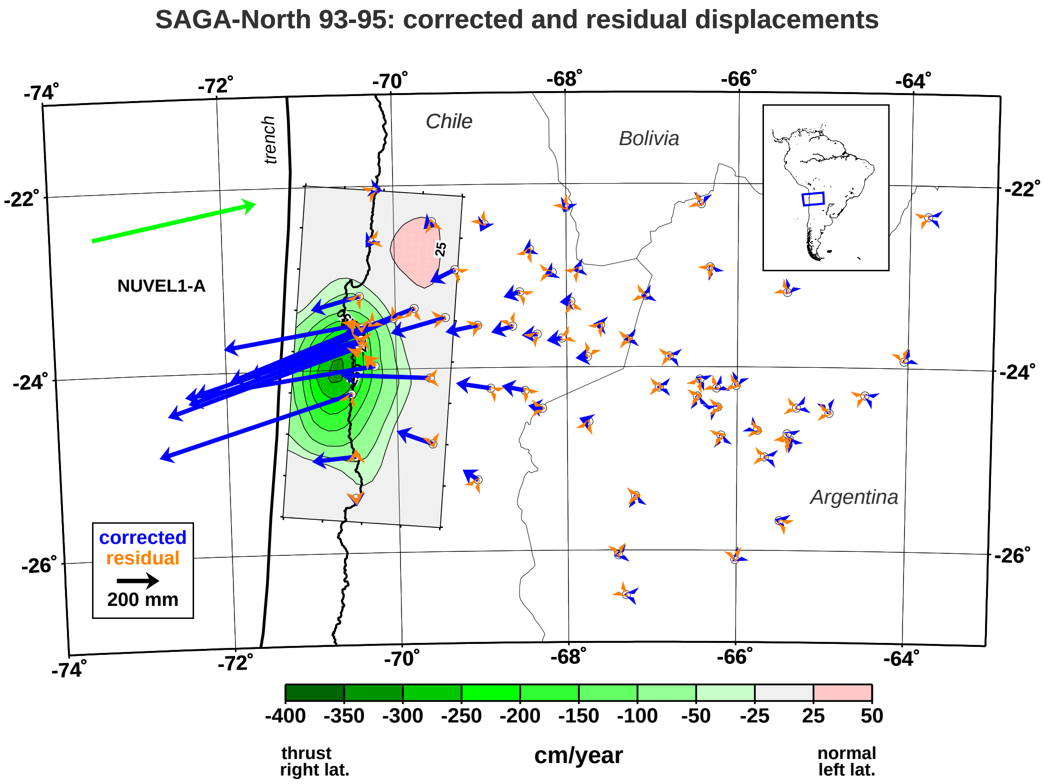
SAGA-North 93-95: corrected and residual displacements

Figure 4.7: Inter-seismic, co-seismic and post-seismic displacement field (green area) in the Atofagasta region as derived from GPS measurements at 215 stations. From: (*Klotz et al.*, 1999). Blue arrows show the corrected displacement at each station site; red arrows give the respective residuals. See text for further explanations.

Assuming a geological slip rate of 6.8cm/yr for the Nazca plate (*Norabuena et al.*, 1999) descending beneath Southern America in an slightly oblique east - west direction and a seismic cycle of $\sim$ 100 years for earthquakes of magnitude 8 in Northern Chile (*Comte et al.*, 1994), a relative displacement of 6.8 m would be achieved during a period of tectonic loading. Supposing that a large earthquake at the end of a seismic cycle recovers the stress accumulation due to the relative displacement the resulting slip on the fault plane should be in accordance to the geological slip value. The maximum values of slip on the Antofagasta fault plane using the asperity model (5 - 7 m) is in fairly good agreement with the expected 6.8 m of displacement due to the geological slip rate.

Papageorgiou & Aki (1983) and *Aki* (1984) constructed a specific barrier model described by five parameters as fault length, width, rupture velocity, maximum slip, and barrier interval where they achieve a linear relation between barrier interval and maximum slip using a circular crack model for the estimation of the local stress drop. In search for additional evaluation for the asperity distribution found in the *b*-value map and the stress drop $\Delta\sigma_A$ for asperity 1 and 2, the distance of $\sim$ 15 km between asperity 1 and 2 (set equal to the barrier interval in Aki's model) and a mean value of 6.2 m of maximum slip

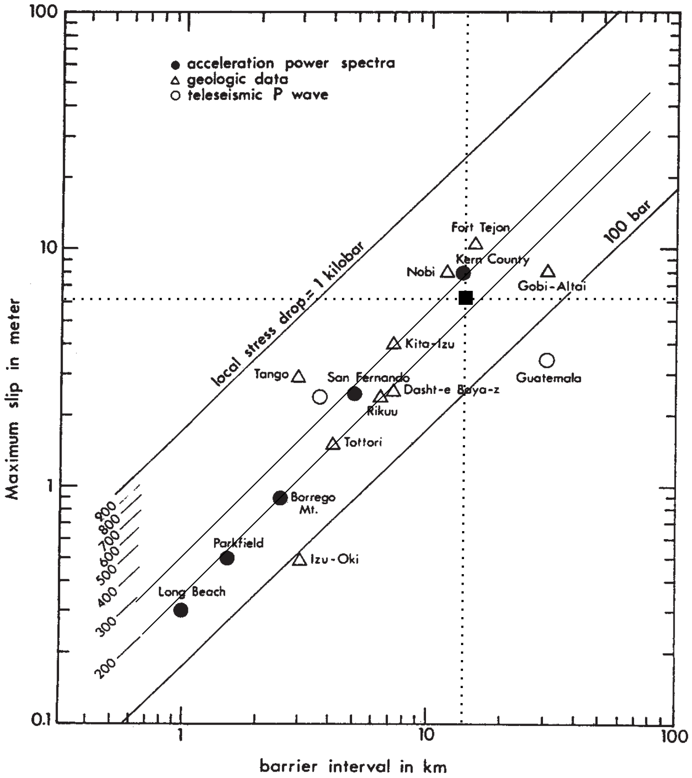

Figure 4.8: The diagram relates the barrier interval to the maximum slip of a fault (taken from: (*Aki*, 1984)). The diagonals give the attributed stress drop values for different intervals and slips of several wellknown earthquakes. The small square marks the corresponding value for the Antofagasta fault plane. See text for further explanation.

were inserted into the diagram taken from *Aki* (1984). According to the diagram this leads to a stress drop of $\sim$ 250 bars which is only slightly larger than a mean value of 243 bars for the stress drop found on asperity 1 and 2.

Another corroboration of the asperity sizes on the Antofagasta fault plane is coming from the spectrogram of a vertical component velocity record at station VNDA (Wright Valley, Bull Pass, Antarctica) realized by *Ihmlé & Madariaga* (1996). In this spectrogram higher amplitudes are attributed to two distinct areas of frequencies between 0.11 Hz and 0.16 Hz at 10 to 30 s and 0.05 Hz and 0.17 Hz at 50 to 65 s respectively. As the rupture propagation of the Antofagasta event is known to be unilateral these areas of higher P-wave amplitudes might be linked to the asperities as a cause for the excitation. Assuming a rupture velocity $v_r = 3.0$ s (*Ihmlé & Madariaga*, 1996) and a mean value of frequencies of 0.14 Hz and 0.17 Hz respectively this leads to spatial dimensions of $\sim$21 km and $\sim$27 km. These values reflect relatively well the dimensions of the two asperities having estimated diameters of $\sim$28 km and $\sim$42 km.

Recently a number of authors has developed asperity models to find scaling laws for source parameters of small repeating earthquakes on sites of the San Andreas Fault (California) (*Nadeau & Johnson*, 1998; *Sammis et al.*, 1999; *Sammis & Rice*, 2001; *Johnson & Nadeau*, 2002; *Chen & Sammis*, 2003). *Nadeau & Johnson* (1998) were able to identify the asperities associated with the sequences of the small events and found that the smallest asperity had linear dimensions of 0.5 m and a slip of 2cm. This implies stress drops as large as 20000 bars (*Nadeau & Johnson*, 1998; *Sammis et al.*, 1999). Although the generalization of scales is difficult, an attempt was made here to link the presented results gained from the Antofagasta earthquake to the previously mentioned values for the small asperity by using the relation $\Delta\sigma \propto A^{-0.3}$ (*Nadeau & Johnson*, 1998) (Fig. 4.9). The slip value determined for the main asperity of the 1997 Cariaco earthquake, northeast Venezuela (see end of Chapter 6), was also considered in the diagram to have an additional data point. Despite the fact that there are only a view datapoints and dispersion is obvious, the solid line having a slope of -0.3 supports the general trend of the relation and thus the hypothesis that stress drop on asperities decreases with increasing slip area and moment.

Summerizing the previous observations and results we can draw the conclusion that seismic moment, stress drop and slip are heterogeneously distributed on the Antofagasta fault plane. Certain areas are showing much higher values of the source parameters than the entire fault planes. This is well adopted with the general hypothesis that the higher order structures or the distribution of intrinsic physical properties on a fault can lead to strongly varying source parameters. The values for the sizes of the assumed asperities displaying the heterogeneity and the values for stress drop and slip are lying well within the values cited from other publications. In this context it is interesting to note that according to the applicability of an asperity model as described here the spatial *b*-value distribution derived from aftershock sequences obviously reflects a situation prior to the main shock.

According to the asperity model discussed here, the largest slip of up to 7m is released

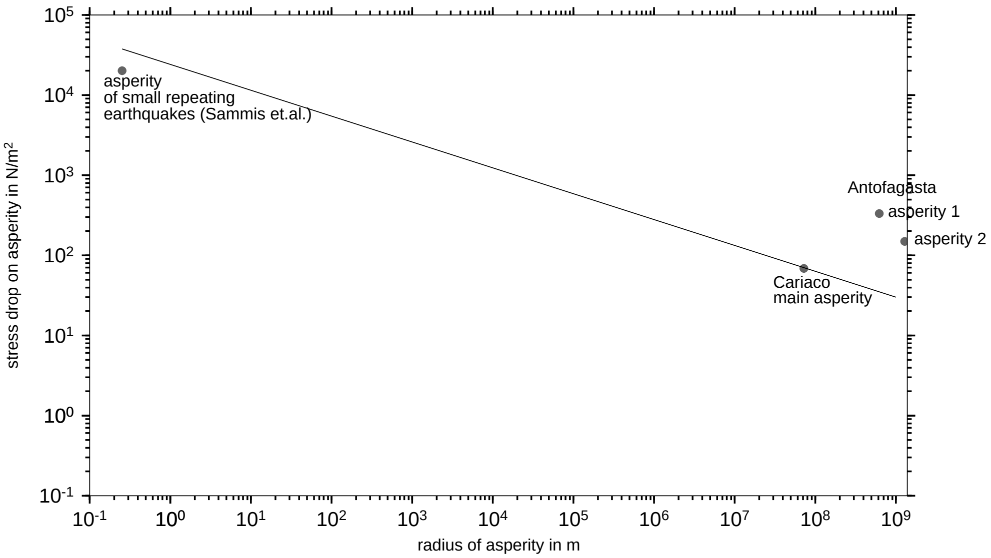

Figure 4.9: The graph is showing the scaling relation between stress drop and asperity size as found by *Nadeau & Johnson* (1998) for small repeating earthquakes (value at the upper end of the graph) and the values from the Antofagasta and Cariaco earthquakes (lower end of the graph).

on the asperity patches. The consequence must be a large deficit between asperity patches and surrounding material which could be recovered either in a late coseismic phase, a postseismic creep or during the longterm interseismic phase. Assuming that the model discussed in chapter 3 resulting from the correlation of the b-values with the teleseismic STF, the IRF anomalies, the aftershock E_s and the seismic v_p/v_s ratios is valid, part of the slip deficit must develop during interseismic phases as the asperities accumulate stress prior to a large earthquake. Simultaneously the weaker material between asperities is forming creeping sections on the fault plane which follow the convergent plate motion in a ductile manner. However, a smaller slip deficit between plate movement and creeping sections must also be expected as it is observed that the rupture process of the Antofagasta earthquake starts approximately 10 to 20 km north of the first asperity which would correspond to a location in a creeping section. The record of a VBB station at Iquique north of Antofagasta shows a slow start of the Antofagasta earthquake (*Ruegg et al.*, 1996) which would be consistent to the start of the rupture process in a creeping section of the seismogenic zone.

5. Aftershock Source Mechanisms

Structural information about the main shock fault plane infered from aftershock focal mechanism solutions and their moment tensor transformations will be discussed in this chapter. It is found that the character of the moment tensors changes from the northern to the southern part of the fault plane. A deviation of the mechanism from pure shear is indicated for the southern part which hosts the two asperities identified in the *b*-value map. Furthermore the aftershock fault-plane solutions disclose the segmentation of the mainshock fault plane and reveal some details on faulting processes in the interface zone.

5.1 Moment tensor decomposition and its relation to the complexity of a fault plane, theory

Moment tensors are an option to describe the permanent inelastic strain produced by an earthquake. They offer the possibility to include non-double-couple (NDC) source mechanisms due to complex fault structures besides the usual double-couple mechanism due to shear stresses released on planar fault surfaces (*Frohlich & Apperson*, 1992; *Frohlich*, 1994; *Jost & Herrmann*, 1989; *Kagan & Knopoff*, 1985; *Knopoff & Randall*, 1970; *Madariaga*, 1983). Each of the six independent moment tensor elements M_{ij} corresponds to a force couple pointing in direction i and holding on the axis defined by j. Conventional fault-plane solutions (*fps*) can be written in the principle axes system as a moment tensor in such a way that their double couple is expressed by two moment tensor elements

$$\mathbf{M} = M_o \cdot \begin{pmatrix} 1 & 0 & 0 \\ 0 & -1 & 0 \\ 0 & 0 & 0 \end{pmatrix} \quad or \;\; \mathbf{M} = M_o \cdot diag[1, -1, 0] \tag{5.1}$$

This represents a deviatoric, traceless, and symmetric moment tensor, expressing a strike slip event. To realise the transformation of an *fps* to a moment tensor representation, the scalar seismic moment of the event has to be obtained. For this purpose the relation of moment magnitude scale by *Kanamori* (1977) can be used:

$$M_w = \frac{2}{3} log(M_o) - 10.7 \tag{5.2}$$

Assuming a population of N earthquakes in an area S, the individual moment tensors

$\mathbf{M_1}, \mathbf{M_2}, \mathbf{M_3}, ..., \mathbf{M_N}$ can get summed simply by adding up all tensor elements, $\mathbf{M_{sum}} = \mathbf{M_1} + \mathbf{M_2} + \mathbf{M_3} + ... + \mathbf{M_N}$ (*Frohlich & Apperson*, 1992)

$$\sum_{n=1}^{N} \mathbf{M_n} = \mathbf{M_{sum}} \tag{5.3}$$

Once the individual moment tensors of the N earthquakes are summed, the resulting moment tensor $\mathbf{M_{sum}}$ will be transformed by rotation into the principle tension (T), pressure (P), and null (B) axis. If $\mathbf{R_{ij}} = cos_{ij}$ is defined as the direction cosines between the initial and resulting set of axes the general procedure for rotation of the moment tensor $\mathbf{M_{sum}}$ can be described by

$$\mathbf{M'^{sum}_{jk}} = R_{jl}\, \mathbf{M^{sum}_{li}}\, \mathbf{R_{ik}} \tag{5.4}$$

where $\mathbf{R_{il}}$ is the rotation matrix and $\mathbf{R_{jk}}$ its transpose. So generally a moment tensor can get transformed by summation or rotation. Considering again a population of earthquakes, the total seismic moment tensor $\mathbf{M_{sum}}$ composed of the N earthquakes should be the consequence of both operations (*Kagan & Knopoff*, 1985). All moment tensors of the N earthquakes of the population are deviatoric and thus their traces are zero, $tr\mathbf{M_n} = 0$. Consequently the trace of $\mathbf{M_{sum}}$ has to be zero, $tr\mathbf{M_{sum}} = 0$. The determinant of each of the N earthquakes is also zero, $det\mathbf{M_n} = 0$, but the determinant of the summed tensor does not need to be zero, thus can be $det\mathbf{M_{sum}} \neq 0$. This implies that the summed moment tensor will be deviatoric as the initial tensors are but can involve another component besides pure double couple. This component is called the compensated linear vector dipole (CLVD) which characterizes a source with a uniform inward or outward motion on one plane and shortening or extension normal to this plane (*Randell & Knopoff*, 1970), (*Frohlich & Apperson*, 1992). This means that the CLVD has one dipole of strength 2 and two dipoles of unit strength (*Lay & Wallace*, 1995) and thus can be written as

$$\mathbf{M} = 3^{-1/2} \cdot M_o \begin{pmatrix} 2 & 0 & 0 \\ 0 & -1 & 0 \\ 0 & 0 & -1 \end{pmatrix} \quad or \quad \mathbf{M} = 3^{-1/2} \cdot M_o \cdot diag\,[2, -1, -1] \tag{5.5}$$

(*Knopoff & Randall*, 1970; *Kagan & Knopoff*, 1985). The physical meaning of the three types of source mechanisms which can be represented as moment tensors are explained again in Fig. 5.1, showing the most important features for each mechanism. That is the non-zero trace for the isotropic moment tensor, the zero trace and zero determinant for the double couple and the zero trace and non-zero determinant for the CLVD.

Where DC sources describe pure shear on planar fault planes, CLVD mechanisms are often observed when rupture processes get more complex (*Kubas & Sipkin*, 1987; *Kuge &*

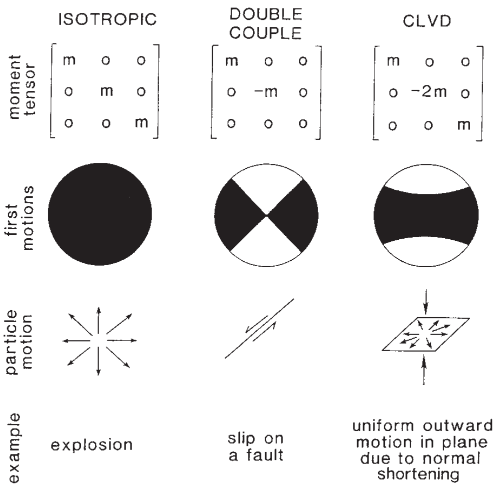

Figure 5.1: Three types of earthquake mechanisms and their equivalent representations as moment tensors. See text for further explanation. From: *Apperson* (1991).

Kawakatsu, 1993; *Julian et al.*, 1997; *Miller et al.*, 1998; *Vavryčuk*, 2001). To investigate the state of deformational complexity expressed by the arrangement of *fps* of a population of earthquakes, the summed moment tensor $\mathbf{M_{sum}}$ can be decomposed to identify the amount of DC and NDC components. Generally any moment tensor can be decomposed into a variety of source mechanism combinations such as the decomposition into three equivalent vector dipoles or into terms of a major and minor double couple. The decomposition used in this investigation for $\mathbf{M_{sum}}$ has got an isotropic part, a double couple and a CLVD and can be expressed such as (*Lay & Wallace*, 1995):

$$\mathbf{M_{sum}} = \begin{pmatrix} M_T & 0 & 0 \\ 0 & M_B & 0 \\ 0 & 0 & M_P \end{pmatrix} = \frac{1}{3} \begin{pmatrix} tr\mathbf{M} & 0 & 0 \\ 0 & tr\mathbf{M} & 0 \\ 0 & 0 & tr\mathbf{M} \end{pmatrix} \tag{5.6}$$

$$+ (1 - 2f_{clvd}) \begin{pmatrix} 0 & 0 & 0 \\ 0 & -M_P & 0 \\ 0 & 0 & M_P \end{pmatrix} + f_{clvd} \begin{pmatrix} -M_P & 0 & 0 \\ 0 & -M_P & 0 \\ 0 & 0 & 2M_P \end{pmatrix}$$

where M_T, M_B and M_P are the largest, intermediate and smallest principle moments respectively. The f_{clvd} is called the CLVD ratio and is a measure of the size of the CLVD component relative to the douple couple. For pure DC, $f_{clvd} = 0$, and for a pure CLVD, $f_{clvd} = 0.5$ or -0.5 respectively (see also Fig. 5.1) (*Giardini*, 1984; *Frohlich & Apperson*, 1992). Alternatively the f_{clvd} can be expressed as percentage of CLVD where f_{clvd} has to be multiplied by 200. The percentage of DC is $(1 - 2f_{clvd}) \cdot 100$ (*Jost & Herrmann*, 1989). The f_{clvd} can be expressed as

$$f_{clvd} = \frac{|M_B|}{max(|M_T|, |M_P|)} \tag{5.7}$$

which means that f_{clvd} is the ratio of the principle moments or eigenvalues having the smallest and largest absolute values (*Giardini*, 1984; *Frohlich & Apperson*, 1992). If the f_{clvd} is positive the maximum absolute eigenvalue is the tensional principle axis (T-axis). When the f_{clvd} is getting negative the maximum absolute eigenvalue is the compressional principle axis (P-axis) (*Kuge & Kawakatsu*, 1993).

A statistical method to determine the similarity of earthquake mechanisms in an area can be achieved by calculating the seismic consistency factor C_s which is defined by

$$C_s = \frac{M_o sum}{\sum_{n=1}^{N} M_{on}} \tag{5.8}$$

which is the division of the scalar moment of $\mathbf{M_{sum}}$ by the sum of scalar moments of N tensors contributing to $\mathbf{M_{sum}}$ (*Brune*, 1968; *Frohlich & Apperson*, 1992). C_s is ranging from 0 to 1 depending on the degree of similarity of the summed mechanisms. Fig. 5.1 gives a graphical explanation of f_{clvd} and C_s.

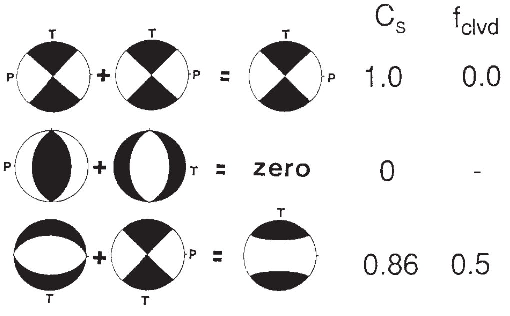

Figure 5.2: Examples for C_s, seismic consistency, and f_{clvd}, CLVD ratio, for different tensor summations. From: *Frohlich & Apperson* (1992).

The possibility to sum up moment tensors of earthquakes in a coherent seismogenic region and the fact that the summation is proportional to the average strain tensor as established by *Kostrov* (1974), leads to a qualitative estimation of how much deformation in the region is due to seismic activity:

$$\varepsilon_{\mathbf{ij}} = \frac{1}{2\mu V} M_{ij} \tag{5.9}$$

$$\varepsilon_{\mathbf{ij}} = \frac{1}{2\mu V} \sum_{n=1}^{N} M_{on} = \frac{1}{2\mu V} \mathbf{M_{sum}} \tag{5.10}$$

where μ is an average value for the rigidity and V is the volume defined by the hypocentres of the summed earthquakes (*Kostrov*, 1974; *Frohlich & Apperson*, 1992). If the coherent seismogenic region to be investigated can be reduced to a two dimensional plane, then the average deformation can be written as:

mechanism	total number	percent	mean M_L	M_L max.
thrust	161	54.6	2.2	4.7
dip	68	23.0	2.1	4.7
strike	39	13.2	2.4	3.8
normal	27	9.2	2.2	3.9

Table 5.1: List of the four mechanism groups found within the available aftershock focal mechanism solutions. Some general information is given regarding each group.

$$\varepsilon_{\mathbf{ij}} = \frac{1}{\mu S} \sum_{n=1}^{N} M_{on} = \frac{1}{\mu S}\, \mathbf{M_{sum}} \tag{5.11}$$

where S is the area on which the earthquakes occur. The summtion of moment tensors has been used by various authors to compare it to the total deformation in a region obtained by tectonic, geologic or geodetic studies (*Brune*, 1968; *Jackson & McKenzie*, 1988; *Holt et al.*, 1991). Theoretically, if the moment tensors of all aftershocks of one sequence would be known, the deformation due to the aftershocks could be compared to the deformation produced by the main shock of a large earthquake. Unfortunately in reality only a relatively small number of aftershock *fps* or moment tensors are available, mostly due to the lack of good quality polarity readings.

5.2 Source mechanisms of the Antofagasta aftershock sequence

5.2.1 General constraints from focal mechanisms

Focal mechanism solutions for 295 aftershock events were obtained from the Antofagasta data set using the software code FPFIT (*Reasenberg & Oppenheimer*, 1985) as implemented in the GIANT software (*Rietbrock & Scherbaum*, 1998). The calculation itself is based on P-wave first arrival polarity readings and a solution was accepted if at least 15 readings were available and a single solution for the best fit was given. This high quality standard led to well and unambigiously constrained fault plane solutions. The resulting solutions were sub-devided into four mechanism catagories, namely into a group of thrusts, dip slips, strike slips and normal faults respectively. This was done according to the criteria for each catagory as defined by *Zoback* (1992). The only exception is the dip slip group. This mechanism actually belongs to the catagory of unclassified *fps*, but as vertical uplift (dip at 90°) seemed to occur quite frequently (second strongest group, see Table 5.1 below), the aftershocks showing this mechanism were put in a separate catagory. Table 5.1 is giving a brief overview about the number of solutions in the different catagories, percentage of the catagory to the total number of calculated solutions, the mean magnitude and largest magnitude registered in each catagory respectively.

Figure 5.3 a) - d) shows how the calculated focal mechanisms are spatially distributed. A first visual evaluation mediates the impression that the mechanisms at the northern end of the fault plane on Mejillones Peninsula are more uniformly oriented than the mechanisms of events south of Mejillones Peninsula. The clear lack of events in the dip slip catagory at ∼ 23.52° S (Fig. 5.3 b) was taken as a reference for the boundary between northern and southern part of the fault plane at which segmenation could have taken place (see also Fig. 5.9). The well oriented part north of this boundary governs the very small northern section of the fault plane plus the adjacent transition zone on Mejillones Peninsula end governs only a very small part of the rupture plane underneath the Mejillones Peninsula. The small northern section of the fault plane is attributed to the first 10 seconds of rise time in the STF (Fig. 4.5, Chapter 4). The proposed asperities thus are located on the remaining southern part of the fault plane of about 180 km extent (see also Fig. 3.20, Chapter 3, for additional information).

Although thrust focal mechanisms are present on the entire fault plane, they seem to be most abundant in the area of Mejillones Peninsula. When plotted in a different scale (Fig. 5.9 b), the thrust mechanisms align on a garland-like structure which might be congruent with fault strands of the Atacama fault system. The dip slip mechaninsms cluster in two patches on the fault plane separated by the described gap and are more abundant on the southern part. This observation is in accord with results from *Delouis et al.* (1997), saying that the rupture started as a pure thrust event in the north, developing an additional component of normal faulting towards the end of the rupture in the south. As the dip slip mechanism is a special type of normal faulting, this general rupture behaviour in the south might be reflected also by the concentration of dip slip aftershocks in this area. Examining more closely the strike slips, there seems to be evidence for segmentation of the fault plane.

In Figure 5.4 Ia) the northern dip slip group exhibits several events at its southern limit with nearly the same orientation striking NNW-SSE assuming that the vertical nodal planes are active. For some events the strikes seem to rotate somewhat to the west, two events are oriented NNE-SSW. The strikes found for the focal mechanisms align well with fault systems found in this area consisting of parallel sub-faults having orientations NNW-SSE and NNE-SSW. Also purely N-S trending faults can be found on Mejillones Peninsula and dip slip mechanisms showing the same strike direction. What all dip slips except two in this group (Fig. 5.4 Ia) have in common is the uplift of the eastern block and the lowering of the western block (see red symbols for arrow tail and arrow peak in Fig. 5.4 Ia). In attempt to interpret this finding it is supposed, that these events are related to the upper plate which is moving westward and upward in a relative manner during the rupture process (see small scheme in Fig. 5.4 I). Fresh scarps reported by *Delouis et al.* (1997) and *Delouis et al.* (1998) from a field campaign after the Antofagasta main shock, serve as an evidence for vertical uplift in the area as proposed by the dip slip mechanisms.

The strike slip mechanisms (Fig. 5.4 II) comprise several remarkable groups of events as for instance the elongated cluster on Mejillones Peninsula (Fig. 5.4 IIa). This group is composed of 10 almost identical strike slip events (except the event further to the east) with their nodal planes trending NNW-SSE and WSW-ENE. The east-west elongation of the cluster suggests that the events occur on an east-west oriented feature which is assumed to be the northern boundary of the first segment of the fault plane seperating the actual slipping part from the remaining non-slipping part beneath Mejillones Peninsula.

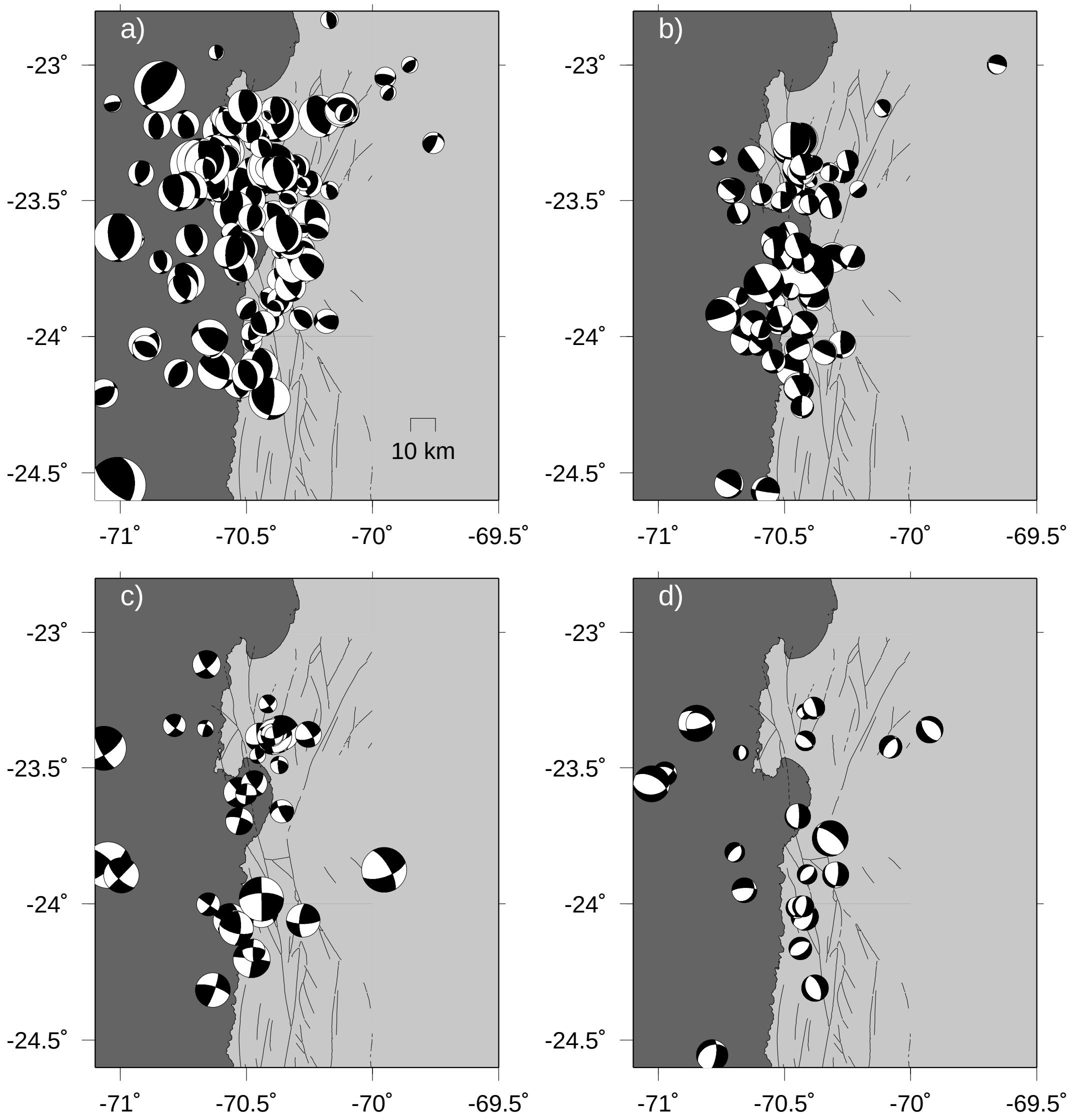

Figure 5.3: The 295 focal mechanisms determined from aftershocks are catagorized in a) thrust, b) dip slip, c) strike slip and d) normal fault events.

This leads to the suggestion that the east-west trending nodal plane of the strike slip mechanisms is active. The group of five events south of Mejillones Peninsula are located in the area of the first asperity. These events do not show any coherent orientation. The group of events further down to the south, marked by a red rectangle in Fig. 5.4 II and shown in Fig. 5.4 IIb) are also quite coherently oriented in opposed symmetry to the group in the north leading to the suggestion, that the events line out the southern border of the first fault plane segment. The red dashed line in Fig. 5.4 II is the proposed southern limit of the segment as in both catagories of dip slip and strike slip mechanisms events aline well along this feature. Thus the suggested segment incorporates the two asperities identified earlier. A third segment reaching further down to the south cannot be resolved with the data. This is due to the lack of registered events in this area or to the proposed change in

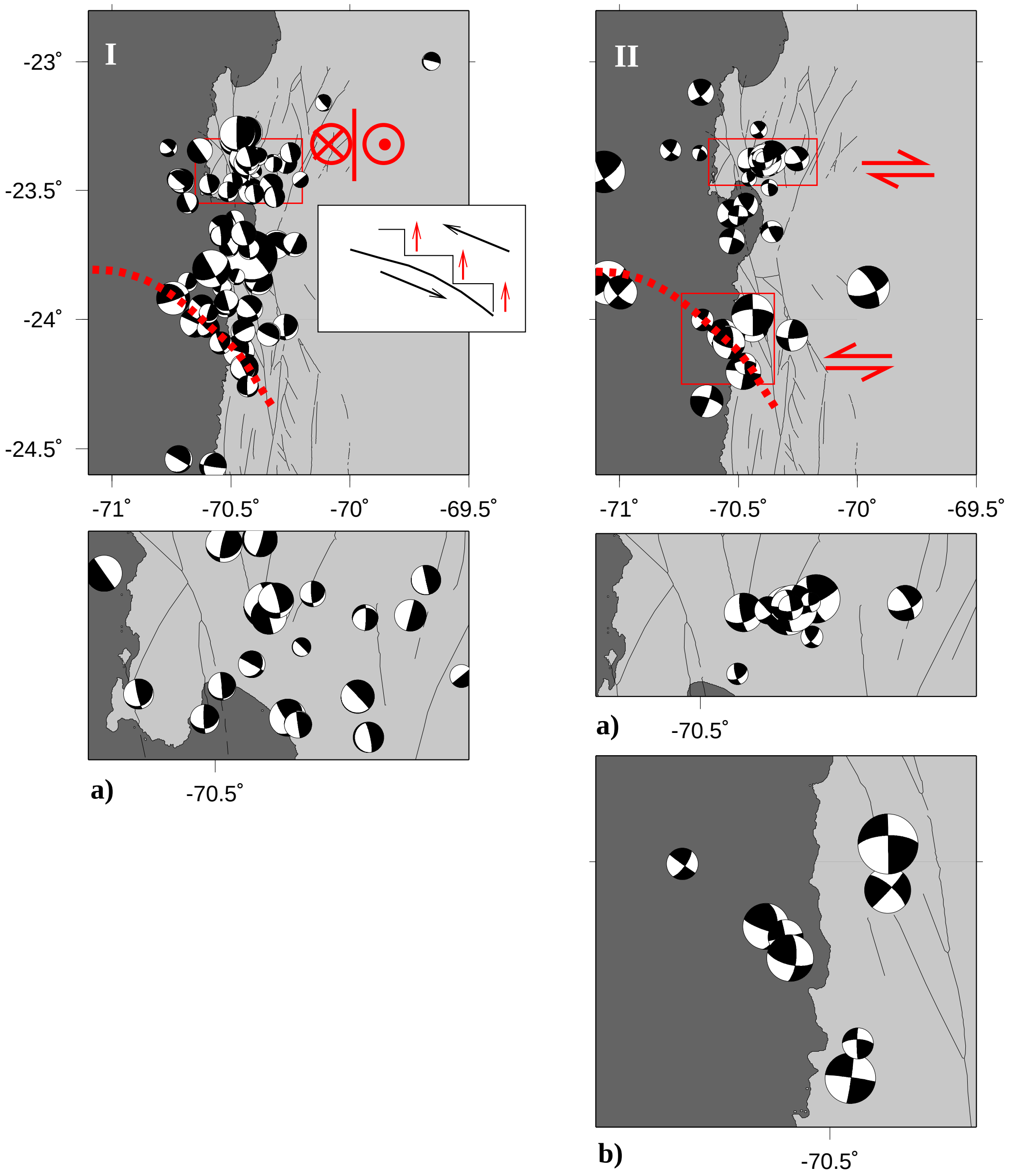

Figure 5.4: I: Events with dip slip mechnisms. The red tail and peak of an arrow denote the assumed direction of coherent movement for the northern group of events. The small sketch refers to an interpretation of the dip slip mechanisms with respect to the overall rupture process. The red dashed line suggests a southern limit of the proposed second segment of the fault plane incorporating the two previously identified asperities. The red rectangle marks the events zoomed in in Ia). II: Events with strike slip mechanisms. The arrows show assumed coherent movements of the northern and southern group marked by a rectangle. IIa) and b) shows a close up of the two groups.

general rupture behaviour which might not involve local strike slip mechanisms. Normal faults (Fig. 5.3 d) make out the smallest catagory among all mechanisms. They are dispersively distributed without a coherent orientation and are thus not easily attributed to any plausible phenomenon related to the rupture process. Probably they are due to very local "site"-effects in the depth on locations which do not follow any general trend.

Owing to the resolution achieved in hypocenter determination for the investigated data set it can be assumed, that the aftershock sequence occured in the interface zone between the upper and lower plate. Thus the events with focal mechanisms studied here do belong to the interface area. The majority of events in all four mechanism catagories occur between 30 and 40 km depth. The histogram in Fig. 5.5 shows the depth distributions of the four mechanism types relatively to a hypothetical interface plane with 20° dip starting at 71.5°W (trench). In this perspective the majority of events lies beneath the hypothetical interface plane where the maximum of thrust events occurs nearest to it. The maxima of dip slip and strike slip events occur slightly deeper indicating a degraded internal faulting structure of the interface zone. This observation has to be taken as a tendency as the relative error for depth calculation of these events is +/- 2km which is the bin width of the histogram columns. However, above the hypothetical interface plane (at 0 depth in the normalized histogram) thrust events seem to be absent whereas dip slips, strike slips and normal faults do still occur.

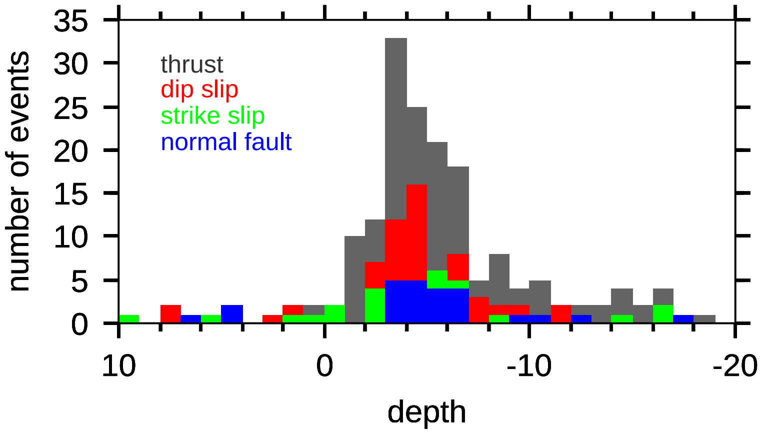

Figure 5.5: Depth distribution of the different focal mechanism catagories. Zero depth marks a hypothetical interface plane with a dip of 20° hinged at the deep sea trench.

5.2.2 Constraints from summed moment tensors

All fault plane solutions of the 295 aftershocks as presented in the previous section were converted into moment tensors, calculating a moment for each event by using Eq. 5.2. For doing so, it has to be assumed that the routinely determined M_L magnitudes are equivalent to moment magnitudes Mw.

The division of the main shock fault plane in a northern and southern part as established in the previous section is also adopted for the investigation of the moment tensors. Thus all moment tensors of events north of 23.5° and all moment tensors south of this line, were summed up according to Eq. 5.3 for each mechanism catagory. The results are four summed moment tensors for the northern part of the fault plane, one for each

Table 5.2: *Northern part of main shock fault plane*

mechanism	DC in %	CLVD in %	f_{clvd}
thrust	73.4	26.5	-0.13
dip	89.4	10.5	-0.05
strike	87.3	12.6	0.06
normal	37.6	62.3	-0.31
total north	91.9	8.1	0.04

Table 5.3: *Southern part of main shock fault plane*

mechanism	DC in %	CLVD in %	f_{clvd}
thrust	53.1	46.8	-0.23
dip	73.6	26.3	-0.13
strike	71.7	28.3	-0.14
normal	51.8	48.1	-0.24
total south	87.3	12.7	0.06

mechanism catagory, ($\mathbf{M_{sum}}$thrust, $\mathbf{M_{sum}}$dip, $\mathbf{M_{sum}}$strike and $\mathbf{M_{sum}}$normal) and four summed moment tensors for the southern part of the fault plane. The summed moment tensor solutions for each catagory in the north and in the south respectively can be seen in Figures 5.6 a) - c) and 5.7 a) marked by an A.

The summed moment tensors in all mechanism catagories were decomposed again according to Eq. 5.6, which is a decomposition into an isotropic, DC and CLVD component. As all input moment tensors, used to calculate the summed moment tensors, are deviatoric, the isotropic components of the summed moment tensors are zero. Thus the result of the decomposition gives the share of the DC and CLVD components in percent for the summed moment tensors (Table 5.2 and Table 5.3). The Tables also give the f_{clvd} for each mechanism catagory, calculated according to Eq. 5.6. This parameter expresses the same as the share of DC and CLVD in percent which is a measure of the deviation of the moment tensor from a pure double couple source.

The summation of the input moment tensors and the decomposition of the summed moment tensors was done by using programs and sub-routines by *Jost & Herrmann* (1989) and *Estabrook, 1999, written comm.*. Details as eigenvalues, eigenvectors, scalar seismic moments and principle axes can be found in Appendix I. All summed moment tensors (A), their DC components (B) and their CLVD components (C) respectively are presented in Fig. 5.6 a) - c) (northern part) and Fig. 5.7 a)-c) (southern part). This was done by using the GMT implemented routine for plotting moment tensor solutions.

Fig. 5.6 shows the results of the moment tensor summation and decomposition into DC and CLVD components of the three most important mechanism catagories for the

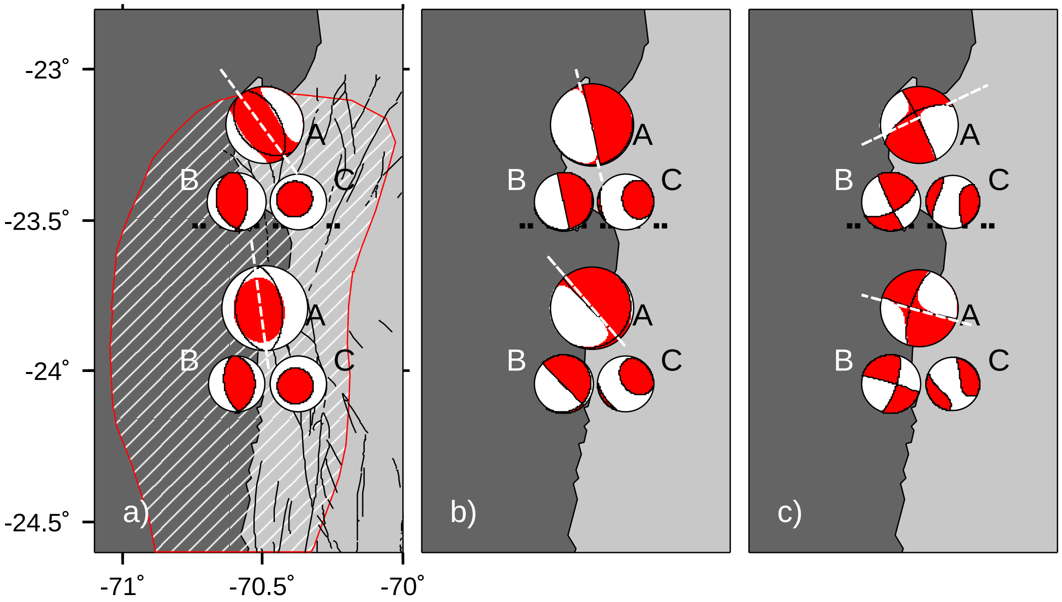

Figure 5.6: Moment tensor representations for the summed moment tensors for a) thrust, b) dip slip, c) strike slip mechanism catagories for the northern and southern part of the main shock fault plane respectively. The larger symbol (A) represents the summed moment tensor, the smaller symbols (B) the double couple component and (C) the CLVD component. The black dashed line marks the limit between northern and southern part of the main shock fault plane. The white dashed lines give the strike direction of each solution.

northern and southern part of the main shock fault plane respectively. Examining the summed moment tensor solutions (large symbols marked by an A) it is interesting to note that the orientations of their principle axes change from the northern to the southern part of the fault plane. The angle between the strike of $\mathbf{M_{sum}}$ of thrusts in the north and $\mathbf{M_{sum}}$ of thrusts in the south is approximately 30 - 35 ° (Fig. 5.6 a). The same is true for the strike axes of dip slips when comparing north to south (Fig. 5.6 b). The $\mathbf{M_{sum}}$ of the strike slips in the north does reveal the opposite pattern of pressure and tension than $\mathbf{M_{sum}}$ of the strike slips in the south. This observation is congruent with the general interpretation of the strike slip mechanisms as given in section 5.2.1, disclosing the segmentation of the mainshock fault plane perpendicular to the direction of main shock rupture propagation.

The DC components (marked by a B in Fig. 5.6 and Fig. 5.7) reflect the same mechanisms as the simple fault plane solutions of the individual aftershocks. In most cases their strike directions are similar to with the strike directions of their corresponding summed moment tensors. A remarkable difference in strike directions can be noted between northern and southern summed moment tensors and DC components. The difference between strike directions of the northern and southern thrust events yields 33°, which is the same for dip slip events. The strike directions for the strike slip events differ by 47° from north to south, for the summed moment tensors of all catagories it is 27° (see dashed lines in Fig. 5.6 and Fig. 5.7).The CLVD components (marked by a C in Fig. 5.6) seem to provide additional information about the local variations in the stress field. But it has to be kept in mind, that the CLVD's have different degrees of significance as shown in Table 5.2 and Table 5.3. The southern thrust events have one of the largest CLVD components (46.8 % of the summed moment tensor) demonstrating that some NS directed pressure component is acting on the second segment of the fault plane. The thrust events also exhibit the strongest increase in CLVD component from 26.5 % in the north to 46.8 % in the south. This increase in CLVD from north to south can be observed also for dip slip and strike slip events. Only the normal mechanism catagory has a change in the CLVD component from 62.3 % in the north to 48.1 % in the south and thus maintains its significance on both parts of the fault plane.

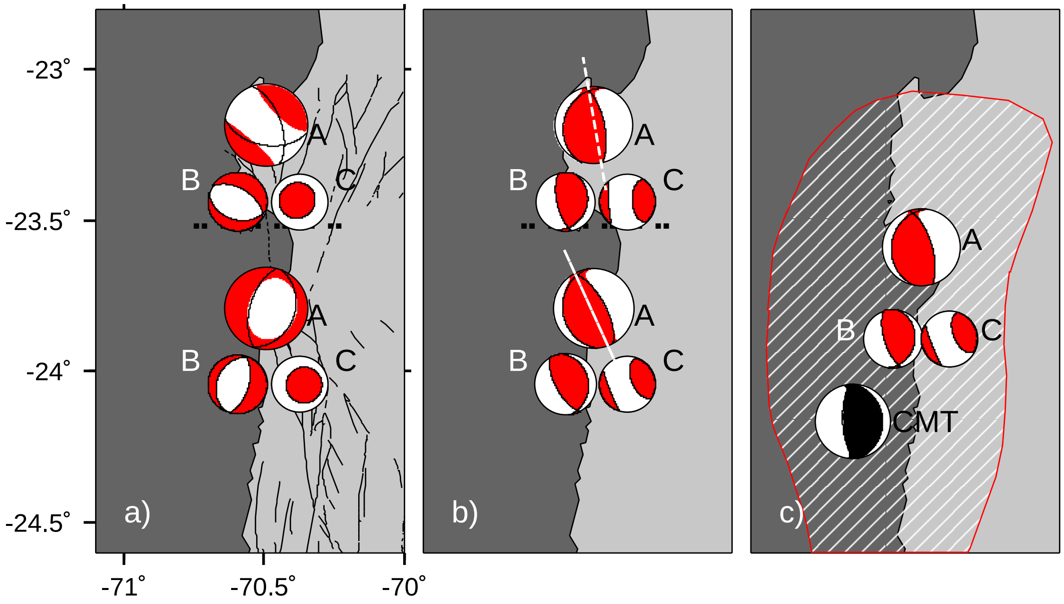

Figure 5.7: Moment tensor representations for the summed moment tensors for a) normal mechanisms. In b) all input events in the north and in the south were summed up disregarding their focal mechanism and c) shows the summed moment tensor for all participating events over the entire fault plane. (A), (B), and (C) as in Fig. 5.6. Hatched area in c) marks the fault plane as derived from aftershock distribution for reference.

This is also true for the results on the CLVD component for $\mathbf{M_{sum}}$ composed of all mechanism types in the north and in the south (Fig. 5.7 b), denoted as "total north" and "total south" in Table 5.2 and 5.3 but the percentages of CLVD of 8.1 % and 12.7 % never reach 20 % (*Kuge & Kawakatsu*, 1993) as a threshold for significance. For completeness, $\mathbf{M_{sum}}$ over the entire fault plane is given in Fig. 5.7 c). The DC component of $\mathbf{M_{sum}}$ is in good agreement with the Harvard CMT solution (*Dziewonski et al.*, 1996) for the Antofagasta main shock. The parameters for both solutions, Harvard CMT (*Dziewonski et al.*, 1996) and the determined summed moment tensor from all available aftershocks, are given in the following Table 5.4 and Table 5.5

Both solution are representing a thrust mechanism. The CMT solution shows a dip of the fault plane of 22° in east direction which is in good agreement with the 20° dip

Table 5.4: **Harvard CMT solution**

moment tensor representation					best DC			
axes	eigenvalue	plunge	AZM	M_o	plane	strike	dip	rake
T	11.91	67	90	12.15	A	354	22	87
B	0.46	1	357		B	177	68	91
P	-12.38	23	267					

Table 5.5: **Summed Moment Tensor $\mathbf{M_{sum}}$total**

moment tensor representation					best DC			
axes	eigenvalue	plunge	AZM	M_o	plane	strike	dip	rake
T	0.48×10^3	66.3	53.7	0.49	A	162	67	79
B	0.14×10^2				B	8.6	25	113
P	-0.49×10^3	21	260					

of the interface derived from the vertical profile of the aftershock distribution. The total $\mathbf{M_{sum}}$ solution also gives a dip of about 20° of its fault plane but in opposite direction which means dipping towards the west. The plunge of the CMT's tension axis T is 67° measured from the horizontal towards the east and the plunge of the total $\mathbf{M_{sum}}$ T axis is 66° towards the west. Thus the principle T and P axes of the two solutions were rotated approximately by 47° (see following section Fig. 5.9). This rotation of T and P axes with respect to the CMT axes is also apparent in the other summed moment tensors of thrust type as shown by $\mathbf{M_{sum}}$ of the thrust catagory in the south and the total $\mathbf{M_{sum}}$'s of the northern and southern fault plane.

5.2.3 Discussion and interpretation

Summerizing in general the results obtained from the aftershock fault plane solutions (section 5.2.1) and their summed moment tensor representations (section 5.2.2) it can be proposed that the two methods reveal: **1)** a possible faulting structure in the interface zone or the confining areas, **2)** a segmentation of the main shock fault plane perpendicular to the rupture propagation and the division of the main shock fault plane in a northern and a southern part. The much larger southern part hosts the assumed asperities as interpreted from the spatial *b*-value distribution (Chapter 3). **3)**The mean deformations obtained through summing up aftershock moment tensors refer to a stronger complexity on the southern fault plane section, indicating there a deviation of the rupture process from pure shear faulting.

1) Faulting structure in the interface zone:
As already pointed out above, the tension axis T of the main shock CMT solution and the T axis of the total summed moment tensor of the aftershocks as well as the thrust type mechanisms differ by an angle of approximately 50°. This is explained again in

Fig. 5.8 offering a view from the side onto a vertical profile of the subducting slab or interface zone. The principle T and P axes of the summed moment tensor (Fig. 5.7 a), the supposed active fault plane, and its force couple are marked in red. Providing that many aftershock events do have the thrust type mechanism as exhibited by the summed moment tensor, the faulting situation could be as it is presented in Fig. 5.8 b). Under the described circumstances a system of parallel sub-faults along the dip of the subduction interface might have developed according to the assumed active summed moment tensor fault plane. Parallel vertical sub-faults are marked in blue showing the same upward directed slip as the faults with the inclined fault plane. For both hypothesized fault types numerous aftershock focal mechanisms can be found in the thrust catagory (Fig. 5.3 a) and the dip slip catagory (Fig. 5.3 b).

2) Segmentation of the main shock fault plane:
The aftershocks with a strike slip mechanism seem to appear rather on east-west trending line features than being distributed homogeneously on the main shock fault plane. This was taken as a first hint that they occur along boundaries which can be interpreted as segmentation faults of transform character. The faulting sense of the strike slips supports the hypothesis as it is right lateral in the north and left lateral in the south. Fig. 5.9 a) shows the infered structure which could be interpreted by this observation: a drawer- or wedge-like segment pushed towards the trench during coseismic deformation. The suggested transform segmentation faults might have offsets on which thrust, dip slip or even normal fault events could occur (Fig. 5.9 a). Fig. 5.9 b) shows that the majority of the thrust mechanisms also lie on lineaments marked by white lines in the figure. A remarkable observation is the congruency of thrust event lineament B (Fig. 5.9 b) with the elongated strike slip cluster in the same area (Fig. 5.9 a). Both event types make up a group of at least 14 successive events within a range of 20 to 30 km suggesting that the break-up mechanism as proposed for the segmentation faults can happen on a rather small scale.

The summed moment tensors of the strike slip group support the hypothesis of the segmentation. The change in strike direction between the northern and the southern group (Fig. 5.6 c) has a remarkable amount ($\sim 44°$) which refers to a slight slip partitioning of the coseismic slip.

3) Complexity of the main shock fault plane:
Due to the high quality standards of seismological data comprising global, regional and local networks, the non-double-couple (NDC) components of moment tensor solutions have gained importance on the interpretation of source mechanisms. One special case of NDC mechanisms is the deviatoric compensated linear vector dipole (CLVD) introduced by *Knopoff & Randall* (1970) to give an explanation for the source mechanism of deep earthquakes (e.g. *Frohlich et al.* (1989). Meanwhile it has been established in many publications that non-pure-shear components are also evident in shallow and intermediate depth earthquakes, swarm activities and seismicity in volcanic regions, which might be explained by a CLVD-type mechanism (*Dziewoński & Woodhouse*, 1983; *Kubas & Sipkin*, 1987; *Kuge & Kawakatsu*, 1993; *Julian et al.*, 1997; *Kubo et al.*, 2002; *Horálek et al.*, 2002) (see also previous sections). From recent investigations on CLVD components three major explanations for their occurrence are cropping out:

- complex seismic events, consisting of two or more sub-events, occurring on non-

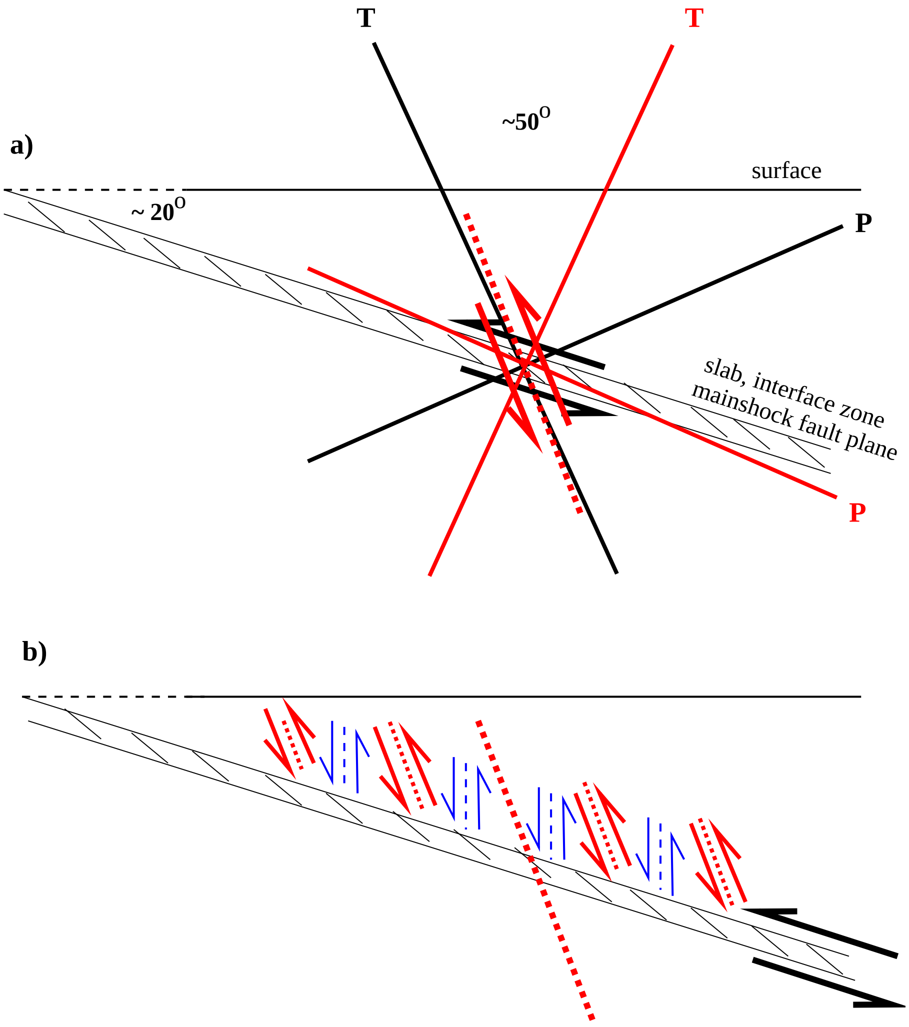

Figure 5.8: a) Arrangement of the principle P and T axes of the Harvard CMT solution (main shock) (black lines) and the total summed moment tensor of the aftershocks (red lines) transferred to a vertical profile along the subduction interface. The force couples of the plausible active fault planes due to the orientation of the principle axes are marked by black and red arrows respectively. b) Description of the hypothesized aftershock faulting along the subduction interface. The suggested parallel sub-faults marked in red and blue can explain the occurrence of aftershocks in the thrust and dip slip catagories.

parallel fault surfaces,

- earthquakes, in which slip occurs along curved fault surfaces, and
- fluid driven opening of tensile cracks

Examining the southern main shock fault plane, it can be noted that summed moment tensors on this part are produced by individual aftershocks having more distinctly oriented strike directions. This would correspond to the cause for CLVD's described in the first item, as the individual aftershocks obviously occur on non-parellel faults.

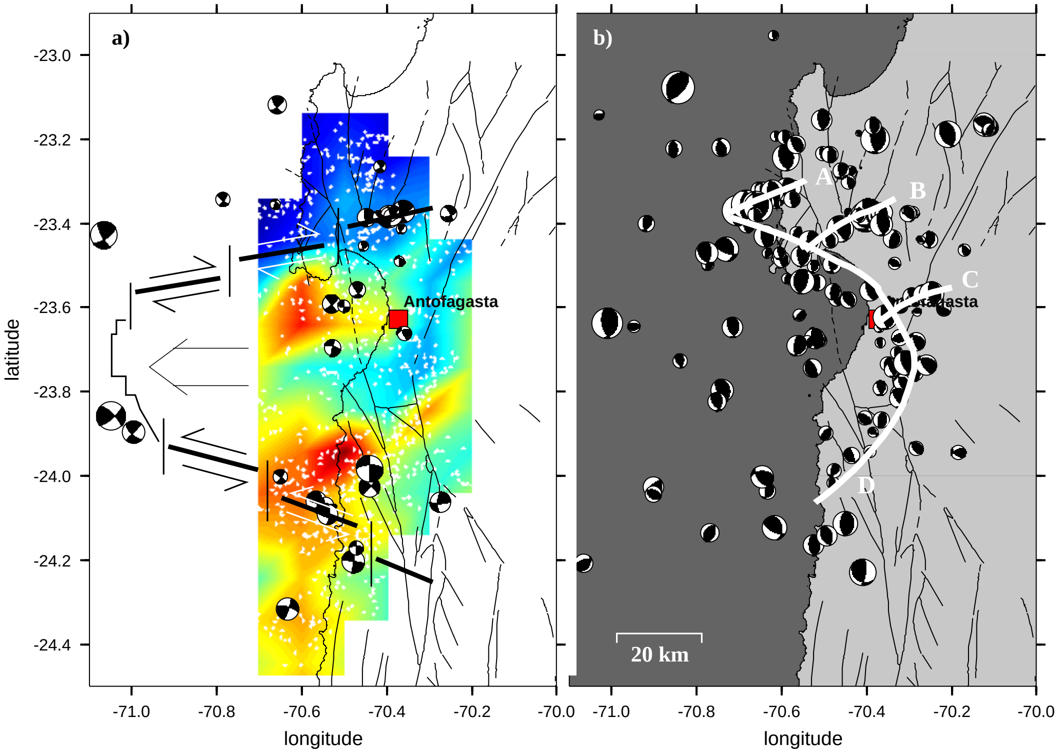

Figure 5.9: a) Scheme of the hypothesized wedge-like shape of the second segment of the main shock fault plane which comprises the assumed asperities as identified in the b-value map. The northern boundary of the segment shows right lateral strike slip mechanisms, the southern boundary is characterized by left lateral strike slip mechanisms. b) The majority of the thrust mechanisms seem to be arranged on lineaments (marked by white lines named A, B, C, D). Lineament B comprises the same area as the pronounced northern cluster of strike slip events in a). Lineament D encompasses the area which hosts the asperities. See text for interpretation.

Providing that the observed lineament D in Fig. 5.9 b), formed by thrust type aftershocks, lines out a curved segment boundary, then the second item also would serve as an explanation for the observed CLVDs. As remarked previously the lineament D seems to encompass the entire segment which hosts the two proposed asperities (Fig. 5.9).

The CLVD in general describes the deviatoric or traceless part of a tensile earthquake fault. Thus its occurrence is often connected to the opening of tensile cracks which can be provoked by intrusion of fluids or ductile material into already existing weak areas. Combining the idea that high b-value areas are characterized by a higher order perturbation due to a larger number of small fault planes, and the hypothesis derived by *Husen & Kissling* (2001), that the time dependent change of v_P/v_S ratios are due to fluid migration, item three would also hold as an explanation for the cause of CLVDs in the aftershock sequence. As the high b-value areas appear on the southern part of the main shock fault plane this could also explain why the fraction of CLVD in the summed moment tensors is higher in the south than in the north (see also discussion in the next chapter).

Seven CLVD components of the eleven summed moment tensors show eigenvalues arranged as (-1, -1, 2); the northern strike slip CLVD component has (2, -1, -1) as eigenvalues and the CLVDs from total summations of northern, southern and entire fault plane give traces of (-1, 2, -1). Their geometrical representations are given in Fig. 5.10. The equatorial planes of the CLVDs in Fig. 5.10 refer to the compressional area (in relation to the source) where fluids might be intruding, and tensional 2-axes could be marking the direction of crack or fracture opening.

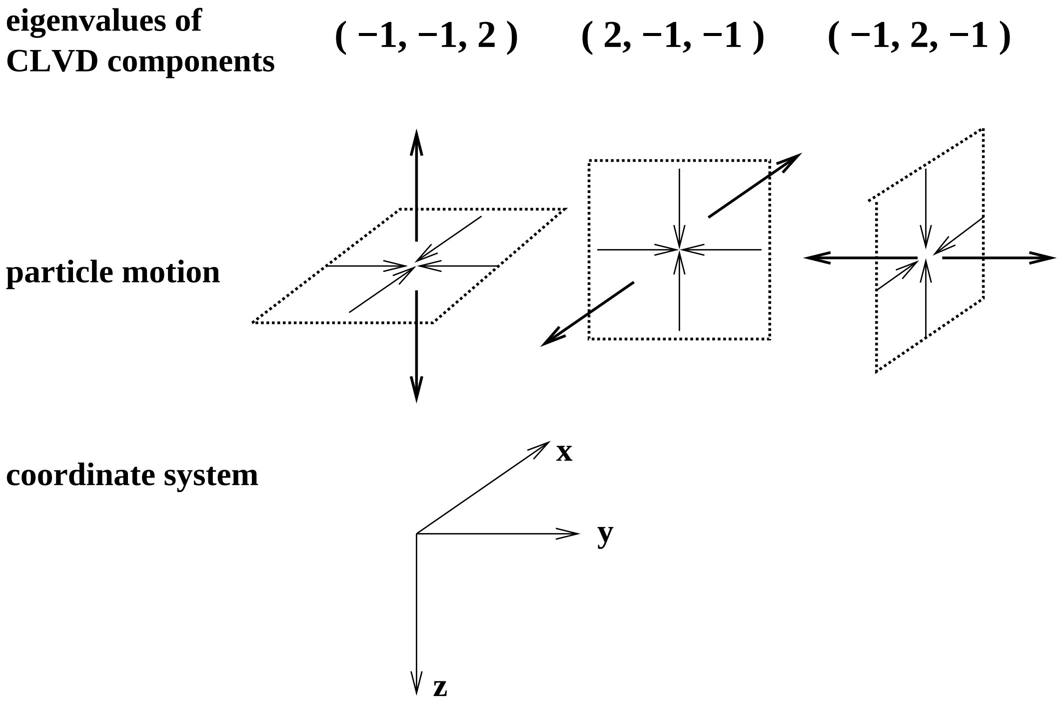

Figure 5.10: Geometric representation of the CLVD components as found from the decomposition of the summed moment tensors.

Summerizing the results obtained from the focal mechanism studies, several major findings should be stressed:

- The separate studies of the four focal mechanism catagories could reveal a possible segmentation of the main shock fault plane, the segment boundaries and the division of the fault plane into a northern part of rather small extent (from the beginning of the main shock rupture to the southern tip of Mejillones Peninsula) and a much larger southern part, comprising the two proposed asperities. This southern area is supposed to be a major segment of the fault plane.

- The average deformation of the northern and southern fault plane, derived from summing up the individual aftershock moment tensors, inferes a rotational component from north to south. This suggests slight slip partitioning of the seismogenic zone.

- The information obtained from the tensional axes of aftershock moment tensors and the occurrence of thrust and strike slip mechanisms on identical lineaments might resolve the small scale rupture process in the interface zone.

- The pronounced increase in percent of CLVD components of the aftershock moment tensors on the southern segment deduces a higher complexity of this fault plane part than in the north under Mejillones Peninsula. This might be interpreted in terms of an introduced 3D feature caused by the geologic structures responsible for the asperities.

6. Final model, conclusions, and outlook

6.1 Final model

Following the individual discussions in the previous chapters, a final model can be proposed for the seismotectonic situations before, during, and after the mainshock in the subduction interface zone where the 1995 Antofagasta earthquake occurred:

Situation before the main shock: As an initial seismotectonic situation, assumed from the previous discussion, the two asperities, identified in this study, are patches of stronger resistance against the convergent motion of the Nazca and South American plates. They define areas where stresses are accumulated in the seismogenic zone prior to a large earthquake. One asperity is located off-shore to the west of Antofagasta, which corresponds to a depth of 20 to 30 km. A second, larger asperity is located south-east of Antofagasta around 24°S with its largest part off-shore, corresponding to a depth range of 20 to 40 km. Direct evidence for the stress accumulation in this area was found by *Porth* (1993) whose results of seismicity investigations show low b-values where the asperities are expected. Assuming that low b-values are indicators for high apparent stresses, the "patches" of high b-values after the main shock should be "patches" of low b-values before the earthquake, thus lining out the areas of stress accumulation or concentration. The results of *Porth* (1993) exhibit a zone of pronounced low b-values (0.4 - 0.6) in the upper crust between 20 and 25°S and 70 to 71°W (see Fig. 6.1).

Information about the nature and possible 3D spatial extent of the structure which might cause the asperities, can be deduced from mapped isostatic residual anomalies (*Götze et al.*, 1994) and geology (*Pichowiak*, 1994). Provide the anomalies are caused by the intrusive bodies of the Jurassic batholiths, and their locations are furthermore congruent with the locations of the asperities, it can be proposed that the igneous complexes pervade the overriding crust and even intrude to some extent into the seismogenic interface. Here they form the patches of higher resistance to the convergent plate motion. In other subduction zones, subducting seamounts have been discussed successfully as stress concentrators (*Barckhausen et al.*, 1998; *Lallemand & Le Pichon*, 1987; *Cloos & Shreve*, 1996; *Cloos*, 1992). But no evidence of such topographic features is given in the high resolution bathymetry as carried out during the CINCA'95 project (*von Huene et al.*, 1999; *von Huene & Ranero*, 2003). In von Huenes and Raneros model (2003) of the outer forearc in the Antofagasta region, the downgoing slab shows a slight steepening of the subduction angle at $\sim$ 12 km depth. This change in subduction angle might give a hint to the existence of an "obstacle" like the batholith could be, which the slab tries to avoid by steepening its angle. This initial situation seems to correspond at first sight to a classical asperity model as proposed by *Kanamori & Stewart* (1978), *Rudnicki & Kanamori* (1981)

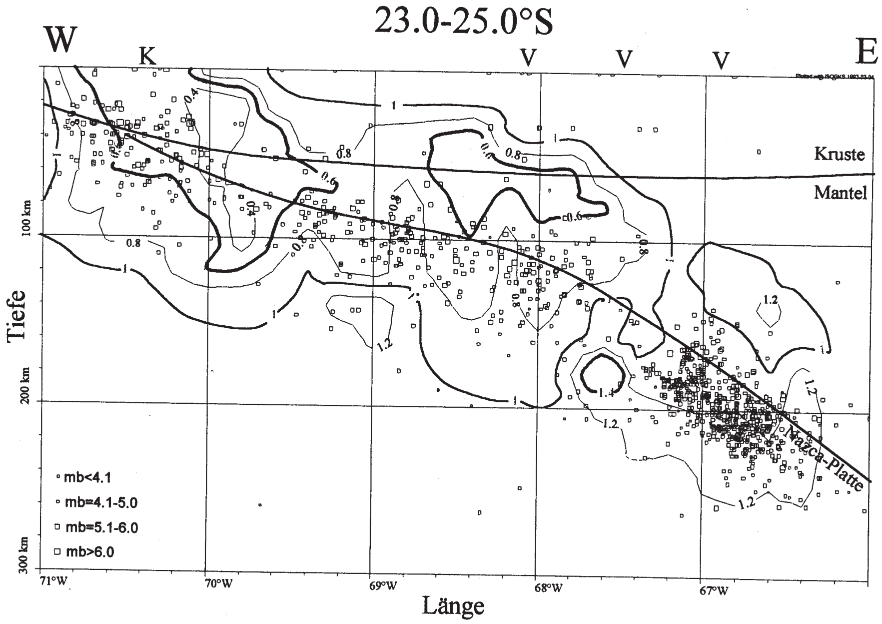

Figure 6.1: East-west *b*-value section between 23°S and 25°S from ISC data by *Porth* (1993). Note the area of low *b*-values (0.4 - 0.6) in the shallow part of the subduction zone. This is congruent with the area where the proposed asperities are hosted.

and *Lay et al.* (1982) whose main characteristic is the varyable stress on the fault. But if the batholiths really playing a role as stress concentrators, they are at the same time patches of higher strength. There, the initial situation deviates from the classical asperity model, and barriers as patches of high strength come into mind. A study of local back ground seismicity by *Delouis* (1996) shows cluster-like activity in the areas of the asperities between 1990 and 1994. So stress accumulation was annotated by back ground events. None of them triggered the large subduction event. Three events of magnitude 3.6, 3.8 and 4.1, which occurred one and two days before the main shock, with epicenters located in the southern Mejillones Peninsula bay (*Delouis*, 1996), are considered to be immediate foreshocks to 1995 earthquake (*Delouis*, 1996).

During the main shock: The rupture of the main shock starts underneath Mejillones Peninsula according to the NEIC solution or the solution given by *Ruegg et al.* (1996) as calculated from the local network. It is interesting to note, that rupture starts in some distance to the first asperity and thus is not initiated at the outer limit of the asperity. Such observations are reported also from other large earthquakes (M. Mai). The rupture propagates southward as it is corroborated by teleseismic directivity studies (*Ruegg et al.*, 1996) and geodetic measurements, being a smooth rupture process for the first 20 km. When the rupture front breaks the asperities, high moment release is indicated in the source time function. Thus the material concerned gets shattered in this process. The asperities alter from highly stressed strong patches to areas with high slip and high stress drop. In the asperity model large slip is associated with asperities, low slip with relaxed areas or creeping sections on the fault. The co-seismic slip on asperity 1 is 7.4 m and 5.0 m on asperity 2 which is in the range of expected slip considering a Nazca plate motion of 6.1 (*Angermann et al.*, 1999) to 6.4 cm/yr (*Norabuena et al.*, 1998) and a seismic cycle for M=8.0 events of 100 to 120 years (*Comte et al.*, 1994). Thus the rupture process of the main shock leaves behind an altered section of the seismogenic zone which is inhomogeneous in slip and stress drop distribution.

After the main shock: After the main shock rupture the seismic activity of the aftershock sequence starts to develop immediately. *Ruegg et al.* (1996) and *Delouis et al.* (1997) report aftershocks of magnitudes between M_w=5 and 7 during the first 10 days after the main shock. A cluster of these large aftershocks is registered off-shore to the northwest of Mejillones Peninsula (*Delouis et al.*, 1997) where stresses seem to concentrate due to stress transfer, triggered by the Antofagasta main shock. This is corroborated by the aftershock derived b-value map which shows the lowest b-values at the coast and northern part of Mejillones Peninsula. The former asperities consist now of shattered material with a high crack density which is reflected in the high b-values in the asperity areas, saying that events with small magnitudes are more abundant than events with high magnitudes. Aftershock activity is highest on and in the vicinity of the asperity structures considering only the southern part of the fault plane, even at later time periods in the aftershock sequence. This contineous activity concentration could result in higher permeability along and above the seismogenic interface where the asperities are hosted, thus giving way to fluid intrusion causing increased v_p/v_s ratios (*Husen & Kissling*, 2001; *Shapiro et al.*, 2003). The elongated cluster of aftershocks just west of the NEIC hypocenter solution, consisting of strike slip and thrust focal mechanisms seems to give a detailed insight into the local rupture process of a segment border. On similar lines of aftershocks, altering thrust and dip slip mechanisms suggest a staircase-like faulting process on the seismogenic interface (see Chapter 5). Investigating the spatial development of the aftershock sequence, it must be noted that in case of the Antofagasta sequence almost all aftershocks occured on the fault plane itself even marking very well its western, northern and eastern limits. A considerable amount of aftershocks outside the fault plane were observed only north of it. Besides the importance of these aftershocks to gain information on the large overdue seismic gap of the 1877 event, the eastern fault plane limit is interesting as it seems to be congruent with the main strand of the Atacama fault system. East of the Atacama fault, aftershock activity changes in frequency of occurrence, spatial distribution in the depth, and dominating focal mechanism (*Delouis*, 1996; *Delouis et al.*, 1997), which can be corroborated by focal mechanisms in this study. Summerizing the observations, the aftershocks seem to be a structural answer to the alternation of the seismogenic zone caused by the main shock.

6.2 Significance of the identified fault plane structures for future earthquakes

The investigated parameters and the model described above, try to resolve the structure of the fault plane area in the Antofagasta region and its role in case of a large subduction event. A striking pecularity of the 1995 Antofagasta earthquake was the moderate damage reported despite the large magnitude of $M_w = 8.0$. There are several reasons to consider as possible explanations. The city of Antofagasta is situated on a narrow stretch of ~ 3 km between the Pacific Ocean and the Coastal Cordillera. The relatively thin sediment coverage above shallow consolidated bed rock can be discussed as one of the main reasons for moderate damage. More severe damage was restricted to thicker sediment layers near the foot of the mountain range and to areas with artificial deposits like the harbour area. 8 to 10 Hz were the dominating frequencies found in response spectra, calculated from accelerograms of the networks' strong motion instruments (*5*, 1996). Considerable damage was observed on 1 to 2 story buildings which had eigenfrequencies in the same frequency range. In addition to this advantageous sub-surface structure beneath Antofagasta, the radiation pattern of the main shock focal mechanism might have contributed to moderate damage distribution. Considering the S-wave radiation pattern of a thrust mechanism on a rupture plane with a dip angle of $\sim 20°$ almost directly beneath Antofagasta, leaves the areas affected by the maximum displacements of the transverse components most likely to the east and to the west of Antofagasta. *Ruegg et al.* (1996) suggest moment release at low frequencies as another plausible cause for minor destruction. They found two peaks in the displacement spectra at 65 and 130 s respectively which would also explain the discrepancies between seismic moments determined by body wave analysis or geodetic data.

A new constraint on the question of distructive features of large earthquakes may come from the identification of asperity structures in the seismogenic zones where large earthquake fault planes are situated. Looking again at the identified asperities in the Antofagasta region, it can be noted, that Antofagasta lies outside of the northern asperity and thus outside of an area with high slip concentration. Therefore the position of a city or settlement away from areas of high moment and slip release might be also considered as an important condition for decreased distruction and damage. A similar conclusion can be drawn from results of the 1997 Cariaco earthquake case study (Venezuela), which will be briefly described in the very last sub-section of this thesis. Here it was found that the city of Cariaco was located above a high moment release asperity and suffered the largest amount of damage along the active fault trace (*Baumbach et al.*, 2004). Such observations seem to enhance in general the question what role do play asperity or barrier structures on the fault plane to the distribution and degree of damage observed in surface structures. *Dmowska & Lovison* (1992) suggested that the identification of asperities by accumulating background seismicity in subduction zones would be helpful to look for future high moment release areas. *Aki* (1984) argues that the agreement found between local stress drops estimated from strong motion data and those inferred from geological observations supports the possibility to predict earthquake strong motion directly from geological structures of the fault. *Papageorgiou & Aki* (1983) constructed a specific barrier model based on the assumptions that strong ground motion is characterized by high frequency content related to the details of faulting. To their oppinion, these details arise from the non-uniform distribution of physical properties, expressed by barriers or asperities. They propose, that the frequencies generated by these details, are higher than the corner frequency f_0 and lower than the cut-off frequency f_{max}, which characterize the flat part of the acceleration amplitude spectra of strong motion. This flat part $\Omega(0)$ in their model is scaled with the local stress drop due to asperities or barriers rather than the "global" stress drop (*Hanks*, 1979) on the entire fault plane (see also discussion Chapter 4). Thus f_{max} in this specific barrier model originates from source effects rather than from propagation effects or site effects.

To better understand in what manner high frequency is radiated, *Frankel* (1991) adopted a model where he found that the high-frequency spectral falloff of the mainshock, the size distribution of subevents and the b-value of aftershock sequences can all be determined from the scaling of strength on the fault zones. Similar to the authors mentioned above, *Frankel* (1991) assumes that high frequency radiation is caused by complex fault structures smaller than the mainshock fault plane. But unlike in previous publications assuming a constant size for barriers or asperities, he uses a self-similar size distribution of subevents in his model. *Frankel* (1991) further postulates from his results that the total high-frequency radiation from the subevents accounts for the high-frequency energy of the mainshock.

Herrero & Bernard (1994) also considered self-similarity for fault plane structures in their model but did go a step further to account for physical constraints that reproduce a given spectral law of the far field displacement. With their kinematic model, the authors wanted to demonstrate the situation on the fault plane in front and behind the propagating mainshock rupture. As a further development of this model, *Bernard et al.* (1996) introduced the concept of a scale-dependent rise time related to the wavenumber and incorporating a directivity effect. The result of this model clearly showed, that the shortest wavelength occurring during rupture propagation are concentrated near the rupture front whereas longest wavelength spread of the entire width of the synthetic pulse. In this context it might be worth mentioning again, that the highest values for aftershock radiated seismic energy, as found in Chapter 3, occurs at a proposed material boundary between batholitic structures and the confining material.

In general, for engeneering purposes f_{max} is an important parameter as it controls peak ground acceleration which is again important for seismic resistant construction (*Papageorgiou*, 2003). In general it is most probable that f_{max} is influenced by a mixture of all occurring effects like source effects, site effects and even effects caused by tectonic settings (*Aki*, 1987; *Kinoshita et al.*, 1992). This is still not very well studied and thus should be an issue of future investigations.

Lifetime of asperities

Considering the significance of these interrelations (*Aki*, 2002) between seismogenic structures, the rupture process and soil dynamics for future earthquakes, the question arises, whether asperities or barriers are stationary features and might be able to cause multiple high moment release in more than one seismic cycle. In the Antofagasta region, we were able to correlate the isostatic residual anomalies of the gravity field to the proposed asperities. We interpret the geological structures, the Jurassic batholiths, responsible for these anomalies, as a possible cause for the asperities. This would mean, as the batholiths are stable features over geological time scales, that the asperities could break repeatedly at the end of various seismic cycles.

Regarding this result, one might speculate that other subduction earthquakes along the South American Pacific coastline are also influenced by plutonic structures. This suggestion is supported by comparing the peculiar chain of high isostatic residual anomalies along the coast (*Götze et al.*, 1994) to historic earthquakes as shown in Fig. 2.8 in chapter 2. The resulting impression is that subduction earthquake fault planes start and end where the IRF anomalies are interrupted.

The calculation of recurrence times involve the assumption that the recurrent earthquakes of one magnitude level at major plate boundaries inherit a fault plane of similar location and dimension. This implies that at least some geological and tectonical structures having a life time of millions of years will be repeatedly involved in rupture processes. Considering these structures as candidates for stress concentrators capable of forming asperities or barriers, it should be most probable that the same asperity participates in various seismic cycles. Several authors have tried to evidence stationarity of asperities or barriers by observing stationary stress drop and slip distributions on faults (*Bakun & Joyner*, 1984; *Aki*, 1984; *Bouchon et al.*, 1998), geologic features that are repeatedly reflected in seismicity (*Lay & Kanamori*, 1981; *Dmowska & Lovison*, 1992; *Cloos & Shreve*, 1996; *Barckhausen et al.*, 1998), or by searching for locked and unlocked parts of faults with the help of geodetical data (*Bürgmann et al.*, 2000).

Other observations which can be explained by stable asperities or barriers are coming from paleoseismology. In trenching experiments it was found, that earthquakes can reoccur several times on a given fault with the same rupture length and amount of slip (*Aki*, 1984). But not only for large earthquakes stationary asperities have been proposed. *Johnson & Nadeau* (2002) claim to have identified a small strong asperity patch on the San Andreas fault, which is responsible for the observed repeated small earthquakes and thus can be interpreted as a rather stable resistant feature on the fault.

6.3 Conclusions and outlook

The results of this thesis emphasize that the b-value mapping is a convenient method to identify asperity structures from aftershock sequences, provide that adequate networks and sufficiently large data sets are available. The b-value map provides information directly from the fault plane itself which helps to resolve also small scale or higher order structures, which other methods might not capture. In case of the Antofagasta earthquake, the northern asperity, which is the smaller one in extent but larger in average slip, was resolved only by the b-value mapping. Its position off-shore did cause problems to purely landbased methods. In addition, the seaward extension of the temporary seismic network improved the precision of hypocenters for aftershocks along the coast and off-shore, which also improved the detectability of the asperity 1 with seismological data.

The correlation of independently derived parameters having a spatial distribution on the fault plane (mainshock source time function, isostatic residual anomalies, radiated seismic energies from aftershocks, v_p/v_s ratios from LET) helped to evaluate b as a reasonable indicator to map location and size of inhomogeneous structures on the fault plane which react with the propagating rupture of the mainshock. The results are shown and discussed in detail in Chapter 3. Summerizing in short the major conclusions, the following list can be established:

- the spatial b-value variations are significant and linked to changing physical properties on the fault plane, mapping out size and location of strongly damaged areas which can be identified as asperities,
- high values of E_s derived from aftershocks occur at material boundaries and in stress transition zones between asperities and on adjacent areas to the fault plane,
- the uplifted Jurassic batholiths in the Antofagasta region coincide with the asper-

ities; mass balances and the permanent subduction process are responsible for the accumulation of stress on the asperities during one seismic cycle.

An additional important finding is, that the spatial distributions of all correlated parameters orientate according to the geological structure, namely the batholiths, in the area of Antofagasta. They are derived from either the pre-, co- or postseismic stage of the seismic cycle. With respect to aftershock sequences, this allows to state that from their behaviour also seismotectonic situations before and during a mainshock rupture can be deduced. The histogram of the number of aftershocks with latitude (Chapter 3, Fig. 3.17) shows, that from aftershock hypocenter distribution alone, it is difficult to detect high slip areas. The Antofagasta aftershock distribution demonstrates that high slip areas can also contain a considerable amount of events.

From the obtained aftershock focal mechanisms (see Chapter 5) it can be said that they do not only reveal how stress is redistributed in the fault plane area (*Beroza & Zoback*, 1993; *Scherbaum*, 1994) but also confirm "topography" on the fault surface which is probably linked to the asperity structure.

In context with the interpretation of b-value variations, the significance of the differences $\Delta\ b$ in one map are more important than the absolute b-values as they do vary according to the method used for estimation. However it is interesting to note that the overall b-values for the entire aftershock data sets examined are commonly between 0.70 and 0.80. In general, future investigations of the frequency-size distribution of aftershocks either by assuming self-organized critical or power law behaviour, should recognize the study of small scale variations in the local areas, as they obviously have a physical meaning.

Relying on the previous observations and findings, it can be concluded that in combination with other parameters in a source region, the b-value mapping provides not only a method to identify asperities but also helps to understand their nature. This information could be essential for the estimation and assessment of the seismic potential (calculating re-currence times for large events only in asperities as suggested by *Wiemer & Wyss* (1997)) and hazard in future earthquakes, provide it can be established that asperity structures are stationary over various seismic cycles. The correlation of the high b-value areas with the isostatic residual anomalies let us assume that the proposed asperities are stable for many seismic cycles.

Moreover, the proposed tectonic model for the Antofagasta area points out that geological structures of the upper plates' crust can play an important role on forming asperities when these structures are capable to pervade the crust and influence the seismogenic interface. Formerly only topographic features on the subducting plate were considered to create resistance to the general convergent movement and thus provoke stress accumulation in particular areas. It might be suggested that in many subduction zones a combination of upper plate geologic structures and subducting seamounts or ridges are responsible for such local stress field inhomogeneities.

The results of this thesis show once more that the investigation of aftershock sequences reveal important facts about local seismotectonic structures. By studying a variety of parameters, important conclusions can be drawn on structures that could influence future earthquake damage distributions. Namely the interaction between high seismic moment asperity structures and soil dynamic features related to engeneering concerns, should be investigated in the future. It needs to be checked whether damage probabilities are higher for surface structures near or on asperities despite or because of soil interactions. An organisation like the German Task Force for earthquakes has proven to be an excellent tool for this purpose.

6.3.1 *Final remark on further studies*

The investigations carried out in this thesis with the Antofagasta aftershock data set, namely the *b*-value distribution on the fault plane, the application of an asperity model and the study of average deformations by aftershock focal mechanisms, were also applied to the aftershock data set of the M_w=6.9 Cariaco earthquake in July 1997. The data set was collected, pre-processed and analysed by members of the Task Force at GFZ, Potsdam (*Baumbach et al.*, 2004). It is remarkable that the results of these investigations are similar to the Antofagasta results, although the Cariaco earthquake occurred in a different tectonic environment. The El Pilar fault, which ruptured on a length of $\sim$ 40 - 60 km during this earthquake, is part of a wider, 100 to 200 km brought transcurrent fault zone of parallel and oblique strike slip sub-faults which define the margin between the Caribbean and the South American plates. The similarities of results are listed in the following:

- The *b*-value varies significantly on the fault plane of the strike slip event. Although areas of high *b*-values are smaller in extent compared to the high *b*-value areas of Antofagasta, they are well constrained and detectable.
- Correlation of the *b*-value distribution with results of a 3D tomography using the same aftershock data set, shows that the proposed main asperity apparently is linked to an indent structure of harder material from the northern side of the El Pilar fault, penetrating into the southern side of the fault.
- This indent structure creates a sort of topography on the fault plane which expresses itself also in the character of summed moment tensors of aftershocks in the same area. The moment tensors are dominated by large CLVD components, which indicate a deviation of focal mechanisms from pure double couple mechanisms.

In addition, it could be observed, that the strongly destructed city of Cariaco is located just above the a high *b*-value area, which is proposed to be an asperity with high moment release during earthquake rupture. On the other hand the city of Casanay, approximately 15 km east of Cariaco, which is also located directly on the fault trace and most likely with a soil type similar to that in Cariaco, reported only minor damage. This suggests again a relation between damage distribution and distance to an asperity as observed in the Antofagasta case study.

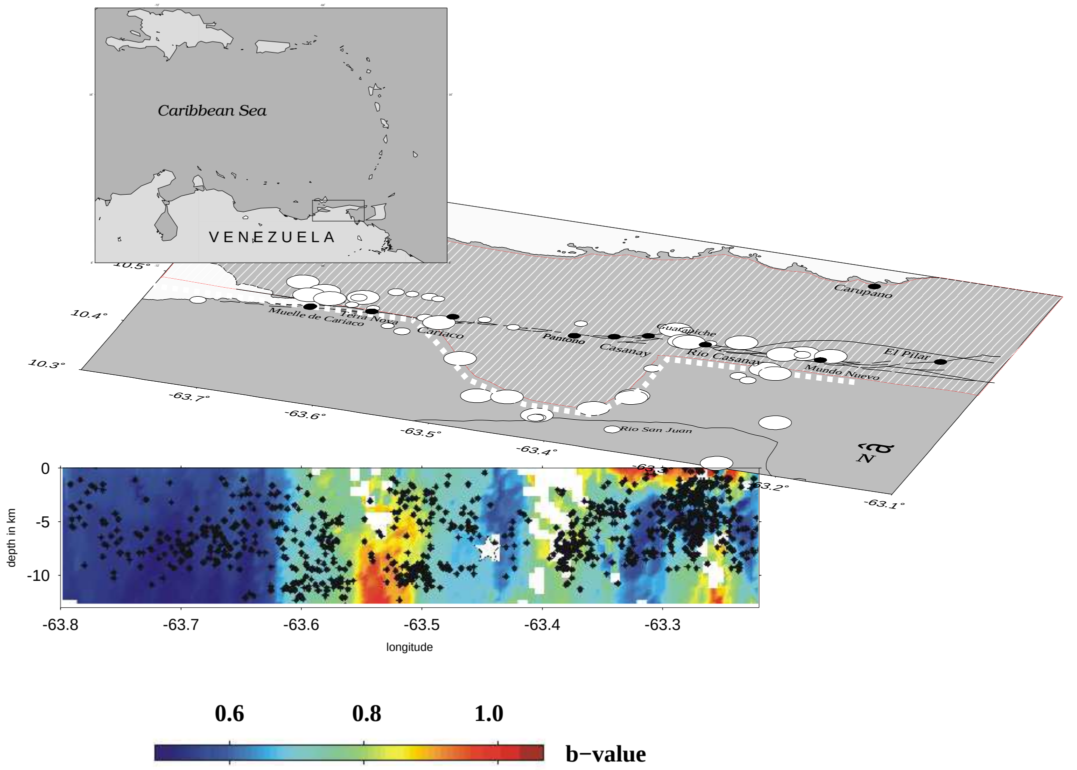

Figure 6.2: b-value map of the 1997, $M_w = 6.9$ Cariaco earthquake which ruptured approximately 60 km of the active El Pilar fault in north-eastern Venezuela. The right lateral El Pilar fault belongs to the plate boundary system between the Caribbean and the South American plates (see upper small sketch). The black lines on the map mark the El Pilar fault system. The area marked by white stripes, denotes a geologically stronger material, belonging most likely to the Caribbean plate. This material, characterized by higher v_p velocities, as determined from a local earthquake tomograghy, form an indent like structure, penetrating into the area south of the El Pilar fault. This occurs at a depth of approximately 5 - 6 km. The asperity structure in the center of the b-value map, characterized by high b-values, is situated just where the indentor starts, where the material boundary should be located. The white dashed line is giving again the southern border of the stronger material. White dots show epicenters of aftershocks with normal fault mechanism.

Bibliography

5, A., Desasterforschung, in *Zweijahresbericht, GFZ Potsdam*, GFZ Potsdam, 1996.

Aki, K., Maximum likelihood estimate of b in the formula log n=a-bm and its confidence limits, *Bull. Earthquake Res. Inst.*, *43*, 237–239, 1965.

Aki, K., Characterization of Barriers on an Earthquake Fault, *J. Geophys. Res.*, *84*, 6140–6148, 1979.

Aki, K., A probabilistic synthesis of precursory phenomena, in *Earthquake Prediction-An International Review, Maurice Ewing Series 4*, American Geophysical Union, Washington, D.C., 1981.

Aki, K., Asperities, Barriers, Characteristic Earthquakes and Strong Motion Prediction, *J. Geophys. Res.*, *89*, 5867–5872, 1984.

Aki, K., Magnitude-frequency relation for small earthquakes: A clue to the origin of f \d\max\u of large earthquakes, *J. Geophys. Res.*, *92*, 1349–1355, 1987.

Aki, K., Higher-order interrelations between seismogenic structures and earthquake processes, *Tectonophysics*, *211*, 1–12, 2002.

Aki, K., M. Fehler, & S. Das, Source mechanism of volcanic tremor: Fluid-driven crack models and their application to the 1963 Kilauea eruption, *J. Volcanol. Geotherm. Res.*, *2*, 259–287, 1977.

Ambraseys, N., & J. Bommer, Uniform magnitude re-evaluation for the strong motion data base of Europe and adjacent areas, *European Earthquake Engineering*, *2*, 3–16, 1990.

Amitrano, D., Brittle-ductile transition and associated seismicity: Experimental and numerical studies and relationship with the b value, *J. Geophys. Res.*, *108*, ESE 19–1 to 19–15, 2003, citation no. 2044, doi: 10.1029/2001JB000680.

Angermann, D., J. Klotz, & C. Reigber, Space-geodetic estimation of the Nazca-South America Euler vector, *Earth planet. Sci. Lett.*, *171*, 329–334, 1999.

Apperson, K. D., Stress fields of the overriding plate at convergent margins and beneath active volcanic arcs, *Science*, *254*, 670–678, 1991.

Asch, G., A. Rudloff, F. Gräber, R. Kind, G. Bock, & K. Wylegalla, Hochauflösende Seismologie in den Zentralen Anden, in *Zweijahresbericht, GFZ Potsdam*, GFZ Potsdam, 1996.

Bak, P., & C. Tang, Earthquakes as a self-organized critical phenomenon, *J. Geophys. Res.*, *94*, 15,635, 1989.

Bak, P., K. Christensen, L. Danon, & T. Scanlon, Unified scaling law for earthquakes, *Phys. Rev. Letters*, *88*, 178,501–1–4, 2002.

Bakun, W. H., & W. B. Joyner, The ML scale in Central California, *Bull. Seism. Soc. Am.*, *74*, 1827–1843, 1984.

Banks, R., R. Parker, & S. Huestis, Isostatic compensation on a continental scale: local versus regional mechanisms, *Geophys. J. R. astr. Soc.*, *51*, 431–452, 1977.

Barckhausen, U., H. A. Roeser, & R. von Hüne, Magnetic signature of upper plate structures and subducting seamounts at the convergent margin off Costa Rica, *J. Geophys. Res.*, *103*, 7079–7093, 1998.

Baumbach, M., H. Grosser, G. RomeroĹeerzeichen’Torres, J. L. RojasĹeerzeichen’Gonzales, M. Sobiesiak, & W. Welle, Aftershock pattern of the July 9, 1997 Mw=6.9 Cariaco earthquake in Northeastern Venezuela, *Tectonophys.*, *397*, 1–23, 2004.

Bender, B., Maximum likelihood estimation of b values for magnitude grouped data, *Bull. Seism. Soc. Am.*, *73*, 831–851, 1983.

Bernard, P., A. Herrero, & C. Berge, Modeling Directivity of Heterogeneous Earthquake Ruptures, *Bull. Seism. Soc. Am.*, *86*, 1149–1160, 1996.

Beroza, G., Near-source modeling of the Loma Prieta earthquake: evidence for heterogeneous slip and implications for earthquake hazard, *Bull. Seism. Soc. Am.*, *81*, 1603–1621, 1990.

Beroza, G., & M. Zoback, Mechanism Diversity of the Loma Prieta Aftershocks and the Mechanics of Mainshock-Aftershock Interaction, *Science*, *259*, 210–213, 1993.

Bhattacharya, P. M., R. K. Majumdar, & J. A. Kayal, Fractal dimension and b-value mapping in northeast India, *Science*, *82*, 1486–1491, 2002.

Bouchon, M., H. Sekiguchi, K. Irikura, & T. Iwata, Some characteristics of the stress field of the 1995 Hyogo-ken Nanbu (Kobe) earthquake, *J. Geophys. Res.*, *103, B10*, 24,271–24,282, 1998.

Brune, J. N., Seismic moment seismicity and rate of slip along major fault zones, *J. Geophys. Res.*, *73*, 777–784, 1968.

Bürgmann, R., D. Schmidt, R. M. Nadeau, M. d’Alessio, E. Fielding, D. Manaker, T. V. McEvilly, & M. H. Murray, Earthquake potential along the Northern Hayward Fault, California, *Science*, *289*, 1178–1182, 2000.

Burridge, R., & L. Knopoff, Body force equivalents for seismic dislocations, *Bull. Seism. Soc. Am.*, *54*, 1875–1888, 1964.

Burridge, R., & L. Knopoff, Model and theoretical seismicity, *Bull. Seism. Soc. Am.*, *57*, 341–371, 1967.

Carlo, D. L., T. Lay, C. J. Ammon, & J. Zhang, Rupture process of the 1995 Antofagasta subduction earthquake (M_w=8.1), *Pure appl. geophys.*, *154*, 677–709, 1999.

Chen, Y., & C. G. Sammis, Asperity models for earthquakes, *Bull. Seism. Soc. Am.*, *93*, 1792–1802, 2003.

Chlieh, M., J. de Chabalier, J. Ruegg, R. Armijo, R. Dmowska, J. Campos, & K. Feigl, Crustal deformation and fault slip during the seismic cycle in the North Chile subduction zone, from GPS and InSAR observations, *Geophys. J. Int.*, *158*, 695–711, 2004.

Choy, G., & J. Boatwright, Global patterns of radiated seismic energy and apparent stress, *J. Geophys. Res.*, *100, No. B9*, 18,205–18,228, 1995.

Christensen, K., L. Danon, T. Scanlon, & P. Bak, Unified scaling law for earthquakes, in *Proceeding of the National Academy of Science of the USA (PNAS)*, pp. 2509–2513, 2002, published as Proceeding of the National Academy of Science of the USA (PNAS), volume 99, number 1.

Cloos, M., Thrust-type subduction-zone earthquakes and seamount asperities: A physical model for seismic rupture, *Geology*, *20*, 601–604, 1992.

Cloos, M., & R. L. Shreve, Shear-zone thickness and the seismicity of Chilean- and Marianas-type subduction zones, *Geology*, *24*, 107–110, 1996.

Coira, B., J. Davidson, C. Mpodozis, & V. Ramos, Tectonic and magmatic evolution of the Andes of northern Argentina and Chile, *Earth Sci. Rev.*, *18*, 303–332, 1982.

Comte, D., & G. Suárez, Spatio-temporal variations of seismicity in the Southern Peru and Northern Chile seismic gaps, *Pageoph*, *140*, 318–330, 1993.

Comte, D., M. Pardo, L. Dorbath, C. Dorbath, H. Haessler, L. Rivera, A. Cisternas, & L. Ponce, Determination of seismogenic interplate contact zone and crustal seismicity around Antofagasta, northern Chile using local data, *Geophys. J. Int.*, *116*, 553–561, 1994.

Das, S., & K. Aki, A numerical study of two-dimensional spontaneous rupture propagation, *Geophys. J. R. astr. Soc.*, *50*, 643–668, 1977.

Das, S., & B. V. Kostrov, An investigation of the complexity of the earthquake source time function using dynamic faulting models, *J. Geophys. Res.*, *93*, 8035–8050, 1988.

Davidsen, J., & C. Goltz, Are seismic waiting time distributions universal?, *Geophys. Res. Letters*, *XXX*, in press.

Delouis, B., *Subduction et Deformation Continentale au Nord-Chili*, L'Université Louis Pasteur de Strasbourg, Ecole et Observatoire de Physique du Globe, Laboratoire de Sismologie et de Physique de la terre, These de Doctoral, Strasbourg, 262 pp., 1996.

Delouis, B., H. Philip, L. Dorbath, & A. Cisternas, Recent crustal deformation in the Antofagasta region (northern Chile) and the subduction process, *Geophys. J. Int.*, *132*, 302–338, 1998.

Delouis, B., et al., The Mw = 8.0 Antofagasta (northern Chile) earthquake of 30 July 1995: A precursor to the end of the large 1877 gap, *Bull. Seism. Soc. Am.*, *87*, 427–445, 1997.

Dieterich, J., V. Cayol, & P.Okubo, The use of earthquake rate changes as a stress meter at Kilauea volcano, *Nature*, *408*, 457–460, 2000.

Dmowska, R., & L. C. Lovison, Influence of asperities along subduction interfaces on the stressing and seismicity of adjacent areas, *Tectonophys.*, *211*, 23–44, 1992.

Dmowska, R., G. Zheng, & J. R. Rice, Seismicity and deformation at convergent margins due to heterogeneous coupling, *J. Geophys. Res.*, *101*, 3015–3029, 1996.

Dziewoński, A., & J. H. Woodhouse, An experiment in systematic study of global seismicity: centroid-moment tensor solutions for 201 moderate and large earthquakes of 1981, *J. Geophys. Res.*, *88*, 3247–3271, 1983.

Dziewonski, A. M., G. Ekström, & M. P. Salganik, Centroid-moment tensor solutions for July-September 1995, *Phys. Earth Plan. Int.*, *97*, 3–13, 1996.

Eberhart-Phillips, D., & A. J. Michael, Three-dimensional velocity structure, seismicity and fault structure in the Parkfield region, Central California, *J. Geophys. Res.*, *98*, 15,737–15,758, 1993.

Frankel, A., High-Frequency Spectral Falloff of Earthquakes, Fractal Dimension of Complex Rupture, b Value, and Scaling of Strength on Faults, *J. Geophys. Res.*, *96*, 6291–6302, 1991.

Frohlich, C., Earthquakes with non-double-couple mechanisms, *Science*, *264*, 804–809, 1994.

Frohlich, C., & K. D. Apperson, Earthquake focal mechanisms, moment tensors, and the consistency of seismic activity near plate boundaries, *Tectonics*, *11*, 279–296, 1992.

Frohlich, C., M. A. Riedesel, & K. D. Apperson, Note concerning possible mechanisms for non-double-couple earthquake sources, *Geophys. Res. Lett.*, *16*, 523–526, 1989.

Giardini, D., Systematic analysis of deep seismicity: 200 centroid-moment tensor solutions for earthquakes between 1977 and 1980, *Geophys. J. Res. astr. Soc.*, *77*, 883–914, 1984.

Götze, H.-J., & A. Kirchner, Interpretation of gravity and geoid in the Central Andes between 20° and 29°S, *J. S. Am. Earth Sci.*, *10*, 179–188, 1997.

Götze, H.-J., & S. Krause, The Central Andean gravity high, a relic of an old subduction complex?, *Journal of South American Earth Sciences*, *14*, 799–811, 2002.

Götze, H.-J., & the MIGRA group, Group updates gravity database for Central Andes, *EOS Trans. Am. Geophys. Union*, *104*, 5 pages, 1996, http://www.agu.org/eos-elec/95189e.html.

Götze, H.-J., B. Lahmeyer, S. Schmidt, & S. Strunk, The lithospheric structure of the Central Andes (20°- 26°S) as inferred from interpretation of regional gravity, in *Tectonics of the Southern Central Andes, Structure and Evolution of an Active Continental Margin*, edited by K.-J. Reutter, E. Scheuber, & P. J. Wigger, pp. 7–22, Springer-Verlag, 1994.

Gregory, A. R., Aspects of rock physics from laboratory and log data that are important to seismic interpretation, in *Seismic Stratigraphy - applications to hydrocarbon exploration*, edited by C. E. Payton, Memoir 26, pp. 15–46, The American Association of Petroleum Geologists, Tulsa, Oklahoma, U. S. A., 1977.

Grosser, H., A. Rietbrock, M. Baumbach, G. R. Torres, & J. Rojas, Seismic tomography in the aftershock region of the Cariaco earthquake 1997, *abstract, EOS Trans. AGU*, 2001.

Guo, Z., & Y. Ogata, Correlation between characteristic parameters of aftershock distributions in time, space and magnitude, *Geophys. Res. Letters*, *22*, 993–996, 1995.

Gutenberg, B., & C. Richter, Magnitude and energy of earthquakes, *Annali di Geofisica*, *9*, 1–15, 1956.

Gutenberg, B., & C. F. Richter, Frequency of earthquakes in California, *Bull. Seism. Soc. Am.*, *34*, 185–188, 1944.

Haberland, C., & A. Rietbrock, Attenuation tomography in the western central Andes: A detailed insight into the structure of a magmatic arc, *J. Geophys. Res.*, *106*, 11,151–11,167, 2001.

Hainzl, S., Erdbeben und selbstorganisierte Kritizität, Dissertation, Universität Potsdam, Institut für Physik, Lehrstuhl für nichtlineare Dynamik, 1998.

Hainzl, S., G. Zoeller, & J. Kurths, Similar power laws for foreshock and aftershock sequences in a spring-block model for earthquakes, *J. Geophys. Res.*, *104*, 7243–7254, 1999.

Hainzl, S., G. Zoeller, J. Kurths, & J. Zschau, Seismic quiescence as an indicator for large earthquakes in a system of self-organized criticality, *Geophys. Res. Letters*, *27*, 597–600, 2000.

Hanks, T. C., b values and $\omega^{-\nu}$ seismic source models: Implications for tectonic stress variations along active crustal fault zones and the estimation of high-frequency strong ground motion, *J. Geophys. Res.*, *84*, 2235–2242, 1979.

Henry, C., & S. Das, Aftershock zones of large shallow earthquakes: fault dimensions, aftershock area expansion and scaling relations, *Geophys. J. Int.*, *147*, 272–293, 2001.

Herrero, A., & P. Bernard, A Kinematic Self-Similar Rupture Process for Earthquakes, *Bull. Seism. Soc. Am.*, *84*, 1216–1228, 1994.

Hinz, K., & . others, CINCA, Crustal investigations off- and onshore Nazca/Central Andes, Final Report, *Bundesanstalt für Geowissenschaften und Rohstoffe, Hannover*, *Archiv-Nr. BGR 117.613*, 217 pp., 1998.

Hinz, K., J. Adam, H. O. Bargeloh, M. Block, & V. D. . . others, Crustal investigations off- and onshore Nazca/Central Andes, CINCA Sonne Cruise 104, Leg 1, *Bundesanstalt für Geowissenschaften und Rohstoffe, Hannover*, *Archiv-Nr. BGR 114.767*, 113 pp., 1995.

Holt, W. E., J. F. Ni, T. C. Wallace, & A. J. Haines, The active tectonics of the Eastern Himalayan syntaxis and surrounding regions, *J. Geophys. Res.*, *96*, 14,595–14,632, 1991.

Horálek, J., J. Šilený, & T. Fischer, Moment tensors of the January 1997 earthquake swarm in NW Bohemia (Czech Republic): Double-couple vs. non-double-couple events, *Tectonophysics*, *356*, 65–85, 2002.

Husen, S., *Local earthquake tomography of a convergent margin, North Chile*, Christian-Albrechts-Universität Kiel, Mathematisch- Naturwissenschaftliche Fakultät, Dissertation, Kiel, 129 pp., 1999.

Husen, S., & E. Kissling, Postseismic fluid flow after the large subduction earthquake of Antofagasta, Chile, *Geology*, *29*, 847–850, 2001.

Ide, S., Estimation of Radiated Energy of Finite-Source Earthquake Models, *Bull. Seism. Soc. Am.*, *92, No. 8*, 2994–3005, 2002.

Ihmlé, P. F., & R. Madariaga, Monochromatic body waves excited by great subduction zone earthquakes, *Geophys. Res. Lett.*, *23*, 2999–3002, 1996.

Ihmlé, P. F., & J.-C. Ruegg, Source tomography by simulated annealing using broad-band surface waves and geodetic data: application to the M_w=8.1 Chile, *Geophys. J. Int.*, *131*, 146–158, 1997.

Ishimoto, M., & K. Iida, Observations of earthquakes registered with the microseismograph constructed recently, *Bull. Earthquake Res. Inst.*, *17*, 443–478, 1939.

Ito, K., & M. Matsuzaki, Earthquakes as a self-organized critical phenomena, *J. Geophys. Res.*, *95*, 6,853, 1990.

Jackson, J., & D. McKenzie, The relationship between plate motions and seismic moment tensors and the rate of active deformation in the Mediterranean and Middle East, *Geophys. J.*, *93*, 45–73, 1988.

Jarrard, R. D., Relations among subduction parameters, *Rev. Geophys. Space Phys.*, *24*, 217–284, 1986.

Jin, A., & K. Aki, Spatial and Temporal Correlation Between Coda Q-1 and Seismicity and Its Physical Mechanism, *J. Geophys. Res.*, *94*, 14,041–14,059, 1989.

Johnson, L. R., & R. M. Nadeau, Asperity model of an earthquake: Static problem, *Bull. Seism. Soc. Am*, *92*, 672–686, 2002.

Jost, M. L., & R. B. Herrmann, A student's guide to and review of moment tensors, *Seism. Res. Lett.*, *60*, 37–57, 1989.

Julian, B. R., A. D. Miller, & G. R. Foulger, Non-double-couple earthquake mechanisms at the Hengill-Grensdalur volcanic complex, southwest Iceland, *Geophys. Res. Lett.*, *24*, 743–746, 1997.

Kagan, Y. Y., & L. Knopoff, The first-order statistical moment of the seismic moment tensor, *Geophys. J. R. astr. Soc.*, *81*, 429–444, 1985.

Kanamori, H., *Seismic and aseismic slip along subduction zones and their tectonic implications*, Maurice Ewing Series, ed. M. Talwani and W. C. PitmanL̀eerzeichen‘III: in ”Island Arcs, Deep Sea Trenches and Back Arc Basins”, AGU, V. 1, p. 163-174, 1977.

Kanamori, H., & D. L. Anderson, Theoretical basis of some empirical relations in seismology, *Bull. Seism. Soc. Am.*, *65*, 1073–1096, 1975.

Kanamori, H., & G. S. Stewart, Seismological aspects of the Guatemala earthquake of February 4, 1976, *J. Geophys. Res.*, *83, B7*, 3427–3434, 1978.

Kausel, E., Los Terremotos de Agosto de 1868 y Mayo de 1877 que Afectaron el Sur del Peru y Norte de Chile, *Bol. Acad. Chil. Cienc.*, *3*, 8–12, 1986.

Kausel, E., & J. Campos, The $\mathrm{M_s}$=8 tensional earthquake of 9 December 1950 of Northern Chile and its relation to the seismic potential of the region, *Phys. Earth Planet. Inter.*, *72*, 220–235, 1992.

Keilis-Borok, V. I., On the estimation of the displacement in an earthquake source and of source dimensions, *Ann. Geophys.*, *12*, 205–214, 1959.

Kelleher, J. A., Rupture zones of large South American earthquakes and some predictions, *J. Geophys. Res.*, *77*, 2087–2103, 1972.

Kinoshita, S., H. Fujiwara, T. Mikoshiba, & T. Hoshino, Secondary Love waves observed by a strong motion array in the Tokyo lowland, Japan, *J. Phys. Earth*, *40*, 99–116, 1992.

Kissling, E., S. Solarino, & M. Cattaneo, Improved seismic velocity reference model from local earthquake data in northwestern Italy, *Terra Nova*, *7*, 528–534, 1995.

Kisslinger, C., & A. Hasegawa, Seismotectonics of intermediate-depth earthquakes from properties of aftershock sequences, *Tectonophysics*, *197*, 27–40, 1991.

Kisslinger, C., & L. Jones, Properties of Aftershock Sequences in Southern California, *J. Geophys. Res.*, *96*, 11,947–11,958, 1991.

Klotz, J., et al., GPS-derived deformation of the Central Andes including the 1995 Antofagasta M_w=8.0 earthquake, *Pure appl. geophys.*, *154*, 709–730, 1999.

Knopoff, L., Energy release in earthquakes, *Geophys. J. R. astr. Soc.*, *1*, 44–52, 1958.

Knopoff, L., & M. J. Randall, The compensated linear vector dipole: a possible mechanism for earthquakes, *J. Geophys. Res.*, *75*, 4957–4963, 1970.

Kösters, M., H.-J. Götze, S. Schmidt, J. Fritsch, & M. Araneda, Gravity Field of a Continent-Ocean Transition Mapped From Land Air and Sea, *EOS*, *78*, 13–16, 1997.

Kostrov, B., Seismic moment and energy of earthquakes and seismic flow of rock, *Phys. Solid. Earth*, *1*, 23–40, 1974.

Kubas, A., & S. A. Sipkin, Non-double-couple earthquake mechanisms in the Nazca Plate subduction zone, *Geophysical Research Letters*, *14*, 339–342, 1987.

Kubo, A., E. Fukuyama, H. Kawai, & K. Nonomura, NIED seismic moment tensor catalogue for regional earthquakes around Japan: quality test and application, *Tectonophysics*, *356*, 23–48, 2002.

Kuge, K., & H. Kawakatsu, Significance of non-double couple components of deep and intermediate-depth earthquakes: Implications from moment tensor inversions of long-period seismic waves, *Phys. Earth Plan. Int.*, *75*, 243–266, 1993.

Lallemand, S., & X. Le Pichon, Coulomb wedge model applied to the subduction of seamounts in the Japan trench, *Geology*, *15*, 1065–1069, 1987.

Lay, T., & H. Kanamori, An asperity model of large earthquake sequences, in *Earthquake Predition*, edited by D. W. Simpson & P. G. Richards, vol. 4 of *Maurice Ewing Series*, pp. 579–592, AGU, 1981.

Lay, T., & T. C. Wallace, *Modern Global Seismology*, Academic Press, San Diego, XII vol., 521 pp., 1995.

Lay, T., H. Kanamori, & L. Ruff, The asperity model and the nature of large subduction zone earthquakes, *Earthquake Pred. Res.*, *1*, 3–71, 1982.

Lee, W. H. K., & J. C. Lahr, HYPO71 - A computer program for determining hypocenter, magnitude and first motion pattern of local earthquakes, *open file report, U.S. Geol. Survey*, *75/311*, 1975.

Madariaga, R., On the relation between seismic moment and stress drop in the presence of stress and strength heterogeneity, *J. Geophys. Res.*, *84*, 2243–2250, 1979.

Madariaga, R., Earthquake source theory: a review, in *Earthquakes: Observation, Theory and Interpretation*, edited by H. Kanamori & E. Boschi, Proc. Int. School of Phys., Enrico Fermi course LXXXV, pp. 1–44, North-Holland, Amsterdam, 1983.

Mai, M., Database of finite-source rupture models, *www.seismo.ethz.ch/srcmod/*, *webpage*, 2002.

Main, I., Statistical physics, seismogenesis, and seismic hazard, *Rev. Geophys.*, *34*, 433, 1996.

Main, I. G., Earthquakes as critical phenomena: Implications for probabilistic seismic hazard analysis, *Bull. Seism. Soc. Am.*, *85*, 1299–1308, 1995.

Main, I. G., P. G. Meredith, & C. Jones, A reinterpretation of the precursory seismic b-value anomaly from fracture mechanics, *Geophys. J.*, *96*, 131–138, 1989.

Martinod, J., D. Comte, C. David, B. Glass, E. Correa, M. Vallée, L. Audin, G. Hérail, & M. Farias, Superficial crustal seismicity in northern chile and the seismic cycle on the nazca subduction zone, *abstract, EGS, Nice*, 2002.

Marzocchi, W., & L. Sandri, A review and new insights on the estimation of the b-value and its uncertainty, *Anals of Geophysics*, *46*, 1271–1282, 2003.

McCloskey, J., A hierarchical model for earthquake generation on coupled segments of a transform fault, *Geophys. J. Int.*, *115*, 538–551, 1983.

McGarr, A., & J. Fletcher, Mapping Apparent Stress and Energy Radiation over Fault Zones of Major Earthquakes, *Bull. Seism. Soc. Am.*, *92, No. 5*, 1633–1645, 2002.

Mendoza, C., & S. H. Hartzell, Aftershock patterns and main shock faulting, *Bull. Seism. Soc. Am*, *78*, 1438–1449, 1988.

Miller, A. D., G. R. Foulger, & B. R. Julian, Non-double-couple earthquakes, 2, Observations, *Rev. Geophys.*, *36*, 551–568, 1998.

Mogi, M., Magnitude-frequency relation for elastic shocks accompying fractures of various materials and some related problems in earthquakes, *Bull. Earthquake Res. Inst.*, *40*, 831–853, 1962, 2nd paper.

Mori, J., & R. E. Abercrombie, Depth dependence of earthquake frequency-magnitude distributions in California: Implications for rupture initiation, *J. Geophys. Res.*, *102*, 15,081–15,090, 1997.

Nabelek, J., Determination of earthquake source parameters from the inversion of body waves, Phd thesis, M.I.T., Cambridge, Massachusetts, 1984.

Nadeau, R. M., & L. R. Johnson, Seismological studies at Parkfield VI: Moment release rates and estimates of source parameters for small repeating earthquakes, *Bull. Seism. Soc. Am.*, *88*, 790–814, 1998.

Norabuena, E., L. Leffler-Griffin, A. Mao, T. Dixon, S. Stein, I. S. Sacks, L. Ocola, & M. Ellis, Space geodetic observations of Nazca-South America convergence across the Central Andes, *Science*, *279*, 358–362, 1998.

Norabuena, E. O., T. H. Dixon, S. Stein, & C. G. A. Harrison, Decelerating Nazca-South America and Nazca-Pacific plate motions, *Geophys. Res. Lett.*, *26*, 3405–3408, 1999.

Ortlieb, L., S. Barrientos, & N. Guzman, Coseismic coastal uplift and coralline algae record in Northern Chile: The 1995 Antofagasta earthquake case, *Quaternary Science Reviews*, *15*, 949–960, 1996.

Pacheco, J. F., C. H. Scholz, & L. R. Sykes, Changes in frequency-size relationship from small to large earthquakes, *Nature*, *355*, 71–73, 1992.

Papageorgiou, A. S., The barrier model and strong ground motion, *Pure appl. geophys.*, *160*, 603–634, 2003.

Papageorgiou, A. S., & K. Aki, A specific barrier model for the quantitative description of inhomogeneous faulting and the prediction of strong ground motion. Part II. Applications of the model, *Bull. Seism. Soc. Am.*, *73*, 953–978, 1983.

Pardo-Casas, F., & P. Molnar, Relative motion of the Nazca (Farallon) and South American plates since late Cretaceous time, *Tectonics*, *6*, 233–248, 1987.

Patzig, R., Lokalbeben-Tomographie der Umgebung von Antofagasta (Nordchile) sowie Betrachtungen der Magnituden-Häufigkeits-Parameter in dieser Region, *Berliner Geowis. Abh.*, p. 219, 2000.

Patzwahl, R., *Plattengeometrie und Krustenstruktur am Kontinentalrand Nord-Chiles aus weitwinkelseismischen Messungen*, Berliner geowiss. Abh., Vol. 30, Dissertation, Kiel, 150 pp., 1998.

Patzwahl, R., J. Mechie, A. Schulze, & P. Giese, Two-dimensional velocity models of the Nazca plate subduction zone between 19.5°S and 25°S from wide-angle seismic measurements during the CINCA95 project, *Journal of Geophysical Research*, *104*, 7293–7317, 1999.

Pichowiak, S., Early Jurassic to early Cretaceous magmatism in the Coastal Cordillera and the Central Depression of North Chile, in *Tectonics of the Southern Central Andes*, edited by K.-J. Reutter, E. Scheuber, & P. J. Wigger, pp. 203–217, Springer Verlag, 1994.

Porth, R., Die Seismizität der andinen Subduktionszone, insbesondere die räumliche Verteilung von b, Diplomarbeit, Freie Universität Berlin, Institut für Geologie, Geophysik und Geoinformatik, 1993.

Press, W. H., B. P. Flannery, S. A. Teukolsky, & W. T. Vetterling, *Numerical Recipes, The Art of Scientific Computing*, Univ. of Cambridge, The Pitt Building, Trumpington Street, Cambridge CB2 IRP, 1988.

Pritchard, M. E., M. Simons, P. A. Rosen, S. Hensley, & F. H. Webb, Co-seismic slip from the 1995 July 30 M_W=8.1 Antofagasta, Chile, earthquake as constrained by InSAR and GPS observations, *Geophys. J. Int.*, *150*, 362–376, 2002.

Randell, M. J., & L. Knopoff, The mechanism at the focus of deep earthquakes, *J. Geophys. Res.*, *75*, 4965–4976, 1970.

Reasenberg, P. A., & D. H. Oppenheimer, *FPFIT, FPPLOT and FPPAGE: Fortran computer programs for calculating and displaying earthquake fault-plane solutions*, U.S. Geol. Surv., open file report, 109 pp, 1985.

Richter, C., *Magnitude, statistics, energy*, Elementary Seismology, Freeman, San Francisco, Cal., p. 338-349, 1958.

Rietbrock, A., Entwicklung eines Programmsystems zur konsistenten Auswertung grosser seismologischer Datensätze mit Anwendung auf die Untersuchung der Absorptionsstruktur der Loma-Prieta-Region, Kalifornien, Dissertation, Ludwigs-Maximilians-Universität, München, Fakultät der Geowissenschaften, 1996.

Rietbrock, A., & F. Scherbaum, The GIANT analysis system, *Seis. Res. Lett.*, *69*, 40–45, 1998.

Rudnicki, J. W., & H. Kanamori, Effects of fault interaction on moment, stress drop, and strain energy release, *J. Geophys. Res.*, *86*, 1785–1793, 1981.

Ruegg, J. C., et al., The Mw = 8.1 Antofagasta (North Chile) earthquake of July 30, 1995: First results from teleseismic and geodetic data, *Geophys. Res. Lett.*, *23*, 917–920, 1996.

Ruff, L. J., Asperity distributions and large earthquake occurrence in subduction zones, *Tectonophys.*, *211*, 61–83, 1992.

Rundle, J., & W. Klein, Scaling and critical phenomena in a cellular automation slider-block model for earthquakes, *J. Stat. Phys.*, *72*, 405–413, 1993.

Rundle, J. B., D. L. Turcotte, R. Shcherbakov, W. Klein, & C. Sammis, Statistical physics approach to understanding the multiscale dynamics of earthquake fault systems, *Rev. Geophys.*, *41*, 2003, citation no. 1019, doi: 10.1029/2003RG000135.

Sammis, C. G., & J. R. Rice, Repeating earthquakes as low-stress-drop events at a border between locked and creeping fault patches, *Bull. Seism. Soc. Am.*, *91*, 532–537, 2001.

Sammis, C. G., R. M. Nadeau, & L. R. Johnson, How strong is an asperity?, *J. Geophys. Res.*, *104*, 10,609–10,619, 1999.

Scherbaum, F., What can we learn from aftershocks?, *Geologie en Mijnbouw*, *73*, 241–252, 1994.

Scherbaum, F., J. Johnson, & A. Rietbrock, *Programmable Interactive Toolbox for Seismological Analysis, PITSA*, 1999.

Scheuber, E., T. Bogdanic, A. Jensen, & K.-J. Reutter, Tectonic development of the North Chilean Andes in relation to plate convergence and magmatism since the Jurassic, *in: Tectonics of the Southern Central Andes, editors: K.-J. Reutter and E. Scheuber and P. J. Wigger, Springer Verlag, Berlin*, pp. 121–139, 1994.

Scheuber, E., K. Hammerschmidt, & H. Friedrichsen, ^{40}Ar/^{39}Ar and Rb-Sr analyses from ductile shear zones from the Atacama Fault Zone, northern Chile: the age of deformation, *Tectonophysics*, *250*, 61–87, 1995.

Scholz, C. H., The frequency-magnitude relation of microfracturing in rock and its relation to earthquakes, *Bull. Seism. Soc. Am.*, *58*, 399–415, 1968.

Scholz, C. H., *The Mechanics of Earthquakes and Faulting*, Cambridge Univ. Press, Cambridge, 1 vol., 439 pp., 1990.

Schön, J., *Petrophysik: Physikalische Eigenschaften von Gesteinen und Mineralen*, Enke, Stuttgart, 403 pp., 1983.

Schurr, B., G. Asch, A. Rietbrock, R. Trumbull, & C. Haberland, Complex patterns of fluid and melt transport in the central Andean subduction zone revealed by attenuation tomography, *Earth planet. Sci. Lett.*, *215*, 105–119, 2003.

Shapiro, S. A., R. Patzig, E. Rothert, & J. Rindschwentner, Triggering of seismicity by pore-pressure perturbations: Permeability-related signatures of the phenomenon, *Pure appl. geophys.*, *160*, 1051–1066, 2003.

Shcherbakov, R., & D. Turcotte, A Damage Mechanics Model for Aftershocks, *Pure appl. geophys.*, *XXX*, in press.

Shi, J., & B. A. Bolt, The standard error of the magnitude-frequency b value, *Bull. Seism. Soc. Am.*, *72*, 1677–1687, 1982.

Shimazaki, K., Small and large earthquakes: The effects of the thickness of the seismogenic layer and free surface, in *Earthquake Source Mechanics, Maurice Ewing Ser.*, edited by S. Das, J. Boatwright, & C. Scholz, vol. 6, pp. 209–216, AGU, Washington D.C., 1986.

Smith, W., Evidence for precursory changes in the frequency-magnitude b-value, *Geophys. J. R. astr. Soc.*, *86*, 815–838, 1986.

Sobiesiak, M., Fault plane structure of the Antofagasta, Chile, earthquake of 1995, *Geophys. Res. Letters*, *27*, 581–584, 2000.

Starr, A. T., Slip in a crystal and rupture in a solid due to shear, *Proc. Cambr. Phil. Soc*, *24*, 489–500, 1928.

Stepp, J. C., Analysis of completeness of earthquake sample in the Puget Sound Area and its effect on statistical estimates of earthquake hazard, in *Contributions to Seismic Zoning*, edited by S. Handing, vol. ERL-267-ESL 30, pp. 897–908, U.S. Dep. of Commerce, NOAA tech. report, 1973.

Sue, C., J. R. Grasso, F. Lahaie, & D. Amitrano, Mechanical behavior of western alpine structures inferred from statistical analysis of seismicity, *Geophys. Res. Lett.*, *29*, 65–1 to 65–4, 2002, citation no. 1224, doi:10.1029/2001GL014050.

Taylor, G. K., J. Grocott, A. Pope, & D. E. Randall, Mesozoic fault systems, deformation and fault block rotation in the Andean forearc: a crustal scale strike-slip duplex in the Coastal Cordillera of northern Chile, *Tectonophysics*, *299*, 93–109, 1998.

Tichelaar, B. W., & L. J. Ruff, Seismic coupling along the Chilean Subduction Zone, *J. Geophys. Res.*, *96*, 11,997–12,022, 1991.

Trifunac, M., & J. Brune, Complexity of energy release during the Imperial Valley, California, earthquake of 1940, *Bull. Seism. Soc. Am.*, *60*, 137–160, 1970.

Turcotte, D., *Fractals and Chaos in Geology and Geophysics*, Cambridge University Press, 1997.

Turcotte, D. L., *Fractals and Chaos in Geology and Geophysics*, Cambridge University Press, Cambridge, 1 vol., 221 pp., 1992.

Urbancic, T. I., C.-I. Trifu, J. M. Long, & R. P. Young, Space-time correlations of b Values with stress release, *PAGEOPH*, *139*, 449–462, 1992.

Utsu, T., Statistical study on the occurrence of aftershocks, *Geophys. Mag.*, *30*, 521–605, 1961.

Utsu, T., A method for determining the value of b in formula $logN = a - bM$ showing the magnitude-frequency relation for earthquakes, *Geophys. Bull. Hokkaido Univ.*, *13*, 99–103, 1965.

Utsu, T., On seismicity, in: Report of the Joint Research Institute for Statistical Mathematics, *Inst. for Statistical Mathematics, Tokyo*, pp. 139–157, 1992.

Uyeda, S., & H. Kanamori, Back-arc opening and the mode of subduction, *J. Geophys. Res.*, *84*, 1049–1061, 1979.

Vavryčuk, V., Inversion for parameters of tensile earthquakes, *J. Geophys. Res.*, *106*, 16,339–16,356, 2001, doi: 10.1029/2001JB000372.

von Huene, R., & C. R. Ranero, Subduction erosion and basal friction along the sediment-starved convergent margin off Antofagasta, Chile, *J. Geophys. Res.*, *108*, 3–1 to 3–16, 2003, doi: 10.1029/2001JB001596.

von Huene, R., W. Weinrebe, & F. Heeren, Subduction erosion along the North Chile margin, *Journal of Geodynamics*, *27*, 345–358, 1999.

von Seggern, D., A random stress model for seismicity statistics and earthquake prediction, *Geophys. Res. Lett.*, *7*, 637–640, 1980.

Waldhauser, F., & W. Ellsworth, Fault structure and mechanics of the Hayward Fault, California, from double-difference earthquake locations, *J. Geophys. Res.*, *107*, ESE3–1–3–15, 2002.

Wells, R. E., R. Blakely, & Y. Sugiyama, Great slip in great subduction earthquakes occurs under forearc basins, *abstract, GSA Annual Meeting, Corvallis*, 2002.

Wiemer, S., & J. Benoit, Mapping the b value anomaly at 100 km depth in the Alaska and New Zealand subduction zones, *Geophys. Res. Lett.*, *23*, 1557–1560, 1996.

Wiemer, S., & K. Katsumata, Spatial variability of seismicity parameters in aftershock zones, *Journal of Geophysical Research*, *104*, 13,135–13,151, 1999.

Wiemer, S., & S. R. McNutt, Variations in the frequency-magnitude distribution with depth in two volcanic areas: Mount St. Helens, Washington, and Mt. Spurr, Alaska, *Geophys. Res. Lett.*, *24*, 189–192, 1997.

Wiemer, S., & M. Wyss, Seismic quiescence before the Landers ($m = 7.5$) and big Bear ($m = 6.5$) 1992 earthquakes, *Bull. Seism. Soc. Am.*, *84*, 900–916, 1994.

Wiemer, S., & M. Wyss, Mapping the frequency-magnitude distribution in asperities: An improved technique to calculate recurrence times?, *J. Geophys. Res.*, *102*, 15,115–15,128, 1997.

Wiemer, S., & M. Wyss, Minimum magnitude of completeness in earthquake catalogs: Examples from Alaska, the western United States, and Japan, *Bull. Seism. Soc. Am.*, *90*, 859–869, 2000.

Wigger, P. J., et al., Variation in the crustal structure of the southern Central Andes deduced from seismic refraction investigations, in *Tectonics of the Southern Central Andes*, edited by K.-J. Reutter, E. Scheuber, & P. J. Wigger, pp. 23–48, Springer Verlag, 1994.

Wyss, M., Towards a physical understanding of the earthquake frequency distribution, *Geophys. J. R. astr. Soc.*, *31*, 341–359, 1973.

Wyss, M., & J. Brune, The Alaska earthquake of 28 March 1964: A complex multiple rupture, *Bull. Seism. Soc. Am.*, *57*, 1017–1023, 1967.

Wyss, M., & J. Brune, Seismic moment, stress, and source dimensions for earthquakes in the California-Nevada region, *J. Geophys. Res.*, *73*, 4681–4694, 1968.

Wyss, M., & R. Habermann, Precursory seismic quiescence, *Pure Appl. Geophys.*, *126*, 319–332, 1988.

Wyss, M., K. Shimazaki, & S. Wiemer, Mapping active magma chambers by b values beneath the off-Ito volcano, Japan, *J. Geophys. Res.*, *102*, 20,413–20,422, 1997.

Xia, Y., G. W. Michel, C. Reigber, J. Klotz, & H. Kaufmann, Seismic unloading and loading in Northern Central Chile as observed by D-INSAR and GPS, *International Journal of Remote Sensing*, *24*, 4375–4391, 2003.

Zoback, M. L., First- and second-order patterns of stress in the lithosphere: The World Stress Map Project, *J. Geophys. Res.*, *97*, 11,703–11,728, 1992.

Zonenshayn, L. P., L. A. Savostin, & A. P. Sedov, Global paleogeodynamic reconstructions for the last 160 million years, *Geotectonics*, *18*, 181–195, 1984.

Acknowledgements

I would like to express my sincerest thanks to my principal advisor Prof. Dr. Jochen Zschau and my second advisor Prof. Dr. Frank Scherbaum for scientific advices, discussions and in particular for their patience during the rather long time finishing this thesis. They both accepted the interruption of my thesis in favour of a three years stay in Venezuela and continued their support after my return to Germany. I am grateful to Prof. Zschau for always providing me with a possibility to work for some days at the department when I was on vacations in Germany. This helped a lot to maintain contacts with my colleagues.

I want to thank Dr. Pascal Bernard and Dr. Stefan Wiemer for taking up the role as external reviewers. The intensive discussions I had with Pascal helped a lot to improve the manuscript of my thesis. To Stefan I am especially grateful for answering all my questions when I started to work with his program ZMAP. I really appreciated his fast replies whenever a problem occurred, also during my stay in Venezuela.

I am very much indebted to all my colleagues who were busy in the field recording the data after the Antofagasta earthquake and were occupied for a long time with preprocessing the vast amount of data of this aftershock sequence. My special thanks go to Dr. Michael Baumbach who also introduced me to the work of the Task Force. Dr. Stephan Husen and Dr. Robert Patzig I want to thank for sharing with me the time consuming job of determining the hypocenters manually. The high precision of the dataset was achieved to a good part through their diligent work.

Thanks and big hugs are also going to all my colleagues and friends of Section 2.1 in Department 2 of the GFZ. Here I found support not only in scientific matters but in all matters of life. Especially I would like to mention Dr. Helmut Grosser who never refused any help or debate about fault plane solutions and moment tensors or any other concerns.

For their never ending patience in technical support and helpful comments I am indebted to all collegues of Section 2.2, especially to Dr. Trond Ryberg, Ariane Siebert and Christof Lendl.

I would like to thank Prof. Dr. Onno Oncken for his support and interest in my thesis. The fruitful discussions I had with his working group and members of the SFB 267 here at the GFZ or in the Geophysical Institute of the Free University of Berlin contributed a lot to the interpretation of results in my thesis. Here I am especially indebted to Dr. Uwe Meyer and Dr. Jürgen Klotz.

Financial support was coming from GFZ Potsdam and the SFB 267. The multidisciplinary structure of the GFZ provided an excellent tool for exchanging ideas and it was a great pleasure to be able to discuss with so many scientist from different fields.

Sometimes I really would be at a loss without my family: Thea, Rony, Doris, Maria, Jan and Marie-Theres. Without their continous incouragement covering all ”needs in life” it would have been hard to finish this thesis. I am happy that they look after me even at the remotest places in the world... And without friends no one could cope with the larger and smaller every-day troubles, especially during such a time when finishing a thesis; many thanks to all my friends in Potsdam and Berlin.

Last but not least I want to thank my Venezuelian friends and colleagues for teaching me how to live and to work in a different culture and for their understanding when I wanted to leave to finish my thesis at a time when seismologists were urgently needed at FUNVISIS.